

Design and construction of a turbine model for testing in MarinLab

Bendik Weltzien
Hans Joakim Jakobsen
Nikolai Arntzen

Bachelor's thesis in Marine Technology
Bergen, Norway 2022



Western Norway
University of
Applied Sciences

Design and construction of a turbine model for testing in MarinLab

Bendik Weltzien
Hans Joakim Jakobsen
Nikolai Armtzen

Department of Mechanical- and Marine Engineering
Western Norway University of Applied Sciences
NO-5063 Bergen, Norge

IMM 2022-M30

Høgskulen på Vestlandet
Institutt for Maskin- og Marinfag
Inndalsveien 28,
NO-5063 Bergen, Norge

Cover and backside images © Norbert Lümme

Norsk tittel: Design og konstruksjon av en turbinmodell for testing i Marin-Lab

Author(s), student number: Bendik Weltzien 578099
Hans Joakim Jakobsen 585066
Nikolai Arntzen 585052

Study program: Marine Technology
Date: May 2022
Report number: IMM 2022-M 30
Supervisor at HVL: Jan Michael Simon Bartl
Assigned by: HVL
Contact person: Jan Michael Simon Bartl

Antall filer levert digitalt: 1

Preface

This bachelor's thesis is written at the Department of Mechanical and Marine Engineering for the Western University of Applied Sciences (HVL) as part of the bachelor's program in Marine Technology. The thesis is internally supervised by Associate Professor Jan Bartl.

In association with this thesis, we would like to express our thanks to Associate Professor David Roger Lande-Sudall for his work on design and manufacturing of the previous model upon which this project is built. Thanks to the lab engineers at HVL, Harald Moen, Robert Larsson, and Kjetil Gravelseter for advising on the design and making sure the lab is in working order. A special thanks to Jan Bartl for being available at all times to advise and help on the project.

Abstract

Reducing dependencies on fossil fuels and further research on renewable energy sources is a crucial step to achieve climate neutrality. The use of scaled model testing can provide important data for further innovation in this sector. In this thesis, the design, construction, and testing of a model scale turbine will be conducted. The aim is to design an efficient and fully functional model turbine for future research in MarinLab at Høgskulen på Vestlandet (HVL). The model builds upon a previously designed turbine at HVL.

The model contains various electrical components and measurement instruments, which adds to the importance of a durable and watertight design. Rapid prototyping with 3D-printing is used to quickly discover potential manufacturing problems, and in addition, as an aid in the final resistance tests. Furthermore, a complete assembly manual of the turbine is made to ease the learning curve for future users and to ensure proper maintenance in the coming years.

A series of hydrodynamic resistance tests are conducted on the nacelle in MarinLab. Drag forces affecting the model are measured and compared to the previously designed turbine. Three different 3D-printed nacelle designs are used in the tests, both streamlined and non-streamlined. Ultimately this analysis highlights the importance of the nacelle design of a turbine concerning low hydrodynamic resistance and avoiding unwanted resonance.

Sammendrag

Å redusere avhengigheten av fossilt brensel, og videre forskning på fornybare energikilder er et viktig steg for å oppnå klimanøytralitet. Bruk av modelltesting kan gi viktige data for videre innovasjon i denne sektoren. I denne oppgaven vil design, konstruksjon og testing av en turbin i modellskala bli utført. Målet er å designe en effektiv og fullt funksjonell modellturbin for fremtidig forskning i MarinLab ved Høgskulen på Vestlandet (HVL). Modellen bygger på en tidligere designet turbin ved HVL.

Modellen inneholder ulike elektriske komponenter og måleinstrumenter, som øker betydningen av et slitesterkt og vanntett design. Prototyping med 3D-printing brukes for å raskt oppdage potensielle produksjonsproblemer, og i tillegg som et hjelpemiddel i de endelige motstandstestene. Videre er det laget en komplett monteringsmanual for turbinen for å lette læringskurven for fremtidige brukere, og for å sikre riktig vedlikehold i årene som kommer.

En serie hydrodynamiske motstandstester er utført på nacellen i MarinLab. Dragkrefter som påvirker modellen måles, og sammenlignes med den tidligere konstruerte turbinen. Tre forskjellige 3D-printede nacelledesign er brukt i testene, både strømlinjeformet og ikke-strømlinjeformet. Denne analysen fremhever viktigheten av nacelledesignet til en turbin med hensyn til lav motstand, og for å unngå uønsket resonans.

Contents

| | |
|--|------------|
| Abstract | iii |
| Sammendrag | v |
| 1 Introduction | 1 |
| 2 Theory | 2 |
| 2.1 Model scaling | 2 |
| 2.2 Momentum theory | 2 |
| 2.3 Drag | 4 |
| 2.4 Vortex-induced vibrations | 6 |
| 3 Design and construction | 7 |
| 3.1 Design process | 7 |
| 3.2 Design and components | 8 |
| 3.2.1 Instrumentation | 10 |
| 3.2.2 Powertrain | 10 |
| 3.3 Material selection | 12 |
| 3.4 Waterproofing | 13 |
| 3.5 Rapid Prototyping | 15 |
| 3.5.1 Challenges | 15 |
| 3.6 Tolerances and fits | 16 |
| 3.7 Assembly manual | 17 |
| 4 Experimental method | 18 |
| 4.1 Calibration of load cells | 18 |
| 4.2 Carriage setup | 19 |
| 4.3 Tower and nacelle setup | 20 |
| 4.4 Sources of error | 21 |
| 4.4.1 Systematic error | 21 |
| 4.4.2 Random error | 21 |
| 4.5 Data processing | 21 |
| 5 Results | 22 |
| 5.1 Drag force comparison | 22 |
| 5.2 Drag coefficients | 23 |
| 5.3 Choice of nacelle | 24 |
| 5.4 Power spectral analysis | 24 |
| 6 Discussion | 25 |
| 6.1 Results validation | 25 |
| 6.2 Effects of VIV on measurements | 26 |
| 7 Conclusion | 28 |
| References | 29 |
| Appendix | 31 |
| Appendix A: Data recordings | 32 |
| Appendix B: CAD drawings | 35 |
| Appendix C: Matlab script | 46 |
| Appendix D: Assembly manual | 58 |

1 Introduction

The recent geopolitical situation and the resulting changes in the energy market has further emphasized the importance of renewable sources of energy. Europe still imports 58% of its energy – mostly fossil fuels and often from countries posing serious geopolitical risks [1]. Reducing the dependency on fossil fuels and further development of renewable energy sources – is an important step to achieving climate neutrality.

Important sources of renewable energy are wind and tidal energy. Both sources operate on the same principles, but with different strengths and weaknesses. Tides are created by the moon and sun's gravitational pull and exist as a cycle of low- and high tides. Although tidal forces rotate the turbine blades at a much slower rate, seawater is much denser than air, resulting in potentially higher power output - at the expense of size and higher manufacturing costs [2].

Tidal energy has seen rapid development over recent years, with several developers now conducting offshore trials of full-scale prototypes, generating electricity for the grid [3]. One Scottish company, Nova Innovation, was in 2016 the first company to successfully deliver an offshore array of several 100 kW tidal turbines, in Bluemull Sound, Shetland [4].

In a similar fashion, the need for efficiency and cost reduction has produced exciting new research and innovation in the offshore wind sector. Hence an approach to multi-rotor wind turbines as a possible replacement for conventional wind farms is exemplified by the Norwegian company Wind Catching [5], proposing that 5 of their units can produce electricity equivalent to 25 conventional turbines.

A significant step in the process of developing new technologies is the use of scaled model testing. Although a large body of literature reports on experimental testing of turbine models, limited information on the actual design and manufacturing of the models is available [3]. G.S. Payne et al. [3] present details of the design and manufacturing techniques used to develop a highly instrumented turbine model, with the ability to measure streamwise root bending moment for each blade, estimation of wake development, and in addition, torque and thrust measurements for the overall rotor.

Experimental studies give the opportunity to validate data from numerical analysis and consequently predict turbine performance. This is shown by Masson and Smaili [6], which presented a numerical method for the simulation of turbulent flow around the nacelle of a horizontal axis wind turbine. Accordingly, simulation results were compared with experimental data, which resulted in good qualitative agreements that validated the proposed methods.

Equally important, model testing offers great savings when compared to full-scale tests. However, it can still become an expensive undertaking. The larger the model, the better the test data, and the easier it is to scale up to the prototype values; but the cost of the model test can also increase substantially [7].

In this thesis, the design, manufacturing, and testing process of a model scale horizontal axis turbine will be conducted. The design is an extension of previous work by Associate Professor David Lande-Sudall and a team of lab engineers at Høgskulen på Vestlandet (HVL). The aim is to revamp several design parameters that inhibited the prior project's further progression and consequently develop a model for testing in MarinLab.

2 Theory

This chapter presents the necessary theory in order to get a better understanding of the contents encountered in this thesis.

2.1 Model scaling

Similarity between model and full-scale conditions is essential in order to obtain accurate testing results. Geometric, kinematic, and dynamic similarities are the principal elements of successful model testing. The primary forces encountered in model tests are gravity, inertia, viscous, and drag forces. Scaling laws are determined from the ratio of these forces, which are used to achieve a similitude between the prototype and the model [7]. Experiments conducted in wave basins are predominately influenced by inertia and gravity, hence the similarity in the Froude number, Equation (1), ensures that these forces are correctly scaled.

$$Fr = \frac{V}{\sqrt{gL}} \sim \frac{\text{Inertial force}}{\text{Gravity force}} \quad (1)$$

Here, V represents velocity, L is the length of the object in the flow direction, and g is the acceleration of gravity. Geometric similarity as seen in Table 2.1 is achieved by Froude-scaling the model size by a factor of λ . Consequently, all other necessary scales can be derived from these three basic units of length, mass, and time.

| Quantity | Unit | Scaling | Conversion |
|----------|------|------------------|----------------------------|
| Length | [m] | λ | $L_f = L_m \lambda$ |
| Mass | [kg] | λ^3 | $\Delta_f = L_m \lambda^3$ |
| Time | [s] | $\sqrt{\lambda}$ | $T_f = T_m \sqrt{\lambda}$ |

Table 2.1: Froude model scaling.

Wind tunnel experiments commonly use Reynolds number scaling to establish model parameters to properly represent the relationship between viscous and inertial forces in the airflow [8]. Although the Reynolds number plays a vital role in many fluid flow problems, achieving similitude is very demanding practically [7]. As seen in Equation (2), downscaling of the model size requires a proportional increase in either velocity, density or viscosity to achieve equality, potentially resulting in absurdly high numbers. Conclusively, the use of Froude scaling prevents many practical problems, the major one being model speed, and in addition, similarity can be achieved even when the model fluid is different from the prototype fluid [8].

$$Re = \frac{\rho V d}{\mu} = \frac{VL}{\nu} \sim \frac{\text{Inertial force}}{\text{Viscous force}} \quad (2)$$

The Reynolds number is a dimensionless number, where ρ is the density of the fluid, V is the velocity, L is the length, μ is dynamic viscosity and ν is kinematic viscosity.

2.2 Momentum theory

A turbine generates electric energy by converting kinetic energy from a fluid, to rotation in a generator. The extraction is typically done by a rotor involving several foil-shaped turbine blades. An idealised representation, called the actuator disc model, denotes a technique for analysing rotor performance. In this model, the rotor can be simplified as a permeable, non-rotating actuator disc, with stationary, incompressible and frictionless flow around the disc [9]. The rotary disc resembles a circle, with a radius equal to the blade length. The amount of theoretical kinetic energy can be expressed as

$$E = \frac{1}{2} m V^2 \quad (3)$$

The amount of power generated by the fluid can be calculated with

$$P_{Fluid} = \frac{1}{2} \dot{m} V^2 = \frac{1}{2} \rho A V^3 \quad (4)$$

In this equation, the mass flow rate of the fluid \dot{m} is defined as the relationship between density ρ , area A and velocity V . The change in momentum can be found by examining the pressure and velocity at both sides of the rotary disc. The Bernoulli equation is used to calculate this change, and is expressed by

$$P_0 + \frac{1}{2} \rho V_0^2 = P_3 + \frac{1}{2} \rho V_3^2 \quad (5)$$

A short upstream distance away from the disc, the velocity continuously decreases until it stabilizes a distance downstream from the disc. Meanwhile, the pressure increases a short distance upstream from the disc, and eventually reaches a sharp drop, where it immediately continues to increase after passing the disc. This effect is illustrated in Figure 2.1

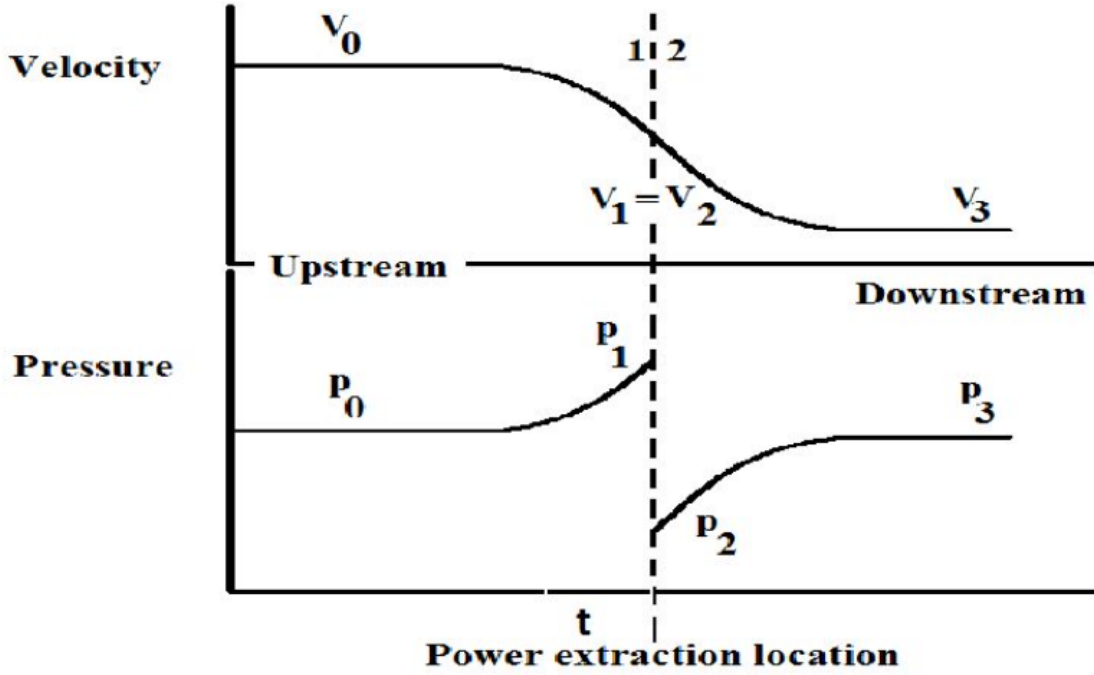


Figure 2.1: 1-D momentum theory [10].

By using Bernoulli's equation and the axial induction factor a , to define the velocity between the cross-section and upstream position, the power output of the turbine can be given by

$$P_{Turbine} = \frac{1}{2} \rho A V^3 4a(1-a)^2 \quad (6)$$

From linear momentum theory and Newton's third law of motion, the turbine blades has an equal and opposite force to the incoming fluid. The thrust, T which affects the turbine is given by the mass flow rate at the power extraction location multiplied by the change in velocity before and after.

$$T_{Turbine} = \rho V_t A_t (V_0 - V_3) \quad (7)$$

Commonly the power coefficient C_P is used to quantify the efficiency of wind power. The power coefficient can also be defined as the ratio of the energy extracted from the fluid, divided by the energy contained in the fluid.

$$C_P = \frac{P}{\frac{1}{2} \rho V_0^3 A_t} = \frac{P_{Turbine}}{P_{Fluid}} \quad (8)$$

The thrust coefficient C_T can be found by rearranging Equation (7), and accordingly be used to find the load on the turbine induced by the fluid energy expressed by

$$C_T = \frac{T_{Turbine}}{\frac{1}{2} \rho V_0^2 A_t} \quad (9)$$

Further study reveals the existence of a maximum theoretical amount of power extractable for a turbine. This limit is known as the *Betz limit*. The law states that it is not possible for a turbine to extract more than 16/27 or 59.3% of the total kinetic energy. In other words, the highest theoretical power coefficient a conventional turbine can attain is $C_P = 0.593$.

2.3 Drag

Drag is the force component acting opposite to an object's relative direction of motion through a fluid. Thrust is often used interchangeably with drag, but is generally used for objects like propellers, turbines and jet engines. In this thesis, the term drag is used, since the experimental study inspects the drag force of different nacelles shapes. The magnitude of the drag force is dependent on an object's speed, shape, size and angle of attack, in addition to the working fluid's density, viscosity and compressibility. The relationship between these parameters is generally very complex but can be condensed into a single variable called the drag coefficient C_D [11]. This makes it possible to collect all the above effects into a single equation and find the drag force F_D , expressed by

$$F_D = \frac{1}{2} C_D \rho A V^2 \quad (10)$$

Where ρ is the fluid density, A is the projected area, and V is the velocity. Drag is generally divided into two main types, shear force (skin-friction drag) and pressure-induced drag (form drag). Streamlined bodies like foils are affected mainly by skin-friction drag since the cross-sectional area is low relative to its surface area. Skin-friction drag occurs when the fluid touching the surface is brought to rest from shear stress at the wall. This phenomenon is known as the no-slip condition, and is caused by viscous effects. The section between the mainstream and stationary flow is called the boundary layer. The rate at which the stationary flow transitions to mainstream flow in the boundary layer is determined by the surface roughness of the body, and the turbulence of the surrounding fluid. The coefficient by which a body is affected by skin friction is the local wall shear stress τ_w and the free stream dynamic pressure p_{dyn} [12].

$$C_{f,friction} = \frac{\tau_w}{p_{dyn,\infty}} \quad (11)$$

Blunt objects like cylinders are mostly affected by pressure-induced drag since the cross-sectional area is higher relative to the surface area. In contrast to friction drag - where forces are tangential to the body, pressure drag forces are directed normal to the body. The pressure change that affects a submerged body in motion results from the conservation of energy, which can be expressed using Bernoulli's equation.

As the flow around a body accelerates, the surrounding pressure decreases, thus increasing the kinetic energy. When the surrounding fluid decelerates, the pressure increases at the cost of kinetic energy. As shown in Figure 2.2b, a body with higher pressure on the side facing the fluid flow and lower pressure on the side facing away - is affected by pressure drag due to this pressure difference.

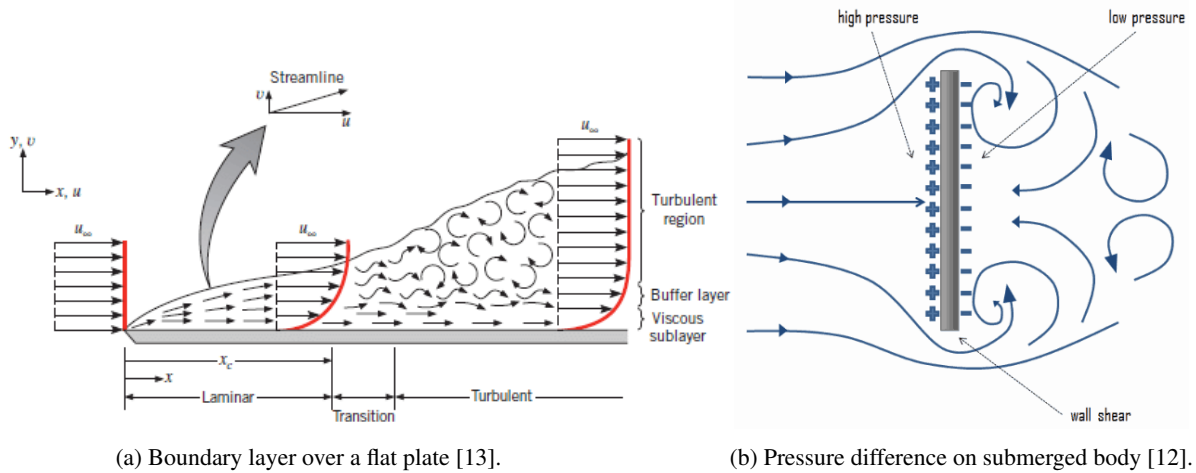


Figure 2.2: Skin friction and pressure drag.

The dimensionless pressure coefficient can be defined as the static pressure difference Δp_{stat} , divided by the free stream dynamic pressure p_{dyn} expressed as

$$C_{p,pressure} = \frac{\Delta p_{stat}}{p_{dyn,\infty}} \quad (12)$$

An approximation of how an object will be affected by drag forces can be made by relating the Reynolds number to the drag coefficient C_D . Figure 2.3 depicts the drag coefficient of a cylinder, sphere and disc as a logarithmic function of the Reynolds number in transverse flow. As illustrated, the drag coefficient decreases as the Reynolds number increases.

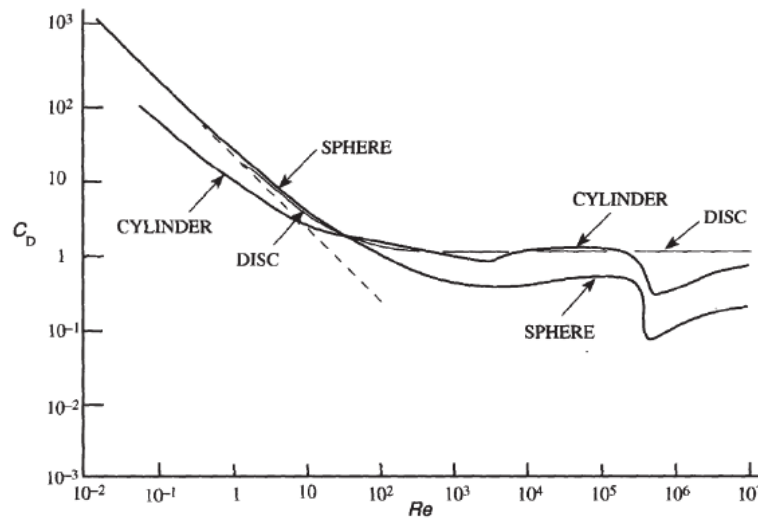


Figure 2.3: Drag coefficients of a cylinder, sphere and disc as a function of Reynolds number [14].

When an object has smooth transitions in its contour, the internal cohesion between the fluid is greater than the surrounding forces. The flow follows the object's contour, and a boundary layer is developed. When the flow no longer follows the contour and detaches, flow separation occurs. This occurrence applies to both streamlined- and blunt objects. In the latter case, flow separation occurs as the flow velocity declines and the pressure increases. Static pressure in the resulting wake, pushes flow in the opposite direction. This force causes vortices to form and an increase in turbulence. This effect is illustrated in Figure 2.4.

At high Reynolds numbers, the inertial force is dominant compared to the viscous force, which increases the likelihood of flow separation. In other words, a turbulent flow changes the steepness of the velocity gradient in the boundary layer, thus producing an accelerated flow around the object's surface. The increase in kinetic energy affects the wake-pressure, consequently moving the separation point further downstream. The resulting wake becomes narrower because of the higher velocity gradient. After the flow has separated from the body, shear forces between the object and the body are reduced drastically, and the skin friction drag becomes negligible. As the energy in the flow transitions to turbulence in the wake, the pressure drops and leads to a significant increase in pressure drag.

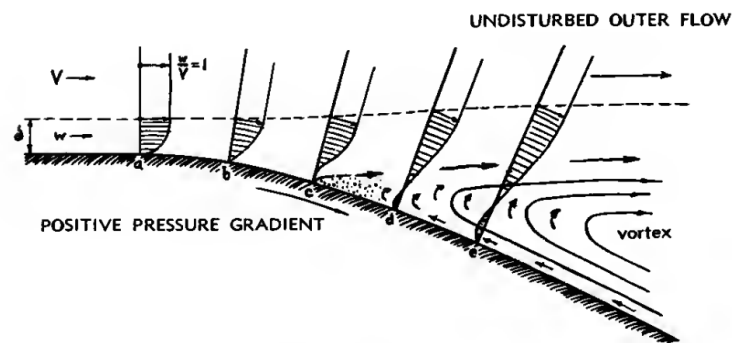


Figure 2.4: Flow separation [15].

When the Reynolds number is sufficiently high, the drag coefficient attains a more linear form, becoming independent from the Reynolds number. In these turbulent flows, the drag coefficient can be represented as a function of its body shape. Figure 2.5 illustrates this, with the drag coefficient of a blunt- and streamlined cylinder as a function of slenderness.

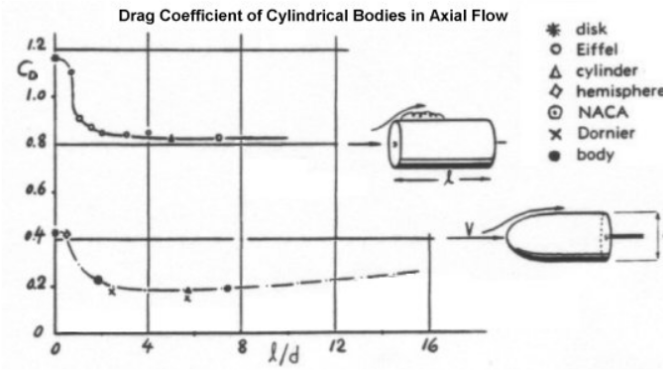


Figure 2.5: Drag coefficients of cylindrical bodies [16].

The significance of the Reynolds number is revealed in a study from the Journal of Energy Engineering [17], where six airfoils are tested, containing the most common Reynolds numbers used in commercial applications. The main discovery reveals greater turbine performance when the Reynolds number is increased. Notable parameters include a higher lift coefficient, lower drag coefficient and a larger lift-to-drag ratio. Additionally, a performance increase occurs when the foils operate at an optimised angle of attack.

Generally, model scale turbines will experience lower inertial forces due to relatively low sizes yet will encounter the same viscous forces - resulting in a lower Reynolds number. In Table 2.2, different types of turbines are compared to show advantages and disadvantages, and similarly, how the resulting thrust- and power coefficients, C_T and C_P , relate to the power output. The wind turbine data is obtained from a V117-4.2 MW turbine manufactured by Vestas [18]. The tidal turbine data is obtained from the manufacturer Atlantis, using the model type AR 1500 [19]. The different turbines are regarded to be among the average proportions in their respective field. The key takeaway is that wind- and tidal turbines operate at approximately the same Reynolds numbers, but in contrast, a mismatch in Reynolds number appears in model scale.

| Turbine | ρ [kg/m^3] | Speed [m/s] | Area [m^2] | Diameter [m] | Re | C_t | C_p | P [kW] |
|---------|---------------------|-----------------|----------------|------------------|----------|-------|-------|------------|
| Wind | 1.225 | 10 | 10751 | 117 | $8.13e7$ | 0.741 | 0.443 | 2915 |
| Tidal | 1025 | 3 | 254 | 18 | $5.54e7$ | 0.68 | 0.426 | 1500 |
| Model | 1000 | 0.9 | 0.28 | 0.6 | $5.4e5$ | 0.7 | 0.45 | 0.45 |

Table 2.2: Comparing different turbines.

2.4 Vortex-induced vibrations

A common problem within experimental research, is the ability to consistently procure data without excessive noise generation or other factors of disturbance. One influential disturbance is vortex-induced vibration (VIV), which occurs when shedding vortices exert oscillatory forces on a cylinder. This force acts in all directions, but mainly in the direction perpendicular to the flow. The structure starts to oscillate due to these forces if not corrected [20]. For fixed cylinders, the frequency of vortex shedding is related to the Strouhal number

$$St = \frac{fD}{V} \tag{13}$$

Where f is the frequency of vortex shedding, D is the cylinder diameter, and V is flow velocity. For cylindrical structures, the Strouhal number can be assumed constant (≈ 0.2) for $1000 < Re < 100.000$ [21].

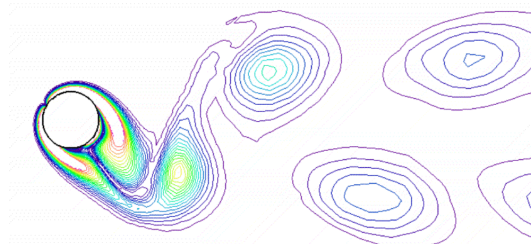


Figure 2.6: Flow induced vibrations on a cylinder generating vortices in the wake [22].

The experimental setup of the turbine tower could be seen as a fixed cantilever beam, shown in Figure 2.7, with the wave load applied at the free end of the tower. The maximum theoretical deflection is then given as

$$\delta = \frac{FL^3}{3EI} \quad (14)$$

Where F is the applied force, L is characteristic length, E is modulus of elasticity and I is the second moment of area. By using Hooke's law and rearranging in terms of a cantilever beam, the new spring constant is obtained

$$k = \frac{3EI}{L^3} \quad (15)$$

If the natural frequency of the cylinder f_n is close to the Strouhal frequency, *lock-in* or near resonance vibrations may occur [20]. This phenomenon is undesirable and could result in large body movements - which should be avoided at any rate.

$$f_n = \frac{1}{2\pi} \sqrt{\frac{k}{m}} \quad (16)$$

Where k is the spring constant, and m is the total mass.

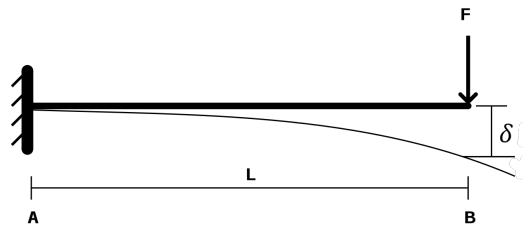


Figure 2.7: Deflection of a cantilever beam [23].

3 Design and construction

3.1 Design process

The overall design method is inspired by a typical design thinking process with modifications as seen in Figure 3.1. Extensive research is required on the topic, and an iterative process is used to develop a solution. The most promising solutions are then discussed with the team, including the lab engineers at HVL. After a complete 3D model draft is created in Autodesk Inventor, several revisions are made with regard to feedback from all involved personnel.

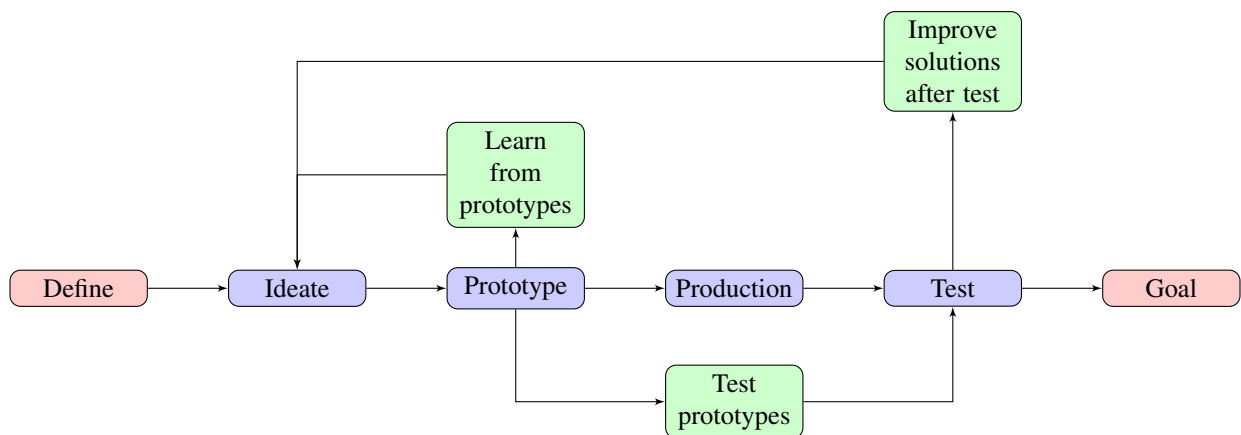


Figure 3.1: Non-linear design thinking process.

The outcome of this procedure is four different versions to consider, all with different strengths and weaknesses, as seen in Figure 3.2. Two of the most promising versions are then chosen, and prototypes are created using 3D printing. This makes it possible to better understand all the involved components and find the best candidate. The prototypes are inspected by the lab engineers to ensure production friendliness to avoid problems during manufacturing. Furthermore, several tests

are carried out on the 3D-printed prototypes during the experimental phase of the project. In the end, a final design is chosen for production and tests are carried out to verify that the goal is achieved.

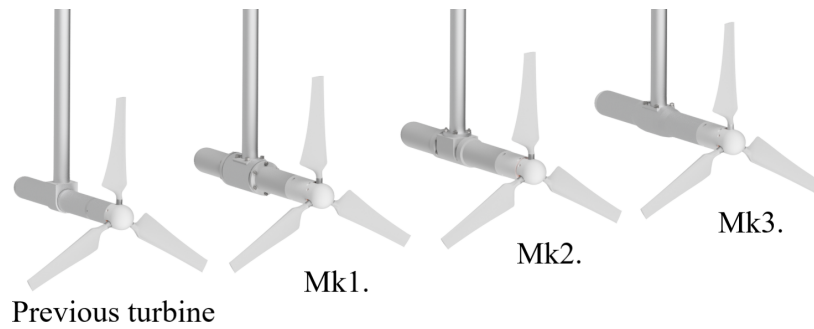


Figure 3.2: Design revisions.

3.2 Design and components

The previous model designed at HVL laid the foundation for the overall design and the required parts. Therefore, most of the powertrain components are implemented into the new design to save time and prevent unnecessary use of resources on developing already existing and proven solutions. However, the previous design was shown to have some significant faults in the nacelle design, which has been necessary to develop further.

There is a need to map all the involved components during the initial design phase. A good way to manage this is to use a product breakdown structure (PBS) of the turbine. A PBS is a valuable tool for planning, assessment, documentation, and displaying the involved components in a project using a hierarchical tree structure [24]. As seen in Figure 3.3, a visual representation of the required components in relation to their fundamental classifications is provided.

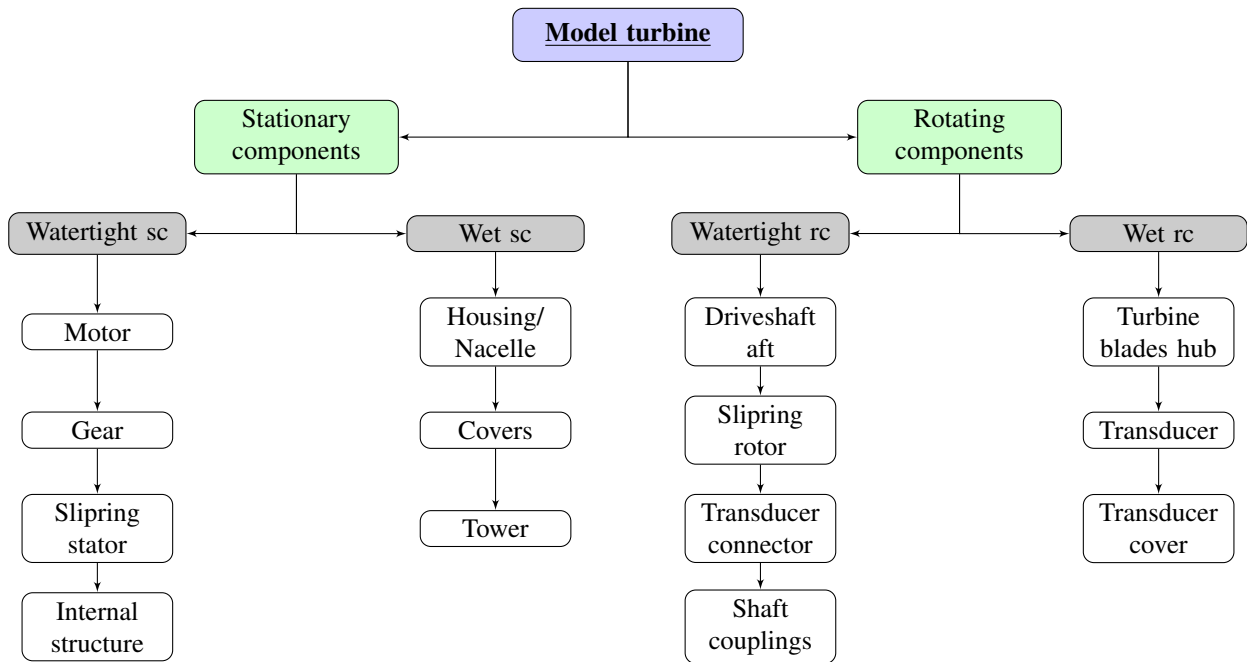


Figure 3.3: Product breakdown structure of main components.

The following section describes the complete turbine model layout in detail from the hub downstream to the motor/generator. To support the description, a section view of the production-ready turbine is displayed in Figure 3.4.

The driveline consists of components to connect the turbine hub to the electric motor and further transfer signals back to the LabView interpreter software. To achieve this in the best possible way, the configuration has to be arranged thoughtfully to avoid undesirable effects. At the front of the nacelle, a nosecone is connected to allow the incoming fluid a smooth transition onto the nacelle for drag reduction. Behind the nosecone, a hub is situated to mount the turbine blades. The hub allows for fully adjustable pitch angles for the blades to simulate different situations with various angles of attack. Additionally, the force transducer is bolted directly onto the hub, transferring the power to the front driveshaft.

Furthermore, a cover is attached to the transducer to compensate for the difference in diameter between the nacelle housing and transducer body.

A wire connector is attached to the back flange of the transducer. A hollow drive shaft is mounted behind the transducer to accommodate the wire and sensor connector while routing the wires back to the slip ring. The same driveshaft separates the dry and wet environments using two radial lip-seals. The hollow driveshaft is connected to a smaller diameter solid driveshaft with a shaft connector, illustrated in dark green. Although this solution might be less reliable than a one-piece driveshaft, it is necessary to help the assembly/disassembly of the turbine.

A cage structure, shown in red, is used around the slip ring to allow for easy access while the inside components are aligned. Furthermore, two bearings are situated in the front of the turbine to support the driveshafts. The selection of the bearings is mainly driven by their dimensions because the load and speed rating are generally over-dimensioned for such applications.

In the middle of the turbine, three green flanges are connected to a common boss, making it easy to separate the three ends. The solid drive shaft is then connected to the gearbox via a flexible jaw coupling to damp vibrations and protect the components in the drivetrain. The gearbox and motor unit are bolted to the rear flange, making it an integrated load-bearing structure.

The cooling sleeve has the primary task of transferring heat from the motor to the surrounding water. Secondly, it works as a seal housing with connection points for the rear end plate, shown in yellow. This makes it possible to transfer a compressing, lengthwise force onto the waterproofing sleeve to seal the nacelle's rear end. The same principle is used at the nacelle's front, where the end plate is connected to the bearing/seal housing. Finally, the tower flange is welded to the tower and attached with bolts to the boss. Several o-rings are then used in key areas to avoid any water intrusion. Further assembly information and bill of materials can be investigated in Appendix B and D.

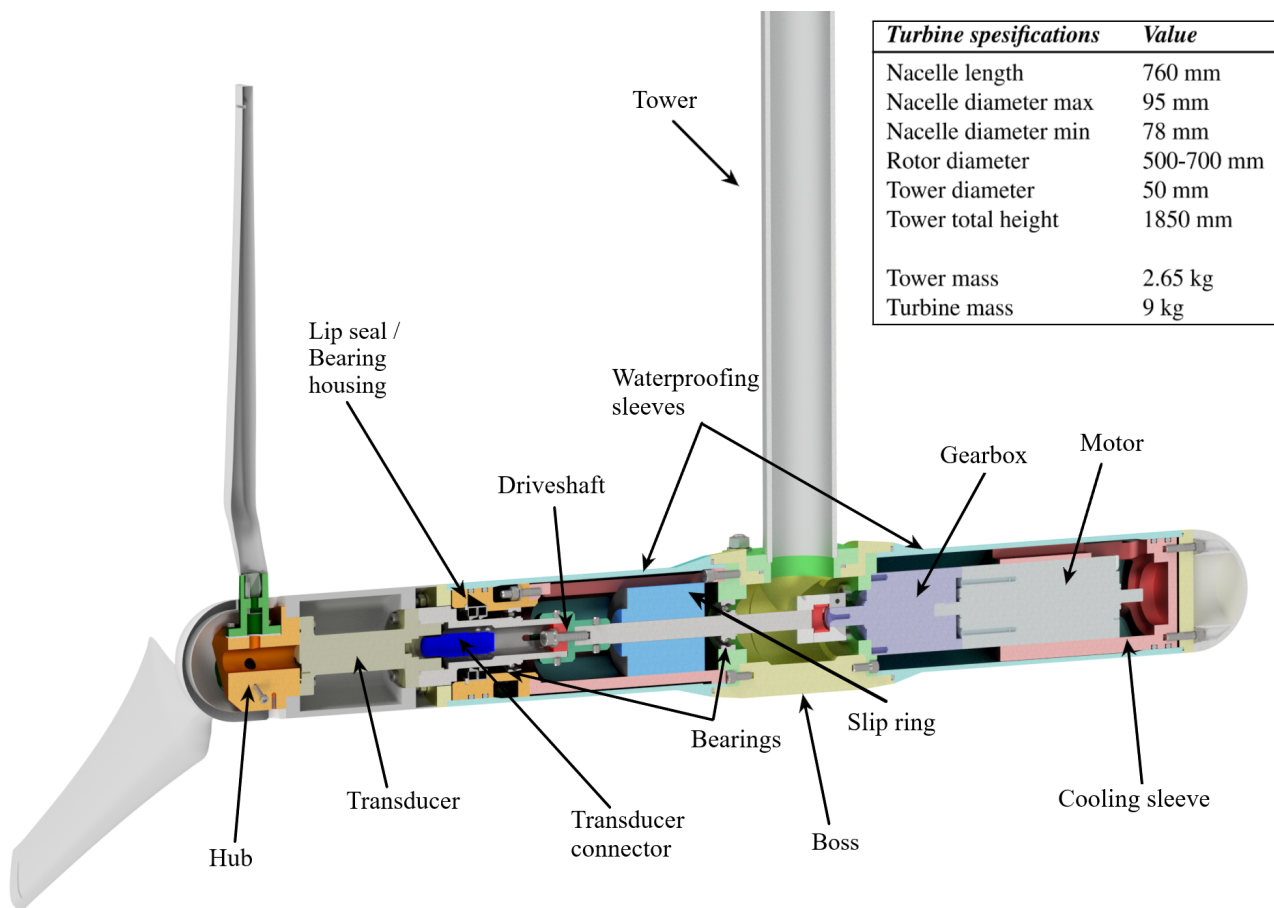


Figure 3.4: Cross-section view of the model turbine with specifications.

3.2.1 Instrumentation

The purpose of the turbine is to gather blade-characteristics data. This is done by measuring the torque and thrust induced by the blades onto the driveshaft. Several components are needed to gather this data, and a force transducer must be situated in the nacelle.

A transducer gets exposed to an input energy signal and responds with an output signal. In this case, the input energy is the reaction force from the turbine blades from the water flow. Consequently, a response signal is produced. This signal is interpreted in a processing unit as torque Q , and thrust T along the turbine's rotation axis, as shown in Figure 3.5. The transducer is a type 297 transducer made as a special order from the hydrodynamic research institution "Marin", situated in the Netherlands [25].

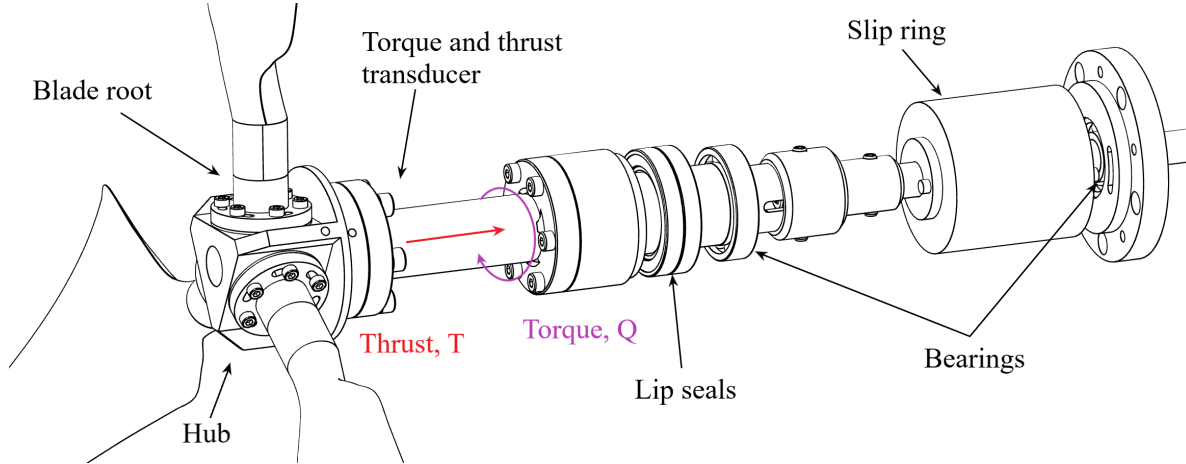


Figure 3.5: Close up view of torque and thrust transducer arrangement with forward drive line.

The transducer has flanges on both ends and is capable of absorbing large bending moments that may occur during testing. Despite its primary area of use as a wind turbine transducer, it can be used underwater due to its waterproof design - involving sealing solutions on both ends. As Figure 3.5 suggests, the transducer is situated as far upstream as possible. According to the producer, this should prevent frictional parasitic effects of bearings and seals, which means that no loss correction has to be accounted for. The transducer is dimensioned appropriately to deal with the expected forces for the given blades and velocity settings for accurate measurements, as seen in Table 3.1.

| <i>Measured Signal</i> | <i>Operating range</i> | <i>Sensitivity</i> |
|------------------------|------------------------|--------------------|
| Torque | 5 Nm | 0.006 Nm |
| Thrust | 100 N | 0.23 N |

Table 3.1: Measuring range and sensitivity of the transducer.

Since the transducer is directly bolted to the turbine hub, it will naturally rotate together with the turbine shaft. However, the wires cannot naturally follow this rotation due to movement constraints. Such a problem has mainly three solutions; rotary transformers, inductive/radio telemetry or slip rings. These components allow a cable signal to be transferred from a rotating part to a stationary part without using a directly connected cable. Since a slip ring was already available from the previous model, it became the natural choice. Typically, a slip ring consists of a rotating metal ring connected to the rotating shaft. In addition, an outer stationary graphite brush will then be rubbing against the ring and making the electrical connection. Slip rings are relatively cheap and easy to implement but are subjected to wear over time, and the signal can appear as noisy.

3.2.2 Powertrain

The primary goal of a turbine is typically to convert the energy from a fluid stream to usable electrical energy. This is achieved by installing a generator to the turbine shaft, either directly or through a gearbox. However, the setup for this turbine will not focus on actual power generation but rather on performing measurements and gathering relevant data. For this reason, the generator is replaced with an electric stepper motor. The motor will be used as a resistance against the torque coming from the turbine blades. This allows for a controlled and monitored surveillance of the applied resistance and angular position through dedicated processing units and software. The gearbox and motor is delivered as a modular package from the Swiss manufacturer "Maxon" [26]. The gearbox is a planetary gearhead, GP 52 C, with a 12:1 gear ratio. This is constrained to the high torque, brushless stepper motor, EC-i-52.

When the motor is operated as a generator, it is expected to deliver a much degraded efficiency. A large portion of the energy will then be lost to heat. Therefore, overheating of the components may be an unwanted effect. Effective heat transfer depends on direct contact between the motor and a cooling fluid. To cope with this, an aluminium cooling sleeve is installed around the motor, as seen in Figure 3.6. This allows the motor to be indirectly in contact with the outside water without an insulating layer of air between the parts.

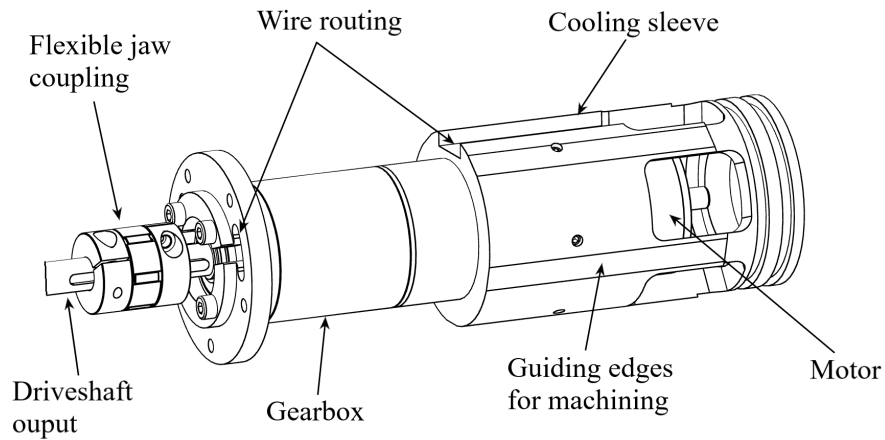


Figure 3.6: Close up view of drive system arrangement.

The transducer and motor have several wires running from each end of the nacelle back to the tower. In order to make a useable solution, the wire routing arrangement was prioritised from the initial design phase. Unlike the turbine produced by G.S. Payne et al. [3] in 2017, the wires from the motor are chosen to be routed inside the nacelle, as seen in Figure 3.7b. This is made possible by increasing the inside diameter of the nacelle housing to situate the cooling sleeve and wires. The most significant advantage of this solution is eliminating sealing solutions for an externally routed cable and a cleaner exterior design.

In the forward section of the turbine, the transducer wire arrangement must allow for a complete separation of the transducer from the rest of the assembly. This is made possible with a transducer connector and the two-piece driveshaft solution, as seen in Figure 3.7a. Depending on the wire connector of the tower side of the slip ring, it might be necessary to expand the kidney slot. This would allow the wires, including the connector, to be inserted through the slots without intrusion. However, such a decision must be taken later in the process when the electrical connector is known.

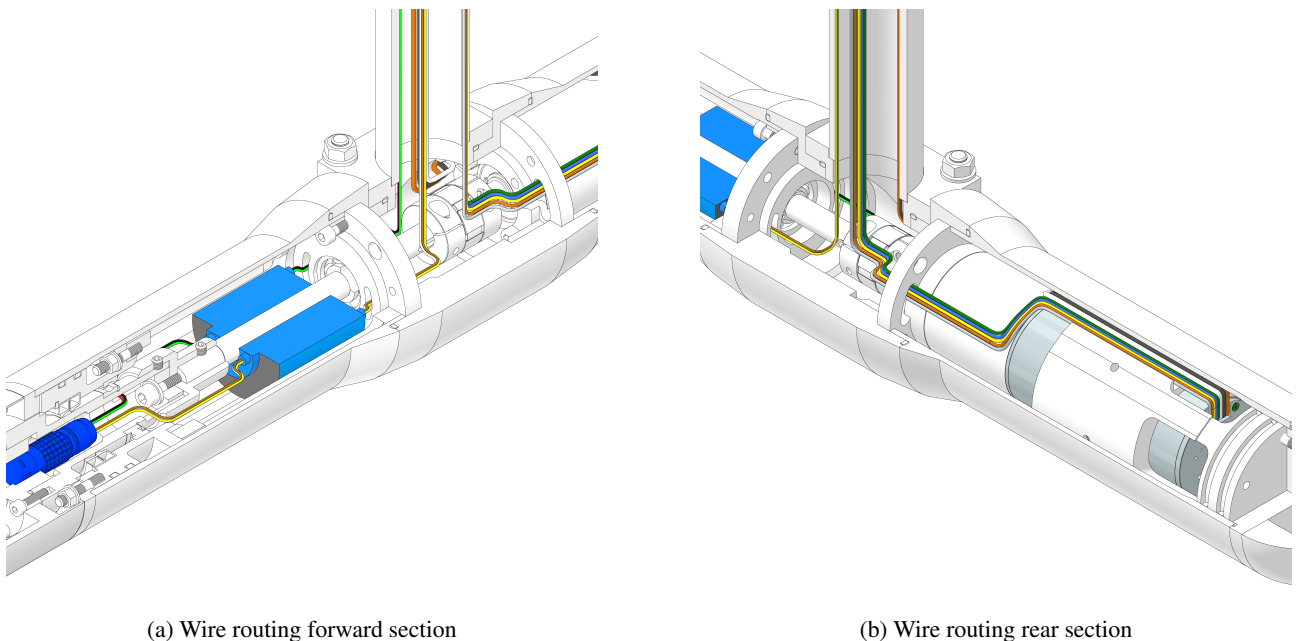


Figure 3.7: Wire routing from components to tower.

3.3 Material selection

A crucial aspect of product design is the material selection process. The main objective of this process is to identify the general design criteria and find a suitable material which reduces costs while meeting the product performance goals [27]. The material design industry is in constant development, and it is estimated to be more than 100.000 materials available for engineers to choose from [28]. This can make the task of selecting a material quite time-consuming and costly if all parameters should be taken into account. In addition, materials will rarely satisfy all needed requirements. Consequently, projects with limited resources must constrain the selection and prioritise key objectives, therefore, reasonable compromises might be necessary to fulfil the design requirements. Initially, a rough overview of important material characteristics needed to identify desirable properties related to the actual application. As seen in Table 3.2, a general categorisation table is used to illustrate the further selection process.

| <i>Category</i> | <i>Typical desirable properties</i> | <i>Main application</i> |
|-----------------|---|--|
| Mechanical | { Strength Toughness Stiffness | { Machinery Load bearing structure |
| Chemical | { Oxidation resistance Corrosion resistance UV radiation resistance | { Chemical plant Power plant Marine structures Outdoor structures |
| Physical | { Thermal conductivity Electrical conductivity Magnetic properties | { Power transmissions Instrumentation Electrical machinery Electronics |
| Physical | Density | { Aerospace, outer space Reciprocating and rotating machinery High performance machinery |

Table 3.2: Elementary material categorisation [28].

The mechanical properties are important, because the structure will be affected by relatively large forces as water flows around it. Likewise, the material needs to have enough stiffness to avoid deflection, especially considering the slender and long tower connecting the turbine and platform. It is also key to choose a material that has good fabrication properties, which allows for reliable features to be made, such as threads.

In regard to the chemical properties, it is essential to choose a material that can cope with the operational environment for the structure. Since the turbine model will be used for testing in MarinLab, the material must be able to resist the destructive effects of water on a long term perspective without corroding or oxidising. Furthermore, the physical properties such as density will be of high importance because it affects the usability of the turbine. In addition, added mass can contribute to a more complicated and less accurate force reading since the load cell setup will be affected by it. And finally, a high thermal conductivity will be needed to transfer heat from the transmission and motor to avoid overheating.

The next step is to choose a class of material that best fits the desired properties found in Table 3.2. The list in Table 3.3 provides a brief rundown of the most general properties of different classes of materials. Without reservation, ceramics and composites are less relevant due to more complicated and resource-intensive processing methods. For these particular reasons, it is clear that the most promising materials will have the properties of metal.

| <i>Plastics</i> | <i>Metals</i> | <i>Ceramics</i> | <i>Composites</i> |
|-------------------------|---------------------------|--------------------------|-------------------|
| Weak | Strong | Strong | Strong |
| Compliant | Stiff | Brittle | Stiff |
| Durable | Tough | Durable | Low density |
| Temperature-sensitive | Electrically conducting | Refractory | Anisotropic |
| Electrically insulating | High thermal conductivity | Electrically insulating | |
| | | Low thermal conductivity | |

Table 3.3: General properties of material classes [28].

Besides the already mentioned aspects, a need to evaluate other factors such as cost, availability and manufacturing properties appear. These factors often lead to additional considerations because some materials may satisfy all criteria, but they might be difficult to acquire. In addition, the facilities, fabrication and manufacturing capabilities will impact the selection, and might differ widely. As a consequence, a clear understanding of the market, as well as good communication with the people in charge of production and material purchasing, will ease the process. All things considered, two materials emerge as the most favourable, which is aluminium alloy and stainless steel.

Aluminium and its alloys are characterised by a resistance to corrosion in most environments, relatively low density compared to steel ($2,7 \text{ g/cm}^3$ vs 8 g/cm^3) and high thermal and electrical conductivity allowing for good heat transferring properties [27]. Stainless steel contains high amounts of chromium (at least 11%) to prevent corrosion in various environments. This makes it suited for a wide range of applications and offers a harder and more durable surface with higher tensile strength compared to aluminium. With that in mind, it is beneficial to use stainless steel in components of high importance that demands good reliability, such as driveshaft parts. Table 3.4 displays relevant information for the two proposed materials for use in the load-bearing structures of the model turbine.

| <i>Properties</i> | <i>Units</i> | <i>Aluminium Alloy</i> | <i>Stainless steel</i> |
|-------------------------|------------------------------------|------------------------|------------------------|
| Grade | | EN AW 6082 T6 | EN 1.4401(316) |
| Material yield strength | $\sigma_y \text{ (N/mm}^2\text{)}$ | 260 | 220 |
| Young's modulus | $E \text{ (N/mm}^2\text{)}$ | 69.000 | 200.000 |
| Density | $\rho \text{ (g/cm}^3\text{)}$ | 2,7 | 8 |
| Thermal conductivity | $k \text{ (W/mK)}$ | 167 | 16 |

Table 3.4: Aluminium vs. Stainless steel properties.

The results from the selection process are shown in Figure 3.8. All driveshaft parts are coloured in red and indicate the use of stainless steel 316. 3D-printed parts are shown in green and are made of PLA+ plastic material. Since the PLA+ plastic reliability is unknown, the 3D-printed parts will only function as covers to improve the streamlined shape of the turbine. The rest of the turbine housing, excluding various components, are made of aluminium.

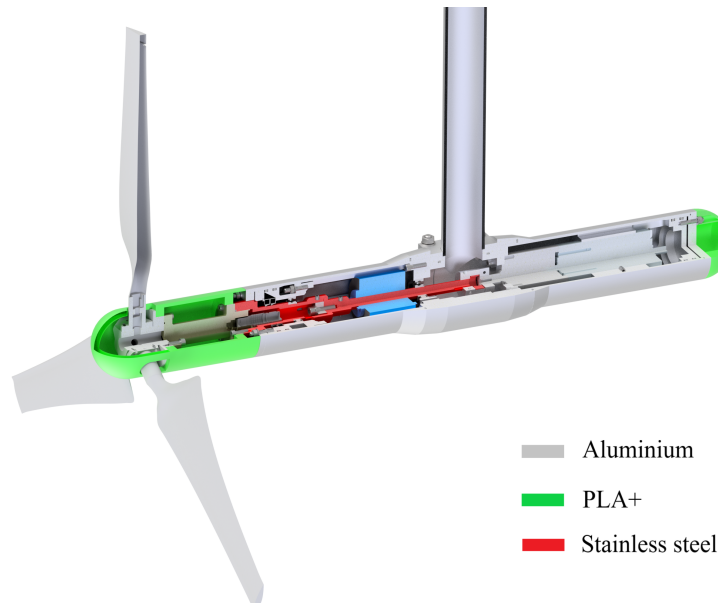


Figure 3.8: 3/4 section view with material specifications.

3.4 Waterproofing

The electrical components inside the housing are dependent on a dry environment to avoid malfunctioning. To establish a watertight section, several seals are used to avoid water intrusion. A variety of sealing solutions are available on the market to suit the current design. This design requires both static and dynamic seals and should ideally keep the cost and complexity to a minimum.

One of the most common seals used in the industry are o-rings. O-rings are designed to be cheap and easy to implement in any design. The two possible o-ring configurations are axial and radial. Both solutions are based on applying pressure between two components to compress the o-ring in its groove to create a seal. In axial compression, the watertight seal is established by pressing two flat surfaces together with the o-ring between them in the axial direction.

An example of axial compression can be seen in Figure 3.9a. In radial compression, the o-ring is used in a piston/cylinder configuration. Pressure is applied to the o-ring due to the tight tolerance between the two components. An example of radial compression can be seen in Figure 3.9b.

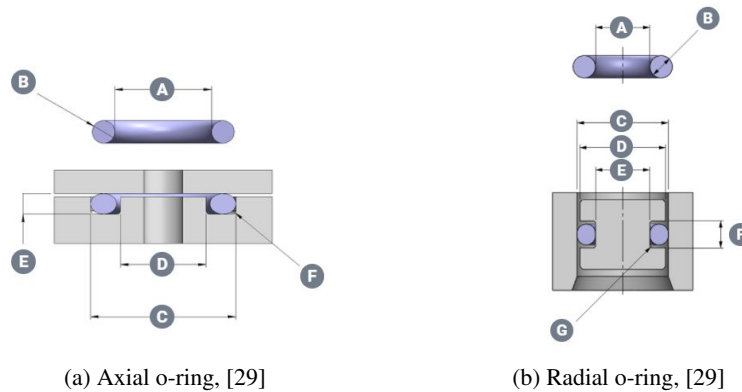


Figure 3.9: O-ring configuration design.

Correct dimensioning of the o-ring and groove is essential to create a reliable seal. First, the ISO 3601 standard is used for the selection process based on the diameter of the components. Secondly, the groove is adapted in accordance with the selected o-ring. The ISO standard also takes into account a stretch for the o-ring between 1-5% where a stretch of 2% is ideal in most applications. If the stretch is greater than 5%, it will result in a smaller cross section and potentially shorten the lifetime.

A suitable cross-section must be chosen when selecting an o-ring from the ISO table of dimensions. This measurement is illustrated with the letter "B" in Figure 3.9a. The distance between the inner and outer radius marked with the letters "D" and "C" in Figure 3.9a is equal to the thickness of the groove. The groove depth marked with an "E" is decided by the ISO standard following the cross section. The selected thickness is primarily driven by the available space and the ambient pressure. In general, a larger cross-section delivers a more reliable seal. As a result, three cross-sectional thicknesses are chosen: 1.75, 2.62 and 3.53mm.

While it might be tempting to use a radially configured o-ring in a rotating assembly, it is much more exposed to wear and failure this way. To solve this problem, an elastomeric radial lip seal is used - which is much more resilient to wear when used as a dynamic seal.

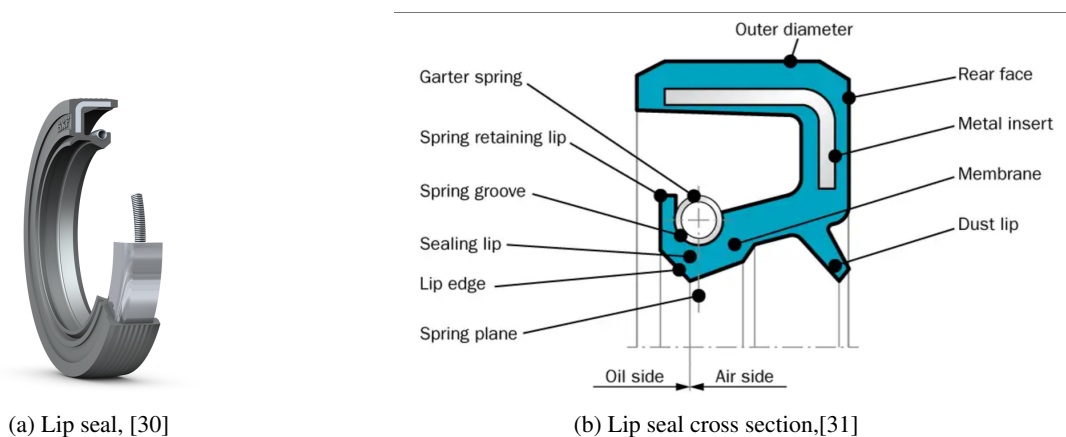


Figure 3.10: Lip seal.

The elastomeric radial lip seal is used throughout the industry to retain lubricants and exclude contaminants in rotating shaft applications [32]. Two lip seals are installed to ensure a proper seal at the rotating driveshaft, separating the dry and wet side of the assembly. In this context, a key consideration is the orientation of the lip seals. As seen in Figure 3.10b, the seal has an open side with a spiral garter spring attached. This side should in most cases be exposed to the high-pressure side to force the sealing lip edge onto the shaft. According to this instruction, the outer seal should have the spring side exposed to the water. The second, inner seal should face the opposite way. Between the seals and the bearing there is a slot with mechanical grease inserted. Such a solution allows for manual adjustment of the pressure by inserting more grease into the slot. This solution is developed by inspiration from industry propeller sleeves, and creates a reliable seal with high redundancy [3]. Further installation information can be found in Appendix D.

3.5 Rapid Prototyping

Rapid prototyping is the fabrication of prototype parts directly from a computer solid model without the need for expensive manufacturing methods [33]. This has become an essential part of the design process, and enables inexpensive and early detection of potential problems which could become critical in the final manufacturing stages. Components of the model is 3D-printed throughout the design process, and iterated upon until the final plastic model is ready. This model can be seen in Figure 3.11. In addition, the existence of a physical copy appends to the transparency of communication and exchange of ideas between the design- and lab engineers.

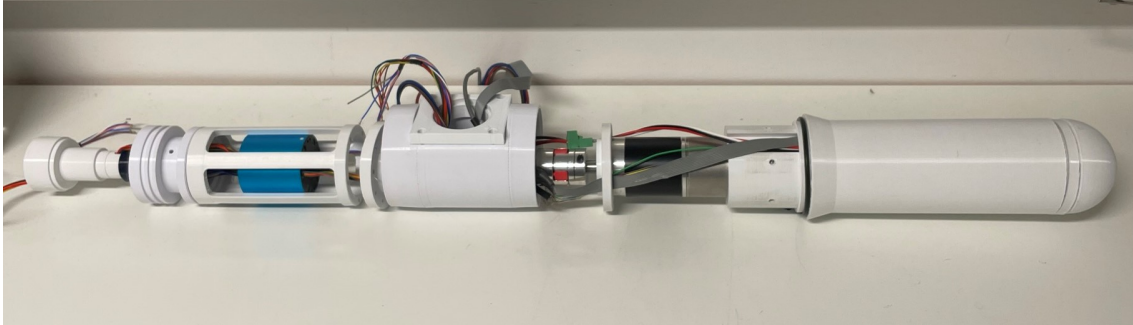


Figure 3.11: 3D-printed nacelle.

The prototyping stage makes use of 3D-printing to create the various physical components. Most of the components are printed using a Flashforge Creator 3, which enables large print volumes and good precision. In addition, the Flashforge Adventurer 3 and Adventurer 4 are also used simultaneously for smaller components, thus enabling a reduction of overall print time. The components are printed using the bioplastic material PLA+, with a print temperature of 220°, and a platform temperature of 70°. A nozzle size of 0.4 mm and a shell count of 3, results in a 1.2 mm solid wall thickness. The infill property is set to 20% for the larger parts, and 40% for the smaller parts in order to increase durability. The layer height is given as 0.18 mm with a travel speed of 70 mm/s, which gives a detailed resolution for the final product. As a result, the inexpensive prototype can be used as a dummy for further investigations.

| 3D-Printer | Print Volume [mm] | Print Precision [mm] |
|--------------|-------------------|----------------------|
| Creator 3 | 300x250x200 | ±0.2 |
| Adventurer 4 | 220x200x250 | ±0.2 |
| Adventurer 3 | 150x150x150 | ±0.1 |

Table 3.5: The main noticeable printer differences are the print volumes and accuracy.

3.5.1 Challenges

A common problem encountered with 3D-printing is the lack of ability to make adjustments to the final product. For instance, subsequent dimensional adjustments on aluminium components could be made with relative ease, due to the material's structural integrity [34]. With PLA plastic, this is not an easy task. The material starts to soften at around 60-70°, and has a melting point of around 175°. If a drill is used on a PLA component, the drill bit warms up, and starts to melt the material. Creating threads is another disadvantage for 3D-printed models. The printers used in this thesis encounters challenges when making thread holes for bolts, and even more capable printers encounter problems with the precision of thread-making. This is mainly due to the interpretation of the uploaded CAD-files. However, this problem is solved by adding a threadless hole to the part, using values seen in Table 3.6. Threads are then added with the use of a tap, with an increase in shell thickness to ensure structural integrity.

| Thread | Standard drill hole [mm] | Recommended drill hole PLA [mm] |
|--------|--------------------------|---------------------------------|
| M3 | 2.5 | 2.6 |
| M4 | 3.3 | 3.5 |
| M5 | 4.2 | 4.3 |
| M6 | 5 | 5.3 |
| M8 | 6.8 | 7.2 |

Table 3.6: Recommended hole sizes for threads [34].

3.6 Tolerances and fits

Many of the machined components relies heavily on dimensional precision to function properly. As a consequence, it is tempting to assign highly accurate tolerances throughout the construction. However, to avoid unnecessary costs and time-consuming machining, it is often wise to choose as course a tolerance as possible without sacrificing functionality. A good understanding of tolerances and fits is therefore needed. To execute this in a proper manner, the tolerances and fits for machining are chosen by following the recommendations given by ISO 286-1. In addition, all general and non specified, linear dimensions shall follow the NS-ISO 2768-1:1990 standard.

Despite designing each part with precise dimensions, there will be an inevitable inaccuracy resulting from the manufacturing process. The measured dimensions will rarely match the designed dimensions, therefore an upper and lower allowable dimensional limit is established, called the tolerance. After two parts are manufactured with regard to the given tolerances, the relative dimensional relationship between the two components will result in a fit. The fit can vary from a loose to an interfering fit, depending on the tolerances that are chosen. The three different types of fits can be characterised as follows [35]

- **Loose/Clearance fit**

- A clearance fit will always have a smaller shaft and a bigger hole. This allows the parts to be easily assembled without force, and leaves room for rotation and sliding motions between them.

- **Transition fit**

- A transition fit encompasses two possible outcomes. At one end of the spectre, the fit can be characterised as a clearance fit with a small amount of room between the two components. At the other end, the shaft may be slightly bigger than the hole, resulting in an interference fit where a small force is required to assemble the two parts.

- **Interference fit**

- Interference fits, also known as friction fits or press fits will always have a bigger shaft diameter compared to the hole. This is used to prevent motion between two parts, and holds the shaft in place using friction. Interference fits must be assembled using a large force or by heating the part containing the hole, and cooling the shaft to make a temporary loose fit.

The ISO 286-1 standard uses letters and numbers as notations to categorise the different levels in an organised manner. There are two options when choosing a system for a fit. The system must be based on a shaft or a hole basis, meaning that one part has a controlled measurement, and the other is made based on the previous measurement. As a main rule, the controlled measurement should touch the zero-line in either the upper or lower tolerance limit, and the letter H or h in the system implies which basis is being used. As seen in Figure 3.12, capital letters define the housing or hole tolerance, and the small letter defines the shaft tolerance. By closer inspection, it is possible to get a rough overview of the different tolerance notations in relation to each other.



Figure 3.12: ISO 286-1 system for tolerances [36].

Each class of fits has sub-categories with different demands for precision and tolerances. This begs the question of which fit-system is the most suitable for different applications. To assist the selection process, a recommendation table is presented in Figure 3.13, based on the given ISO tolerances.

| | recommended fits | |
|------------|---|---------------|
| basic hole | clearance fits | basic shaft |
| H8/d9 | loose running fit: clearance allows for loose fit of parts | D10/h9 |
| H8/e8 | free running fit: sufficient clearance is allowed for ease of assembly | E9/h9 |
| H8/f7 | close running fit: clearance allows for parts to be easily assembled by hand while maintaining location accuracy | F8/h9 |
| H7/f7 | sliding fit - free: clearance allows accurate location and free movement, including turning | F8/h6 |
| H7/g6 | sliding fit - constrained: clearance allows better location accuracy while still allowing sliding or turning movement | G7/h6 |
| H8/h9 | minimal clearance fit: allows location accuracy and hand force assembly without being a snug fit | H8/h9 |
| H7/h6 | locational clearance fit: Allows snug fit of stationary parts that may be assembled by hand force | H7/h6 |
| | transition fits | |
| H7/j6 | locational transition fit: for accurate location allowing more clearance than interference | not specified |
| H7/n6 | locational transition fit - interference: For accurate location where interference is permissible | |
| | interference fits | |
| H7/r6 | locational interference fit: for rigidity and alignment/accurate location without special bore requirements | not specified |
| H7/s6 | medium drive fit: for ordinary steel parts or shrink fits of light sections, tightest fit possible for cast iron | |
| H8/u8 | force fit: for parts fitting that can withstand high mechanical pressing force or shrink fitting | |
| H8/x8 | extreme force fit: for parts that can only be assembled by stretching or shrinking | |

Figure 3.13: Recommended fits from ISO 286-1 standard [37]

The model turbine involves all types of fits with selected tolerances to fulfil the functional specifications. A number of examples can be seen in Figure 3.14. The design allows the bearings to be permanently fixed without the need for further disassembly, meaning both bearings can have an interference fit. Furthermore, the cooling sleeve around the electrical motor needs a transition fit with the tightest possible tolerances, without actual interference. All other guiding edges are meant to be easily assembled and disassembled while keeping a snug fit. For this reason, the best solution is to use clearance fits closing in on transition fits, ranging from sliding to locational clearance fit. Further details on the exact tolerance decisions can be investigated from the drawings in Appendix B.

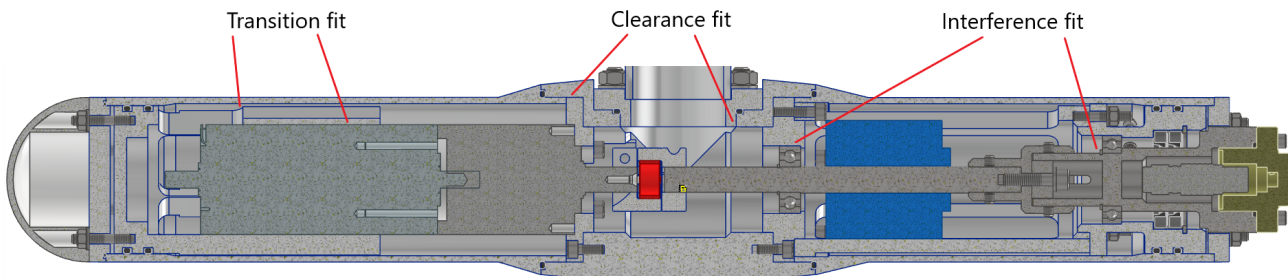


Figure 3.14: Example of different fits.

3.7 Assembly manual

Manual operations involve human interaction with the production lines and assembly procedures. As a result, the assembly manuals in their most basic form still play an important role in the transition zone, from semi-automated to fully automated assembly procedures. From an individual consumer perspective, it is not without reason that everyday products such as furniture, tools and other appliances are delivered with paper-based assembly manuals to aid the assembly process. These manuals should be easy to understand, effective to utilise and cheap to distribute. In small scale manufacturing, the basic assembly manual involving step by step procedures with exploded views is still one of the preferred methods to use for assembly aid.

As a result, a complete assembly manual of the model turbine is made to ease the learning curve for future users, and in addition, ensure proper maintenance in the coming years. The manual in its entirety can be found in Appendix D

4 Experimental method

Flow phenomena can be relatively easy to predict, given a laminar and simple case. Unfortunately, most real flows have a turbulent and unpredictable nature, making it time-consuming to perform accurate CFD simulations. For this purpose, it can be beneficial to conduct experiments to find and verify results against theoretical values. In this case, the dimensions of the new turbine have increased, and it is desirable to investigate the new characteristics. Consequently, several configurations are tested to confirm the effects of a streamlined body. Likewise, it is desirable to observe the behaviour of the test setup and compare any unwanted effects to similar experiments.

The results should clarify if the new turbine design has a negative impact on the flow around the nacelle. Ideally, the results will yield representative data of the new turbine that can contribute to new findings in the future. The experiments are conducted in the research facility MarinLab. The facility contains a medium-sized towing tank which is 2.2 meters deep, 3 meters wide and 50 meters long.

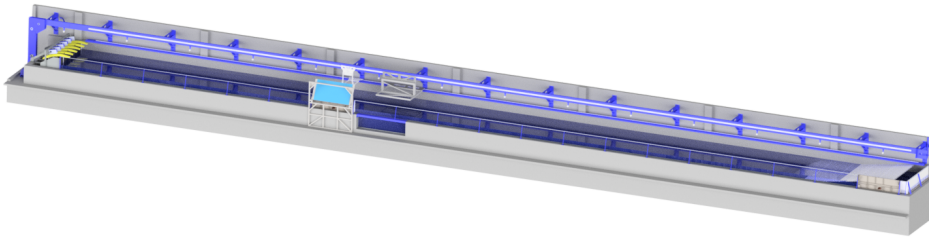


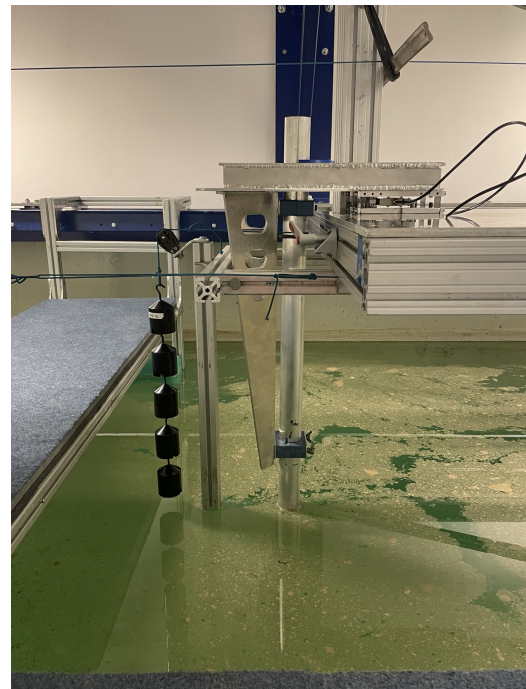
Figure 4.1: Towing tank in MarinLab at HVL.

4.1 Calibration of load cells

Arguably the most important step in experimental research is to ensure the proper configuration and validity of the measuring equipment. The load cell setup consists of a 50 N s-beam load cell, contained in a custom housing, with the ability to measure both tension and compression forces. In order to compare calibration accuracy, multiple different setups are tested, where two of the most consistent methods are explained. The first method shown in Figure 4.2a, uses a vice to constrain the housing vertically at a 90° angle. Shortly after, known loads are applied incrementally, and the LabView software interprets the output. The second calibration method is configured to simulate loading from the complete turbine setup, illustrated in Figure 4.2b. This method uses a pulley connected to a V-slot linear rail on the carriage. The linear rails allow the connection of the tower to the load cell.



(a) Calibration on land.



(b) Calibration in tank.

Figure 4.2: Load cell calibration.

In both cases, the known load, measured load and the deviation between them are noted for each weight applied. The outputs from LabView are imported into a custom spreadsheet for comparison. Linear regression is used in comparison to the best-fitting line representative of the data. From this, the correcting gain and offset values are extracted. Hysteresis in the calibration is found by comparing the average values from loading and unloading, and it is desirable to make this value as low as possible. Ultimately the second calibration method is chosen. Although some frictional forces appear due to the pulley, the benefits of including the load from the turbine setup could potentially mean a more accurate force measurement in later testing.

4.2 Carriage setup

The towing carriage is connected to a rail, and moves along the tank lengthwise. As seen in Figure 4.3, the tower and nacelle are fastened using screws, nuts, and clamps for quick and easy mounting. A custom aluminium bracket is made and functions as a connection from the turbine tower to the tower holder. The tower holder's purpose is to firmly hold the tower in place and evenly distribute forces to the load cell housing. The load cell housing consists of four main parts; top, bottom, flexible shims and a load cell. The load cell housing's base is connected to the carriage, and the housing's top is connected to the tower holder.

When the carriage moves, the tower and nacelle is affected by hydrodynamic drag forces; acting in the opposite direction. Forces are transferred through the tower holder, and to the top of the load cell housing. Two opposite facing forces acting on the top and bottom causes the flexible shims to bend slightly, and results in a displacement. As seen in Figure 4.3, the left and right side of the load cell is connected to the top and bottom housing part respectively. When the LabView program interprets the load cell data, a text file is generated which is further analysed using MATLAB.

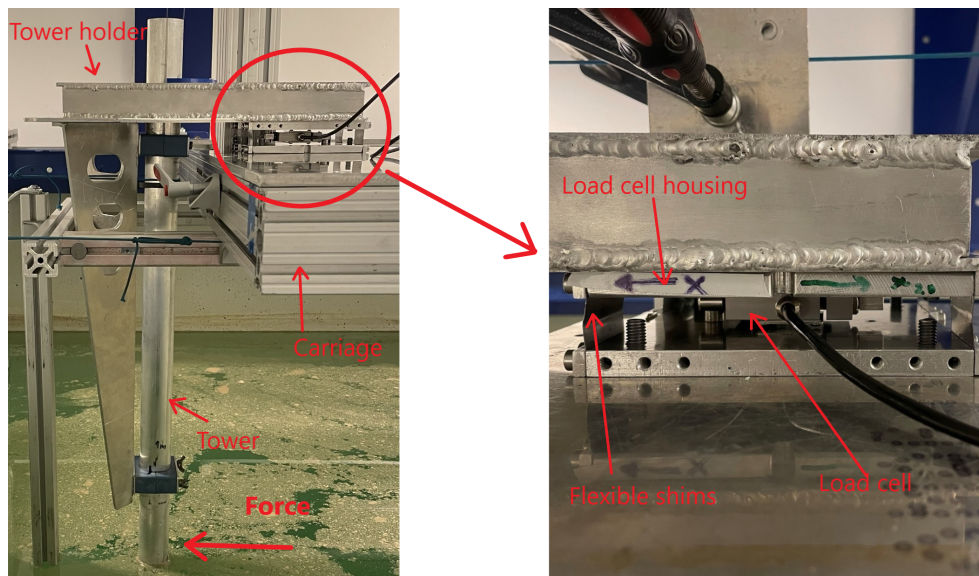


Figure 4.3: Load cell setup on the carriage.

In addition, small QR codes on the railing enable the carriage to monitor its relative position continuously. This results in a velocity curve that can be compared with the chosen velocity to find a potential deviation.



Figure 4.4: QR scanner on the carriage.

4.3 Tower and nacelle setup

Four different configurations of the nacelle and tower are used during testing as seen in Figure 4.5. In addition, two tests consisting of only the tower with and without added weight are performed.

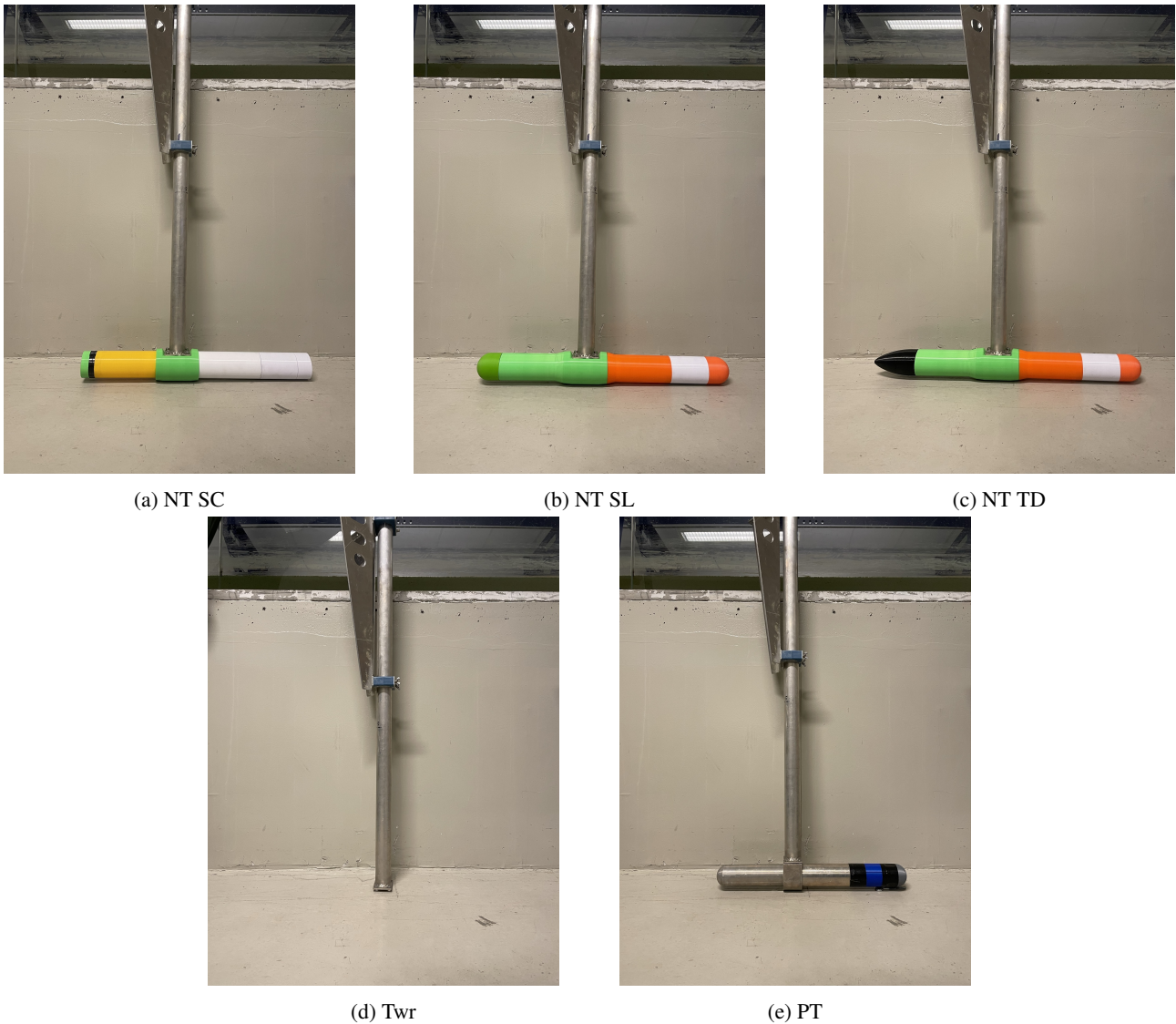


Figure 4.5: Nacelle configurations.

The nacelle configuration "NT SL" is a 3D-printed replica of the nacelle illustrated in Chapter 3. This replica mimics the shape of this nacelle to experience the same hydrodynamic forces approximately. The nacelle "NT TD" has an elongated end in an attempt to reduce pressure drag as a result of flow separation. The nacelle "NT SK" comprises sharp corners and flat surfaces, namely for an attempt to increase flow separation and pressure drag. All test objects consist of six segments with male and female threaded ends, making it possible to connect the different parts. In addition, all the thread dimensions are uniformly standardised to easily change the segments to a different configuration.

| Nacelle type Dimension type | Sharp corner | Streamline | Tear drop | Tower | Tower weighted | Previous Turbine |
|----------------------------------|--------------|------------|-----------|-----------|----------------|------------------|
| | Acronym | NT SC | NT SL | NT TD | Twr | Twr _w |
| Length [mm] | 700 | 700 | 830 | 1850 | 1850 | 600 |
| Weight [g] | 2300 | 2300 | 2300 | 2650 | 4950 | 2300 |
| Material | PLA | PLA | PLA | Aluminium | Aluminium | Aluminium + PLA |
| Projected area [m ²] | 7.09e-3 | 7.09e-3 | 7.09e-3 | 0.025 | 0.025 | 6.5e-3 |

Table 4.1: Tower and nacelle specifications.

VIV and drag forces will be affected by shape and form, and Table 4.1 shows a comparison between the configurations. The length of the nacelle and surface roughness of the chosen material is important for skin friction drag. The height of the tower and the resulting mass affects the structure's natural frequency. In addition, a larger projected area typically leads to an increased drag force. The towing test are carried out with velocities of 0.2, 0.4, 0.6, 0.9 and 1 m/s over a distance of 30 m. The acceleration and jerk is set to 0.2 m/s^2 and 0.2 m/s^3 respectively. To ensure minimal effect from boundary condition along the walls and water surface, the turbine is located 0.5 m beneath the surface in the middle of the tank. Furthermore, estimation of expected forces is done in advance to choose the correct load cell tolerance.

4.4 Sources of error

There will always be some amount of uncertainty or error during experimental research. These sources of error can generally be divided into two main categories, systematic and random error. Systematic error refers to an inaccuracy that is inherent in the measurement system. A common example of systematic error is not calibrating a load cell. All measurements taken with the load cell will be off by the same amount. Random errors are due to fluctuations in the conditions in which the measurements are taken. Random errors are unpredictable and usually not the same for each test, but can be reduced by attaining more data.

4.4.1 Systematic error

The most likely systematic error affecting the results is the load cell calibration. An example of this is hysteresis, which could reach as high as 0.14. Moreover, shims holding the load cell housing are slightly bent, resulting in a variable stiffness. As a consequence, the gain value used to calibrate the load cell could be slightly off. Periodic vibrations from the motor of the towing carriage generate noise which could introduce an error to the measurements. Though this error is small and is assumed to be negligible. In the earlier stages of testing, problems with a LabView sampling frequency of 10k Hz interfered with the accuracy of the results. A notable problem with this includes duplicate data points. This is corrected by reducing the frequency to the manufacturer's recommended value of 2k Hz.

Furthermore, the load cell housing has an additional floor to contain a second load cell. This extra level is necessary to connect both load cells, but causes additional sideways swaying during testing. In any case, this is regarded as obsolete due to only using a single cell in the experiments. To this end, the second floor is removed with the addition of custom drilled holes for mounting.

4.4.2 Random error

Undesirable oscillations of the tower occur at certain velocities, which could be explained by vortex-induced vibrations. A possible solution would be to attach strakes and fairings to the tower. The added strake elements will interfere with the shedding- and vortex process, potentially suppressing most of the resulting forces, and reducing overall VIV [38]. During testing of each different model setup, the equipment and the model itself is manually removed and assembled. Details like length and angle is marked with a permanent marker, but small changes in each test is still possible. Finally, wave reflections from the walls occurring after each experiment results in additional noise. This error is reduced by delaying the test runs appropriately.

4.5 Data processing

All measurements are recorded with a dedicated LabView program. The force readings are then converted to .txt files with a sampling rate of 2k Hz. Furthermore, all files are imported to MatLab for processing. For each individual case, the zero offset is accounted for by taking the mean offset from the stationary measurements, and subtracting it from the results. Since the measurements includes the two acceleration phases, a cut out is made between the start and end of the data recording files. This allows for a reasonably accurate reading in a steady-state phase with zero acceleration. The average force readings over the most stable area is then extracted by taking the mean force out as an independent variable. These values are used in later calculations to produce relevant data. An example of this is shown in Figure 4.6.

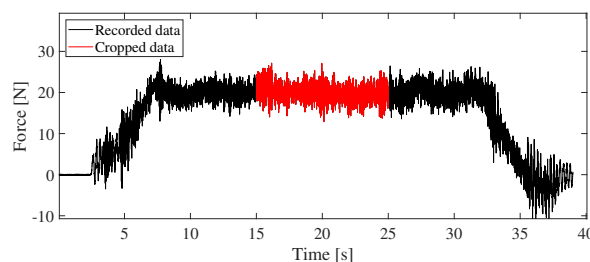


Figure 4.6: Matlab data processing of PT with $V=1\text{m/s}$.

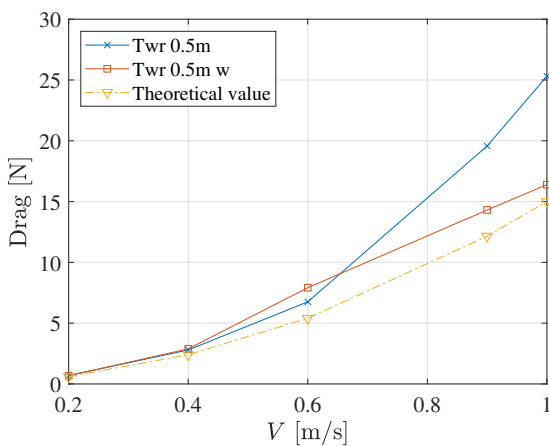
5 Results

This section contains a detailed analysis of the experimental findings. First, a comparison of the drag forces with different carriage velocities is shown. Secondly, the drag coefficients are displayed as a function of the Reynolds number. Lastly, the effects of natural frequency and vortex induced vibrations will be evaluated to assess their impact on the results.

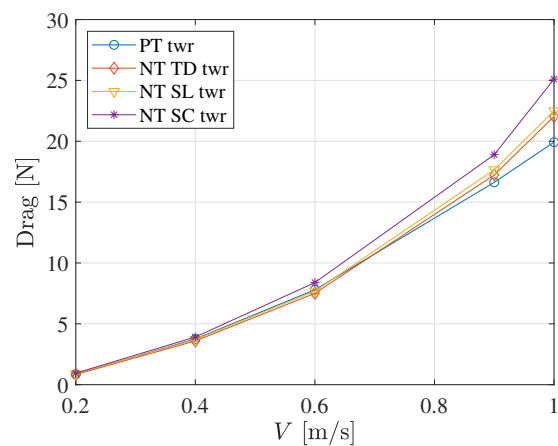
5.1 Drag force comparison

The key objective of the experiments is to verify and compare the drag force of each model configuration. Therefore, a series of towing tests are performed with variable towing velocities ranging from 0.2 m/s to 1 m/s. Four graphs are presented in Figure 5.1, showing two tower tests compared to theoretical values in Figure 5.1a and all turbine setups, including the tower in Figure 5.1b. The graph in Figure 5.1c subtracts the most accurate experimental tower forces from the tower and nacelle measurements - resulting in only the nacelle drag force. In addition, the same is done in Figure 5.1d, but the subtracted, experimental tower data is replaced with theoretical tower drag values.

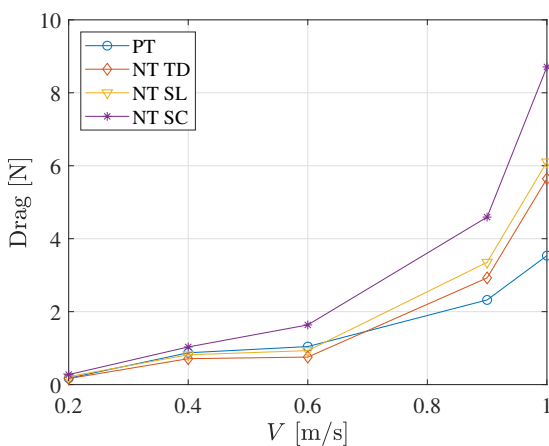
The results demonstrate a distinctive, quadratic increase in drag force relative to the change in velocity. This is to be expected, as seen from the theory in Chapter 2.3. Figure 5.1a suggests that both the weighted and unweighted tower approaches the theoretical values when $V < 0.6$ m/s. However, the tower test without added mass demonstrates a severe deviation from the theoretical values as the velocity increases beyond 0.6 m/s. The unweighted tower delivers a mean drag force of 25.3 N at $V = 1$ m/s, which is very high. For comparison, the weighted tower has a 35% decreased force reading of 16.4 N. In contrast, when $V = 0.6$ m/s, the weighted tower has a drag force of 7.9 N. In this region, the unweighted tower has a 14% decreased reading of 6.75 N. To summarise, the tower with added mass coincides with the theoretical values quite well in the majority of cases, while a higher deviation occurs with the unweighted tower in runs of higher velocity.



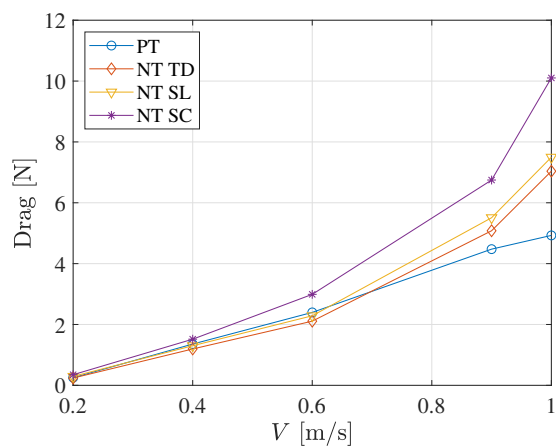
(a) Tower drag force.



(b) Tower and nacelle drag force.



(c) Nacelle drag, experimental values subtracted.



(d) Nacelle drag, theoretical values subtracted.

Figure 5.1: Drag force comparison.

The results from Figure 5.1b reflects the expected outcome in a structured way. The previously developed turbine (PT) with both a small surface and projected area has the lowest drag force in the higher velocity regions. Furthermore, the new turbine with the least streamlined housing (NT SC) delivers the highest drag force as a result. The two streamlined bodies (NT SL/NT SD) have roughly the same drag force, where the difference between the two is within the area of measurement uncertainty. With that said, it makes sense that the setup with the teardrop-shaped back pod has lower drag when compared to theory.

By comparing Figure 5.1c with Figure 5.2d, it is reasonable to assume that the theoretical tower subtraction yields a graph with a more quadratic increase in the slope of the lines. Unexpectedly the PT values are larger than SL and TD in the lower velocity regions, implying that the streamlined options closely match the previous turbine design.

5.2 Drag coefficients

In Figure 5.2, the drag coefficients are displayed as a function of the Reynolds number. The drag coefficients are directly linked to the drag force measurements, meaning a higher drag force equals a greater drag coefficient, given that other parameters such as the reference area and velocity remain unchanged. In all cases, the projected area is used as the reference area.

In Figure 5.2a, the C_D value from the tower tests are evaluated. As a reference, the theoretical value for a vertical cylinder is gathered from Figure 2.3 with a constant value of 1.2. The drag coefficients from the tower tests behaves slightly unpredictable and conflicting when compared to the theoretical values in some areas. In the lower Reynolds number regions, the two tower test coincides with each other, resulting in a C_D of roughly 1.4. In the areas of Reynolds numbers varying from 30.000 to 50.000, the unweighted tower shows a C_D of around 2. This correlates to the unusual high force measurements from Figure 5.1a. On the contrary, the weighted tower gives a C_D value of about 1.4, which is expected considering a slight drag force offset from the theoretical values. The only deviation in measurements for the weighted tower appears with Reynolds number between 20.000 to 30.000 when it approaches a value of 1.8. In conclusion, it is reasonably safe to assume that the tower has a measured drag coefficient somewhere between 1.35 to 1.45.

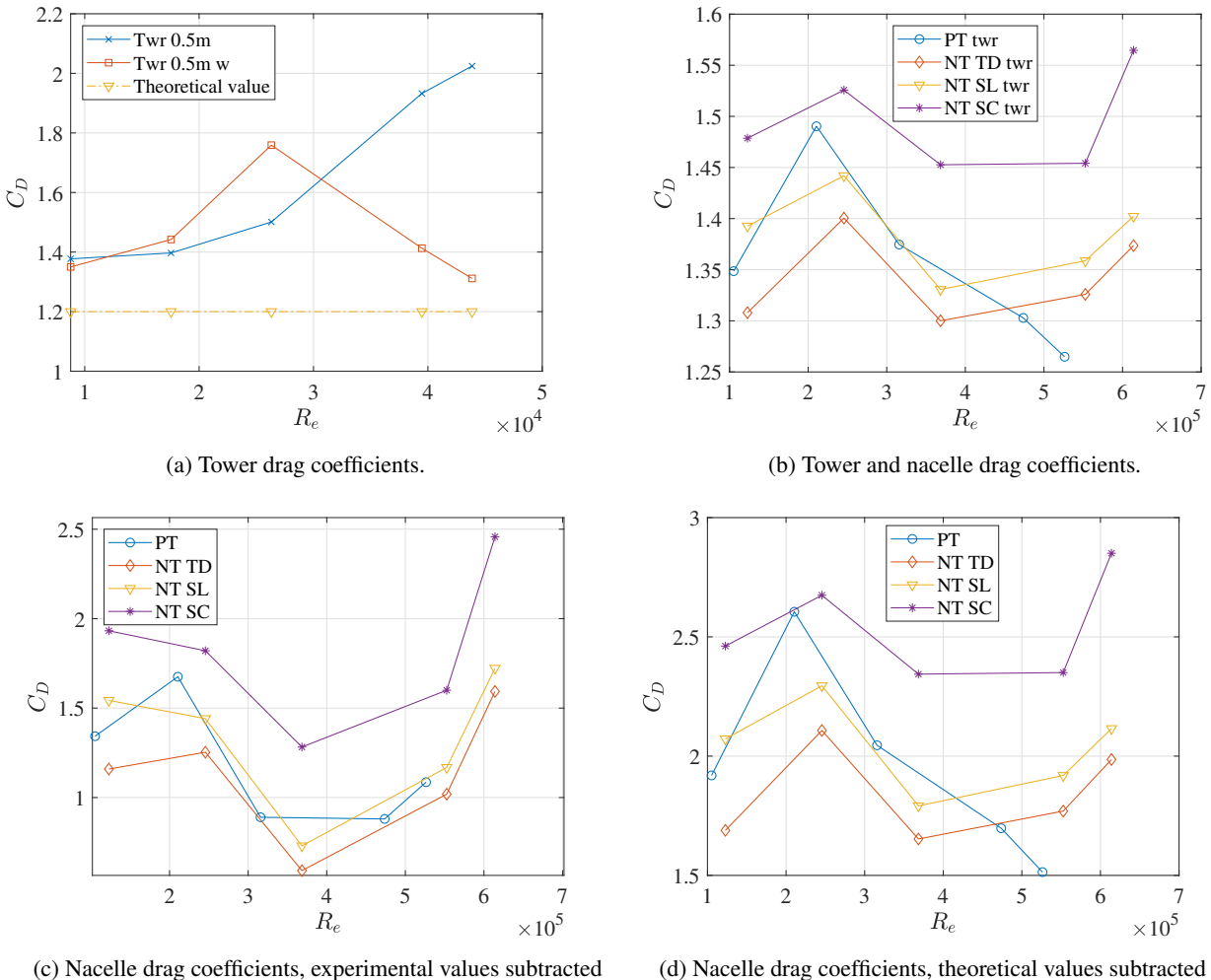


Figure 5.2: Drag coefficient comparison.

Figure 5.2b shows the combined drag coefficients of the tower and nacelle in a typical test configuration. All setups vary to some degree but stay consistent within a maximum C_D variance of 0.25. Adding to this, the previous turbine clearly shows the largest uncertainty with a C_D value ranging from 1.25 to 1.49. Both streamlined nacelles share approximately identical graphs, although with a slight offset. Furthermore, the sharp corners nacelle produces the highest C_D coefficient, as expected from theory. In general, the drag coefficients from Figure 5.2b shows the most reliable and stable results out of all the graphs presented.

In Figure 5.2c, the drag force from the tower is subtracted from the tower and nacelle measurements to estimate the drag coefficient of only the nacelle. The tests in Figure 5.2c shows a clear trend where C_D attains a high value at low and high Reynolds number, but reaches a low point at 400.000. This region is in many cases characterised as a critical region, where some shapes experience fluctuating drag coefficients. The same is likely valid for the nacelle setups as well, hence the variation of the C_D results. Again the outcomes are as expected when comparing the setups in relation to each other. Interestingly, the previous turbine seems to have equally large drag coefficients as the streamlined turbines. This shows that the improved turbine, even though it has a larger drag force, still coincides with the C_D of the previous turbine. As a result, this implies that a streamlined body can compensate for the increased size of the turbine. In Figure 5.2d, the theoretical tower drag is subtracted to form the new partially theoretical drag coefficients of the nacelle. As expected, the C_D value rises due to an increase in the relative nacelle force compared to Figure 5.2c. It is also clear that the form resembles the one in Figure 5.2b. This implies that perhaps the theoretical tower values are more correct to use due to the relative similarities between these two graphs.

5.3 Choice of nacelle

It is not easy to draw a clear conclusion from the experimental results. There are a lot of uncertainties and sources of error to consider, which affect the results in different ways. Regardless of this, a recommendation can be made on the basis of the most reliable results. By inspecting the data recordings, it is clear that the turbine tests with a velocity of 0.6 m/s yield stable graphs in most cases, with little variation across the range. The higher velocity measurements are neglected due to excessive noise in the measurements and a tendency to cause unwanted vibrations. A comparison of the nacelle results is presented in Table 5.4 and the turbine results are shown in Table 5.3.

| Measurements | Turbine type | | | |
|-----------------------------|--------------|-----------|-----------|-----------|
| | PT twr | NT SC twr | NT SL twr | NT TD twr |
| Drag force [N] | 7.8 | 8.4 | 7.7 | 7.5 |
| C_D | 1.37 | 1.45 | 1.33 | 1.3 |
| Drag change from PT twr [%] | - | +7.7 | -1.3 | -3.8 |

Figure 5.3: Comparison of nacelles with tower at $V = 0.6$ m/s.

| Measurements | Nacelle type | | | |
|-------------------------|--------------|-------|-------|-------|
| | PT | NT SC | NT SL | NT TD |
| Drag force [N] | 1.04 | 1.63 | 0.93 | 0.75 |
| C_D | 0.88 | 1.28 | 0.73 | 0.6 |
| Drag change from PT [%] | - | +56.7 | -10.6 | -27.9 |

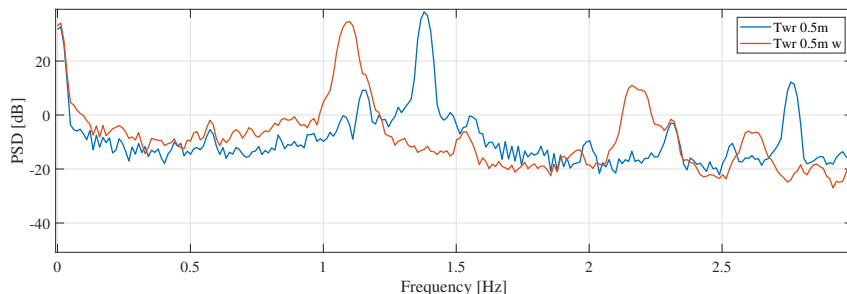
Figure 5.4: Comparison of nacelles at $V = 0.6$ m/s.

In conclusion, the new turbine with a streamlined nacelle and a teardrop shaped back pod results in the lowest force and C_D value. 3D-printing more complex parts does not add to the cost of the project either. All things considered, it is therefore recommended to use the NT TD design to achieve the optimal characteristics of the turbine.

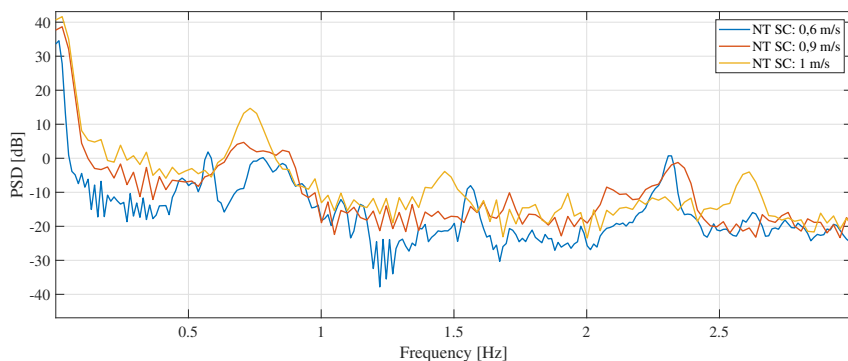
5.4 Power spectral analysis

As mentioned earlier, further processing of the results suggests that the tower may be affected by vortex induced vibrations. As shown in Chapter 2.4, these vibrations vary significantly depending on weight and speed. By using Welch's method in MATLAB, a spectral density estimation is applied to the most relevant sections of force data. Figure 5.5 illustrates the power difference at various frequencies for the tower with and without added mass. The spectral density estimation analyses the power of a signal at different frequencies, which makes it possible to generate a power spectral analysis graph. The force measurements are registered in the relative towing direction, however the VIV-forces are mainly experienced normal to the towing direction, but essentially propagate to all directions.

As seen in Figure 5.5a, it can be noted that peaks from the weighted tower are smaller and shifted towards lower frequencies. It can also be seen that the following peaks are multiples of the first one. One example of this is from the unweighted tower, where its first peak is at 1.4 Hz, and the next is at 2.8 Hz. In Figure 5.5b, three different velocities are illustrated to show the change in power density on the nacelle that was expected to be affected the most by vibrations. From the results, it is observed that the peaks for amplitude and frequency are very similar, but tends to have a higher amplitude at larger velocities.



(a) Tower vibrations at $V = 0.6$ m/s.



(b) SC nacelle at different velocities.

Figure 5.5: Power spectre.

6 Discussion

6.1 Results validation

In order to gather knowledge on the nacelle housing, some simplifications are made. The validity of the results can be regarded as disputable.

Since the nacelle is dependent on a supporting structure i.e the tower to obtain drag force measurements, exclusion of the tower, seen in Figure 5.1c, can lead to some validation issues. In theory, it seems sensible that one part of the turbine can be directly subtracted from related measurements to find the drag force of the nacelle. Nevertheless, all measurements from Figure 5.1c shows that this approach leads to some disagreements with the theoretical estimations. This effect propagates to the drag coefficient in Figure 5.2c as well, because they are outcomes of the same formula.

The inaccuracies imply that the flow pattern of both the tower and nacelle unpredictably affect the drag force measurements. This makes it less correct to subtract only the tower data from the combined tower and nacelle data. One explanation for this, is that some configurations cause higher turbulence downstream of the nacelle. This reduces the flow separation at the connection between the tower and nacelle, which results in a lower hydrodynamic drag for the tower.

Another factor associated with the unexpected drag coefficients is the validity of the reference area used. As mentioned in Section 2.3, the drag force and coefficient depend directly on the size of the body. It is unclear if the projected area yields the most accurate C_D predictions, since neither the length nor surface area are accounted for. Although in theory, it is possible to use any arbitrary surface area on a body as the reference area, since the coefficients will be related by the ratio of the areas [11]. However, this is not tested but would most likely drastically decrease the C_D value.

At last, it is worth mentioning that another approach to data gathering is to perform a CFD analysis on each configuration. This could yield more accurate force readings without additional noise, which may produce more legitimate drag coefficients. Ideally, both numerical and experimental methods should be used to validate each other. Nevertheless, time constraints has lead to the current outcome.

6.2 Effects of VIV on measurements

During the initial stages of testing, a challenging problem was encountered. It was observed, both visually and through data recordings, that some setups at certain velocities resulted in large movements of the turbine tower and nacelle. As shown in Section 2.4, it is common for a cylinder to experience VIV when exposed to a fluid flow normal to its axis orientation. In this section, calculations and observations are discussed to further understand this phenomenon.

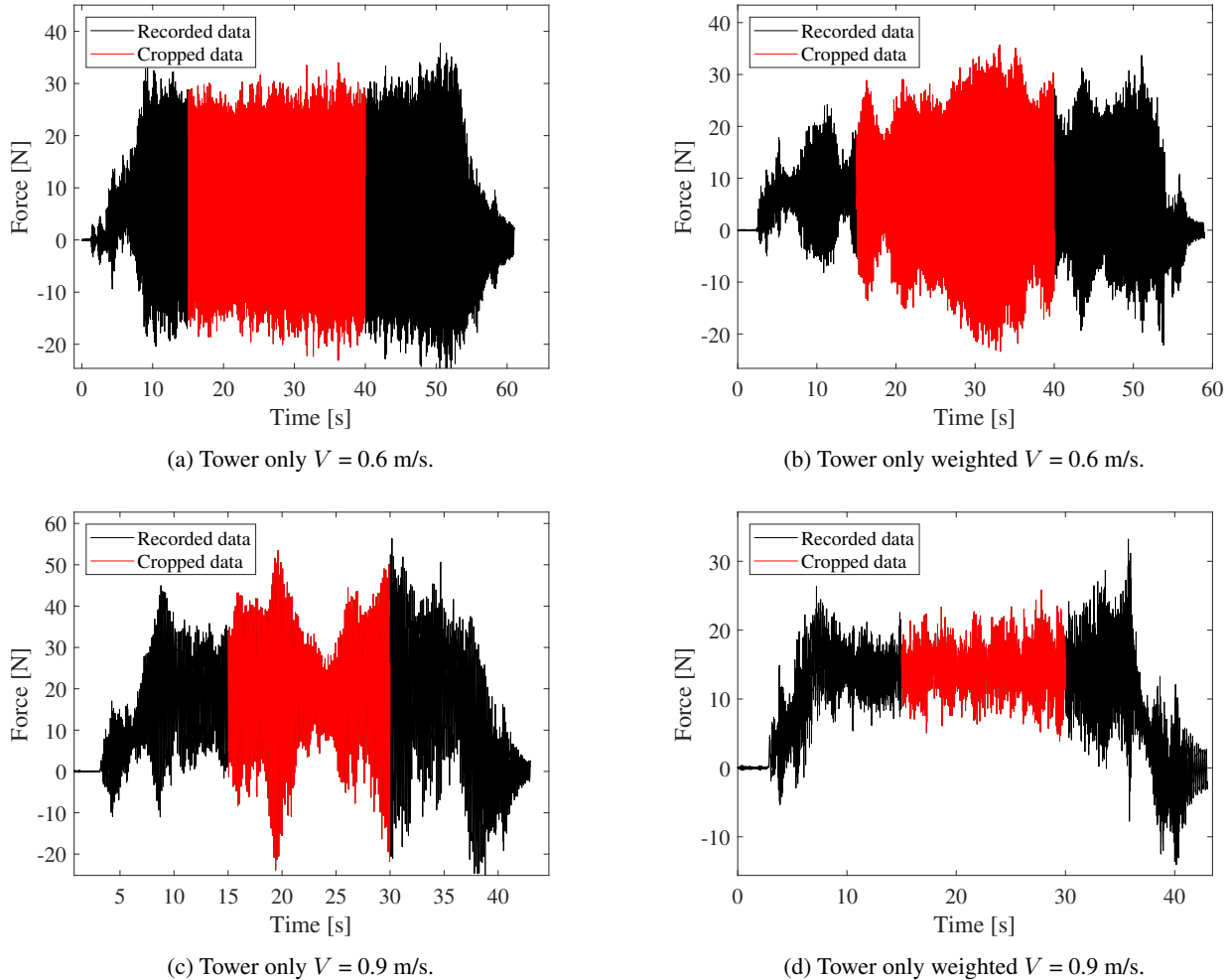


Figure 6.1

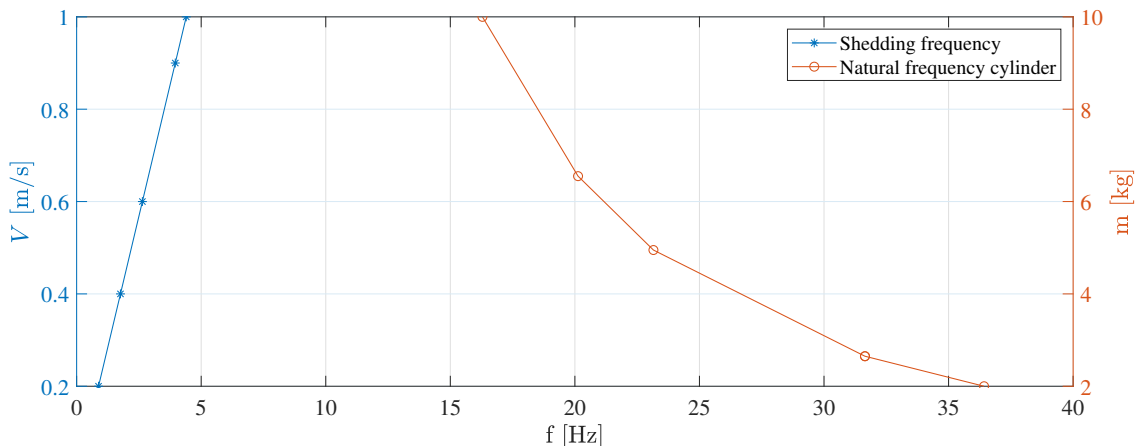
To avoid confusion, only four out of 30 data recordings are presented in Figure 6.1. This is regarded as two of the most relevant examples, showing the tower with and without added mass, resulting in widely different readings. Looking at Figure 6.1a, a nice, even graph with a sensible force reading is shown, disregarding the general noise in the system.

The mean drag force from the cropped area gives a value of 6.75 N. Dissimilarly, a volatile reading with an unpredictable structure is presented in Figure 6.1b, despite having all parameters equal during testing except for the mass. As a result, the mean drag force presents a nearly 20% increased value at 7.9 N. The graph in Figure 6.1c delivers a mean drag force of 19.5 N, which is very high. In comparison, the graph in Figure 6.1d has a 25% decreased force reading of 14.3 N. The experiments have been performed several times for verification and the same tendencies were present each time.

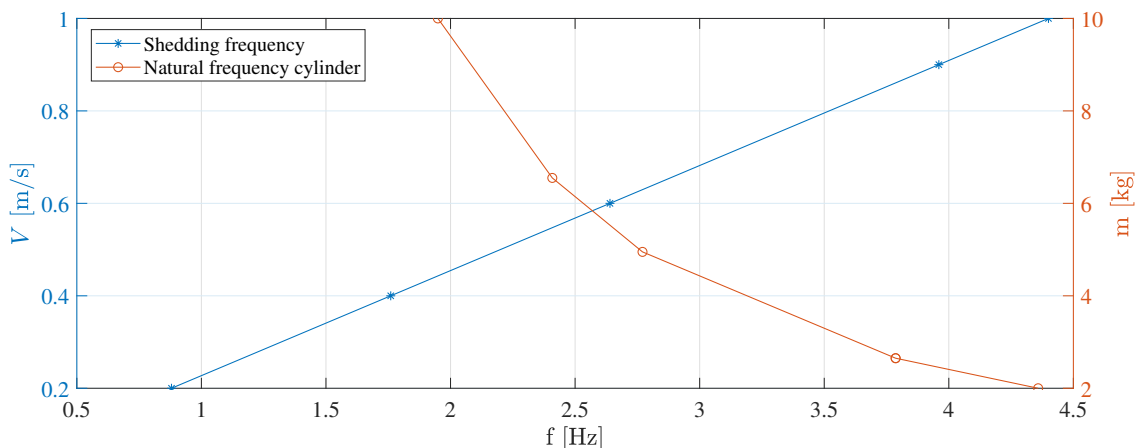
The setup, carriage and measuring instruments are not perfect and do contribute to some level of noise, but they should not be the cause of these behaviours. Consequently, the main suspicion for these results is the effects of VIV on the structure. To reinforce this claim, an analysis has been done involving calculations of the vortex shedding frequency for different flow velocities, and the natural frequency of the tower with changing mass. The results are presented in Figure 6.2. The goal is to uncover potential overlapping frequencies that may cause resonance in the structure, leading to increased force readings at certain speeds.

By studying Figure 6.2a, it is clear that there seemingly is no reason why resonance should occur. The vortex shedding frequency is located in the region of 0.8-4.4 Hz, depending on the flow velocity. Meanwhile, the natural frequency of the cylindrical tower reaches its lowest frequency of 20 Hz with a maximum weight of 3.5 kg added. The key to explaining these situations is perhaps found in Equation (16). It states that the natural frequency is dependent on the spring constant,

k and the mass, m . In an ideal situation, the tower structure would be completely rigidly mounted to the carriage, allowing the spring constant from the tower to be used. In reality, this is not the case since the load cell housing with flexible shims needs to be accounted for. For that reason, the spring constant might actually be a lot smaller than thought.



(a) Resonance analysis with calculated spring constant, $k = 104750$ N/m.



(b) Resonance analysis with estimated spring constant, $k = 1500$ N/m.

Figure 6.2

Due to the complexity of the test setup, it is difficult to calculate the exact input parameters to find the natural frequency domain. One way to estimate the spring constant and natural frequency is by changing k until the graph correlates to the observations and the data recordings.

The method of changing the spring constant is used in Figure 6.2. In this case, the spring constant is reduced from 104750 N/m in Figure 6.2a to 1500 N/m in Figure 6.2b. By comparing the drag force measurements and the data recordings, it seems to be a quite good approximation. When the tower is unweighted, it has overlapping frequencies in the upper-velocity regions around 0.9 and 1 m/s. The weighted tower takes care of this by lowering the natural frequency. As a result, the new overlapping frequencies are moved to the region around 0.6 m/s. According to observations and data recordings in Appendix A, this could be the best explanation for the behaviour of the drag force measurements, especially the tower tests.

Another way to estimate the spring constant and natural frequency is to perform a decay test of the structure, and find the periodic oscillations of either force or displacement measurements. The third method is to use the actual towing test files, and extract the same information by finding the dominating peaks in the force readings through a power spectral analysis. A power spectral analysis was previously shown in Section 5.4. The graphs clearly show that an increase in mass results in the amplitude peak being shifted to a lower frequency. In the case of tower only at 0.6 m/s, it went from 1.38 Hz to 1.10 Hz when the extra mass was added. An increase in velocity did not shift the peak frequency. It is as expected since mass is part of the Equation (16) and velocity is not. Interpreting the power spectre graph at higher frequencies does not give any good values as a result of the previous frequencies being added together and mostly result in static.

It is clear that a relatively complicated topic has many explanations. No matter the cause, it is clear that resonance has an effect on the results and further knowledge should help to avoid the occurrence in later testing.

7 Conclusion

The initial design phase gave several design iterations resulting in an optimised turbine for experimental use. New solutions have been developed with inspiration from previous work and similar projects. The new design aims to be highly reliable, while meeting the design requirements such as water tightness, low drag resistance and ease of maintainability. Rapid prototyping with 3D-printing made it possible to closely inspect all components, and to work as a reference guide for the lab engineers in the manufacturing process. Due to time constraints, the production of the final product was not completed, however a complete assembly manual with detailed descriptions is produced to aid in the production at a later stage.

Following this, four different turbine configurations are tested in MarinLab at HVL, to validate the drag force effects on different nacelle shapes. Rapid prototyping with 3D-printing is used to generate both streamlined and non-streamlined shapes. During the initial test phase, a noticeable sideways swaying was observed on both the tower and nacelle. There is reason to believe that the frequency of vortex shedding could resonate with the tower's natural frequency. Specifically at higher towing speeds, it was observed that changing the tower mass influenced the natural frequency, and measurement results significantly. As a result, a power spectral analysis is used to determine at which frequencies these deviations occur.

The experiments indicates that a streamlined nacelle has a clear advantage compared to a non-streamlined nacelle as expected. The drag- force and coefficients of the streamlined nacelle has significantly lower values across the test range. However, when compared to the previous turbine it is difficult to draw a conclusion due to measurement uncertainty. Still there are strong indications that the new streamlined nacelle can outperform the previous nacelle in relation to its hydrodynamic characteristics. The likelihood of a reduced drag force also contributes to less irregularities in the wake behind the turbine - which could give a positive effect on further experimental testing. The outcome shows that even though the new solutions has led to a larger nacelle, a streamlined shape can compensate for the losses.

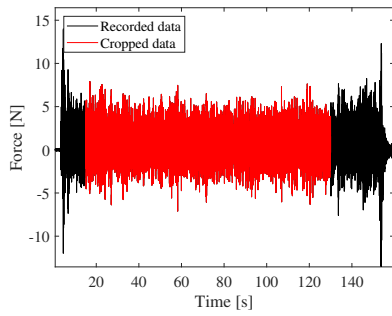
References

- [1] WindEurope. “Europe wants more renewables to increase its energy security”. <https://windeurope.org/newsroom/press-releases/europe-wants-more-renewables-to-increase-its-energy-security/>, 2022. [Online; accessed Mar. 17, 2022].
- [2] A. I. Winter. “Differences in fundamental design drivers for wind and tidal turbines”. In *OCEANS 2011 IEEE - Spain*, pages 1–10, 2011. doi:10.1109/Oceans-Spain.2011.6003647.
- [3] T.Stallard G.S. Payne and R.Martinez. “Design and manufacture of a bed supported tidal turbine model for blade and shaft load measurement in turbulent flow and waves”, July 2017. doi:10.1016/j.renene.2017.01.068.
- [4] Nova Innovation. “Scottish energy innovators win €2.5M to turn up the tempo of tidal power”. <https://windeurope.org/newsroom/press-releases/europe-wants-more-renewables-to-increase-its-energy-security/>, 2021. [Online; accessed Mar. 20, 2022].
- [5] Wind Catching Systems. “Unleashing the power of offshore wind”. <https://windcatching.com/>. [Online; accessed May. 16, 2022].
- [6] Christian Masson and Arezki Smaïli. “Numerical study of turbulent flow around a wind turbine nacelle”. *Wind Energy*, 9(3):281–298, 2006. doi:https://doi.org/10.1002/we.171.
- [7] Subrata Kumar Chakrabarti. *Offshore Structure Modeling*, February 1994.
- [8] Yunus A. Çengel and John M. Cimbala. *Fluid mechanics: Fundamentals and applications*, 2006.
- [9] J.N. Sørensen. “Actuator disc”. *Supervised Machine Learning in Wind Forecasting and Ramp Event Prediction, 2020*, 2012. <https://www.sciencedirect.com/topics/engineering/actuator-disc> [Online; accessed May. 25, 2022].
- [10] Rupp Carriveau. *Advances in Wind Power*. IntechOpen, Rijeka, 2012. doi: 10.5772/3376.
- [11] Tom Benson. “The Drag Equation”. <https://www.grc.nasa.gov/www/k-12/rocket/drageq.html>. [Online; accessed May. 13, 2022].
- [12] Nuclear-power.com. “Skin friction – Friction Drag”. <https://www.nuclear-power.com/nuclear-engineering/fluid-dynamics/what-is-drag-air-and-fluid-resistance/skin-friction-friction-drag/>, 2012. [Online; accessed Apr. 29, 2022].
- [13] Ehab Banihani and Mamdouh El Haj Assad. “Boundary-layer theory of fluid flow past a flat-plate: Numerical solution using matlab”. *International Journal of Computer Applications*, 180, 02 2018. doi: 10.5120/ijca2018916374.
- [14] Rony Caballero, Adan Vega, Aranzazu Berbey-Alvarez, and Manuel Armada. “Six degree of freedom underwater vehicle for culvert inspection”. https://www.researchgate.net/publication/264557763_SIX_DEGREE_OF_FREEDOM_UNDERWATER_VEHICLE_FOR_CULVERT_INSPECTION, July 2014. [Online; accessed Mar. 23, 2022].
- [15] S.F Hoerner. *Fluid-dynamic drag: practical information on aerodynamic drag and hydrodynamic resistance.*, 1958.
- [16] Scott Jeff. “Drag of cylinders & cones”. <http://www.aerospaceweb.org/question/aerodynamics/q0231.shtml>, 2005. [Online; accessed Apr. 29, 2022].
- [17] Mingwei Ge, De Tian, and Ying Deng. “Reynolds number effect on the optimization of a wind turbine blade for maximum aerodynamic efficiency”, Sep. 2014. doi: 10.1061/(ASCE)EY.1943-7897.0000254.
- [18] Vestas Wind Systems A/S. “Performance specification v117-4.0/4.2 mw 50/60 hz”. http://www.ambiente.chubut.gov.ar/wp-content/uploads/2018/04/Anexo-4-0067-7063_V01-Performance-Specification-V117-4.0_4.2MW-Strong-Wind.pdf, July 2017. [Online; accessed Mar. 30, 2022].
- [19] Atlantis resources. “AR1500 Tidal Turbine”. <https://simecatlantis.com/wp-content/uploads/2016/08/AR1500-Brochure-Final-1.pdf>, June 2016. [Online; accessed Mar. 30, 2022].

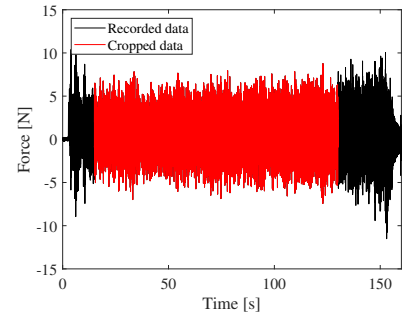
- [20] R. D. Gabbai and H. Benaroya. “An overview of modeling and experiments of vortex-induced vibration of circular cylinders”, April 2005. doi: 10.1016/j.jsv.2004.04.017.
- [21] W. U. A. Leong, I. H. Savci, A. Hatton, and J. Scott. “Using 3D CFD to model exhaust fuel dosing device (fuel vaporizer) and oxidation of hydrocarbon”, January 2011. doi: 10.1533/9780857095060.6.245.
- [22] J. F. Sigrist A. Placzek and A. Hamdouni. “Numerical simulation of an oscillating cylinder in a cross-flow at low Reynold number: Forced and free oscillations”. *Computers & Fluids*, 38(1):80–100, 2009. doi: 10.1016/j.compfluid.2008.01.007.
- [23] Wikipedia, the free encyclopedia. “Deflection”. <https://upload.wikimedia.org/wikipedia/commons/thumb/7/7f/Deflection.svg/1280px-Deflection.svg.png>. [Online; accessed April 27, 2022].
- [24] Mark W. Monaghan and Robert J. Henry. “Development of Hybrid Product Breakdown Structure for NASA Ground Systems”, September 2013. doi: 10.2514/6.2013-5404.
- [25] Maritime Research Institute Netherlands | MARIN. <https://www.marin.nl/>. [Online; accessed Mar. 29, 2022].
- [26] Online shop for high precise drive systems by maxon | maxon group. <https://www.maxongroup.com/maxon/view/product/motor/ecmotor/EC-i/516068>. [Online; accessed Mar. 30, 2022].
- [27] David G. Callister, William D. Rethwisch. *Materials Science and engineering 10th edition*, September 2019.
- [28] J. A. Charles, F. A. A. Crane, and J.A.G Furness. *Selection & Use of Engineering Materials*, 1994.
- [29] Ceetak | O-ring calculator | Axial face. <https://ceetak.com/o-ring-calculator>. [Online; accessed 2022-05-03].
- [30] 6X22X7 HMSA10 RG - Radial shaft seals for general industrial applications | SKF. <https://www.skf.com/id/products/industrial-seals/power-transmission-seals/radial-shaft-seals/productid-6X22X7%20HMSA10%20RG>. [Online; accessed Apr. 03, 2022].
- [31] Oil Seals | Radial Oil Seals | Trelleborg. <http://www.trelleborg.com/en/seals/products-and-solutions/oil-seals>. [Online; accessed Apr. 03, 2022].
- [32] Leslie A. Horve. “Understanding The Sealing Mechanism Of The Radial Lip Seal For Rotating Shafts”, 1992. doi: 10.1007/978-94-011-2412-6_2.
- [33] T. B. Sercombe. “Laser sintering and rapid prototyping of aluminium”, January 2011. doi: 10.1533/9780857090256.3.702.
- [34] Michal Šašala, Lukáš Hrivniak, and Jozef Svetlik. “Material selection for prototype design and production”, 2020. [Online]. Available: https://www.researchgate.net/publication/341676753_Material_Selection_for_Prototype_Design_and_Production.
- [35] A. Velling. “Limits fits”. <https://fractory.com/limits-and-fits/> [Online; accessed Mar. 22, 2022].
- [36] SKF Bearing Select. <https://www.skfbearingselect.com/#/fits/single-bearing> [Online; accessed May. 21, 2022].
- [37] ISO System of Limits and Fits (Tolerances). <http://www.pfeffer.ch/isotolerances.htm> [Online; accessed May. 15, 2022].
- [38] International Towing Tank Conference. *Guideline for VIV Testing*, 2011. <https://www.ittc.info/media/8131/75-02-07-0310.pdf>.

Appendix

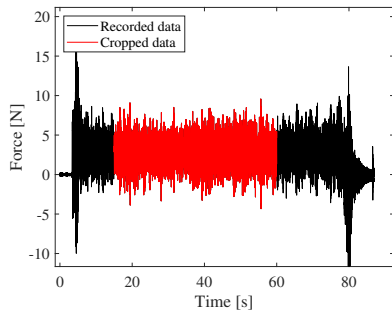
Appendix A: Data recordings



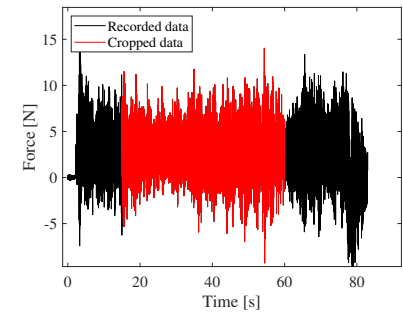
(a) Tower only $V = 0.2$ m/s



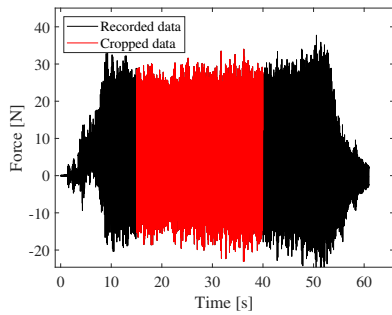
(b) Tower only weighted $V = 0.2$ m/s



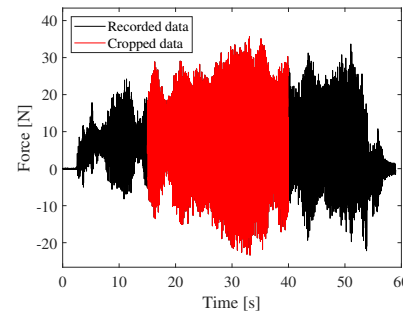
(c) Tower only $V = 0.4$ m/s



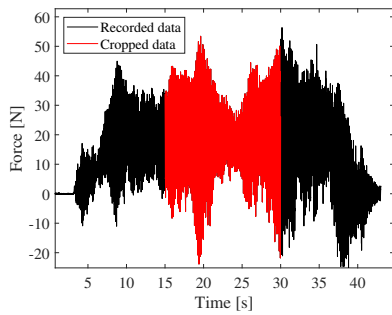
(d) Tower only weighted $V = 0.4$ m/s



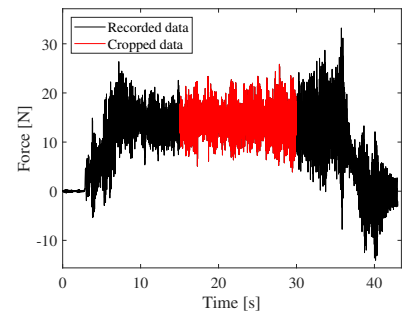
(e) Tower only $V = 0.6$ m/s



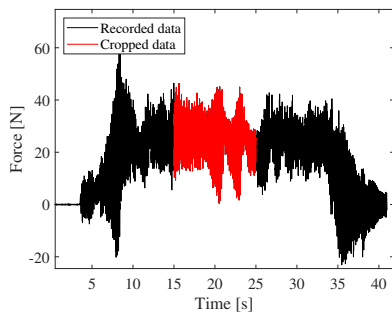
(f) Tower only weighted $V = 0.6$ m/s



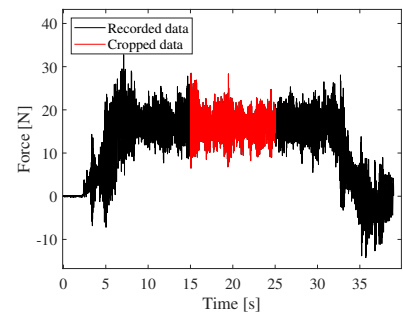
(g) Tower only $V = 0.9$ m/s



(h) Tower only weighted $V = 0.9$ m/s

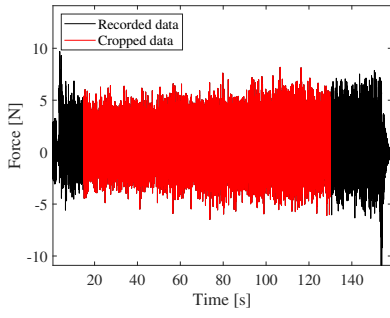


(i) Tower only $V = 1$ m/s

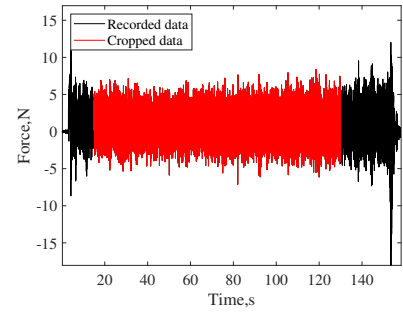


(j) Tower only weighted $V = 1$ m/s

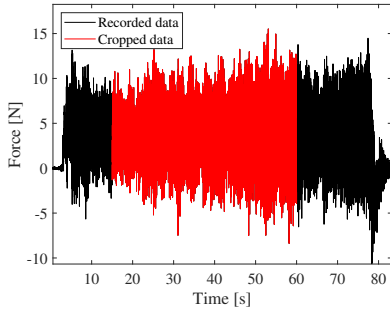
Figure .1: Data Recordings Towers



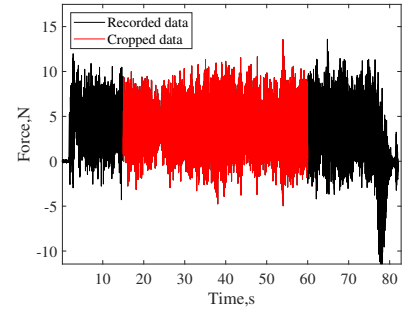
(a) PT $V = 0.2$ m/s



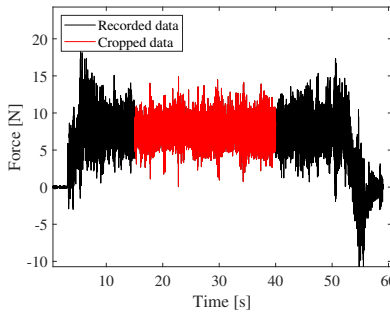
(b) NT SC $V = 0.2$ m/s



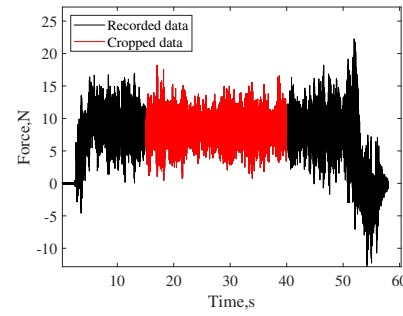
(c) PT $V = 0.4$ m/s



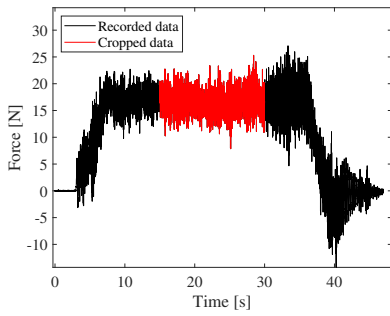
(d) NT SC $V = 0.4$ m/s



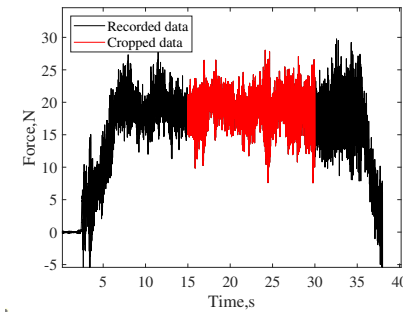
(e) PT $V = 0.6$ m/s



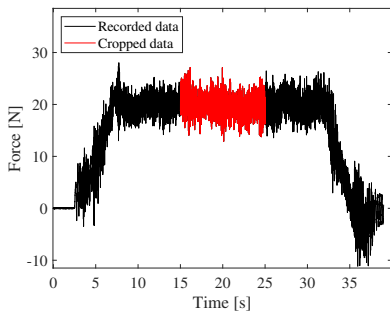
(f) NT SC $V = 0.6$ m/s



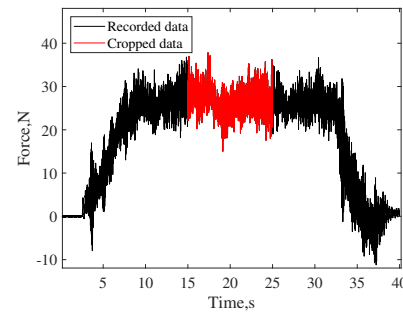
(g) PT $V = 0.9$ m/s



(h) NT SC $V = 0.9$ m/s

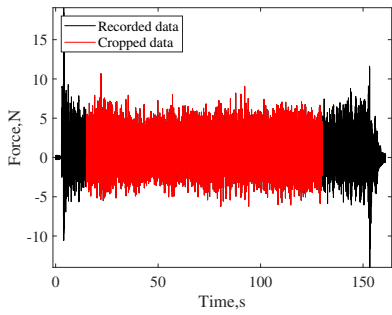


(i) PT $V = 1$ m/s

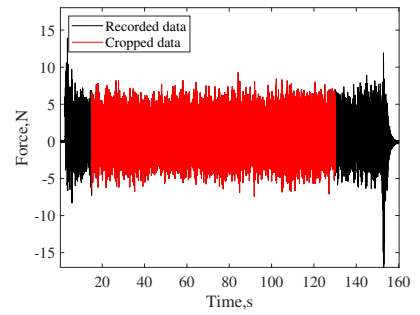


(j) NT SC $V = 1$ m/s

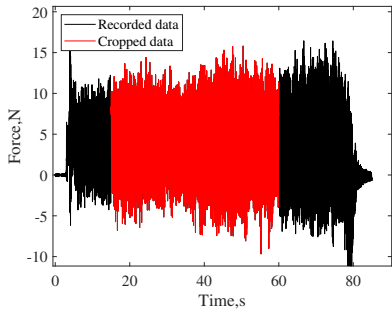
Figure .2: Data Recordings Turbines 1



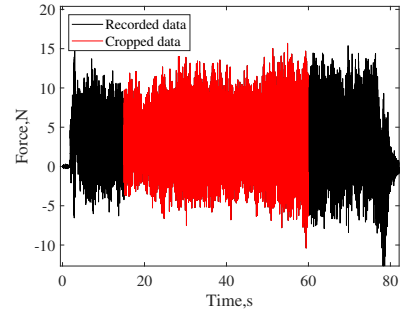
(a) NT SL $V = 0.2 \text{ m/s}$



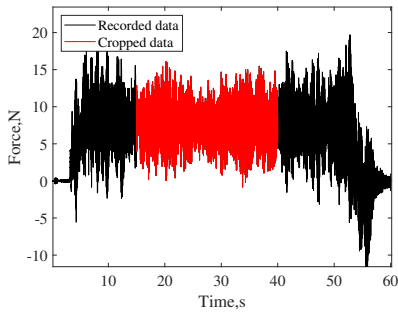
(b) NT TD $V = 0.2 \text{ m/s}$



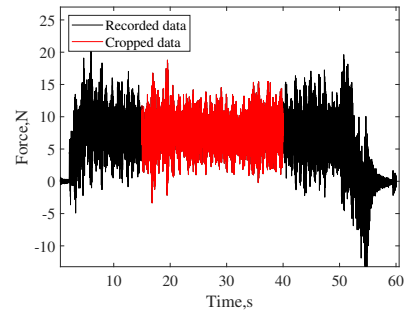
(c) NT SL $V = 0.4 \text{ m/s}$



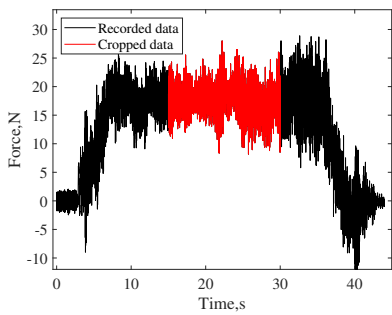
(d) NT TD $V = 0.4 \text{ m/s}$



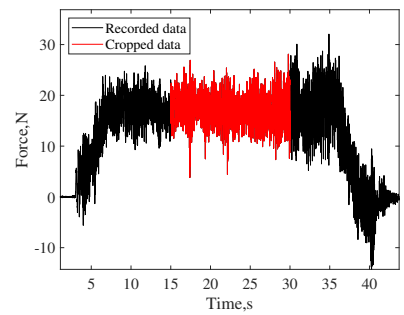
(e) NT SL $V = 0.6 \text{ m/s}$



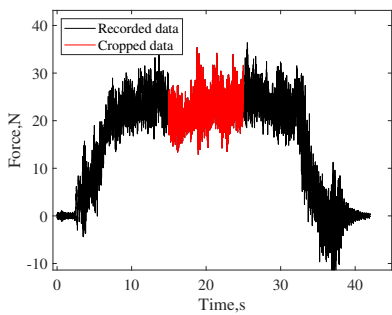
(f) NT TD $V = 0.6 \text{ m/s}$



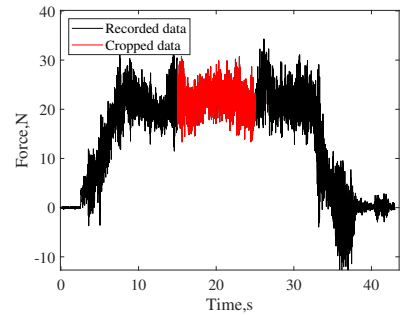
(g) NT SL $V = 0.9 \text{ m/s}$



(h) NT TD $V = 0.9 \text{ m/s}$



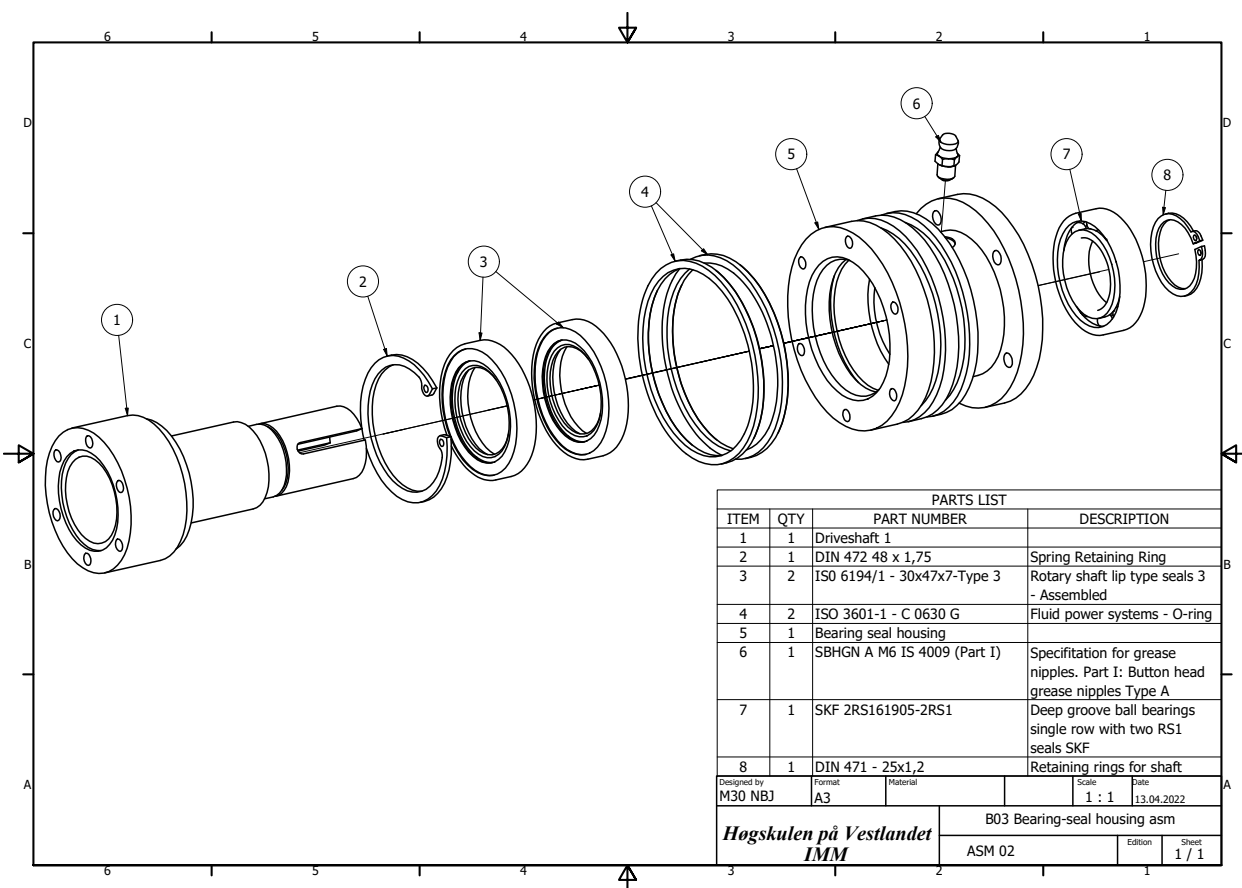
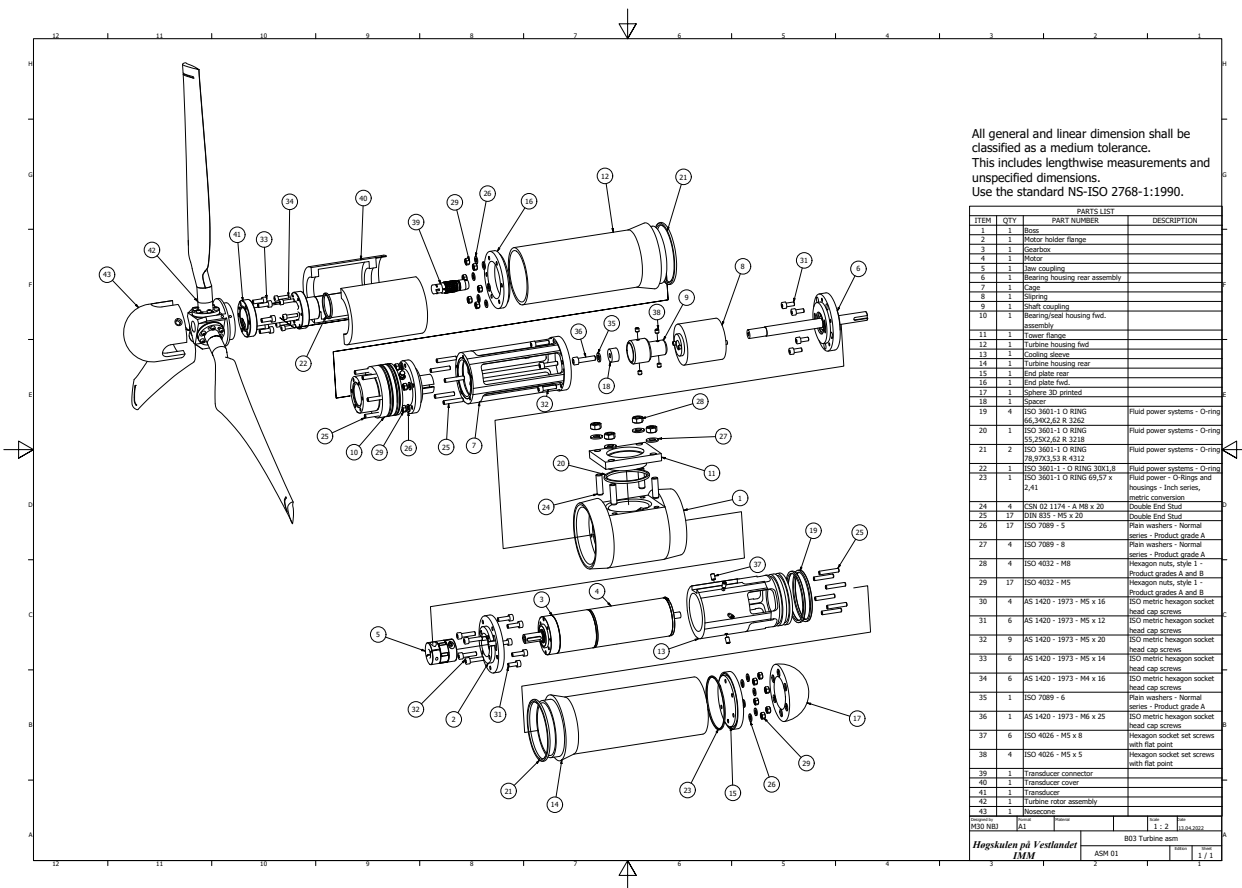
(i) NT SL $V = 1 \text{ m/s}$

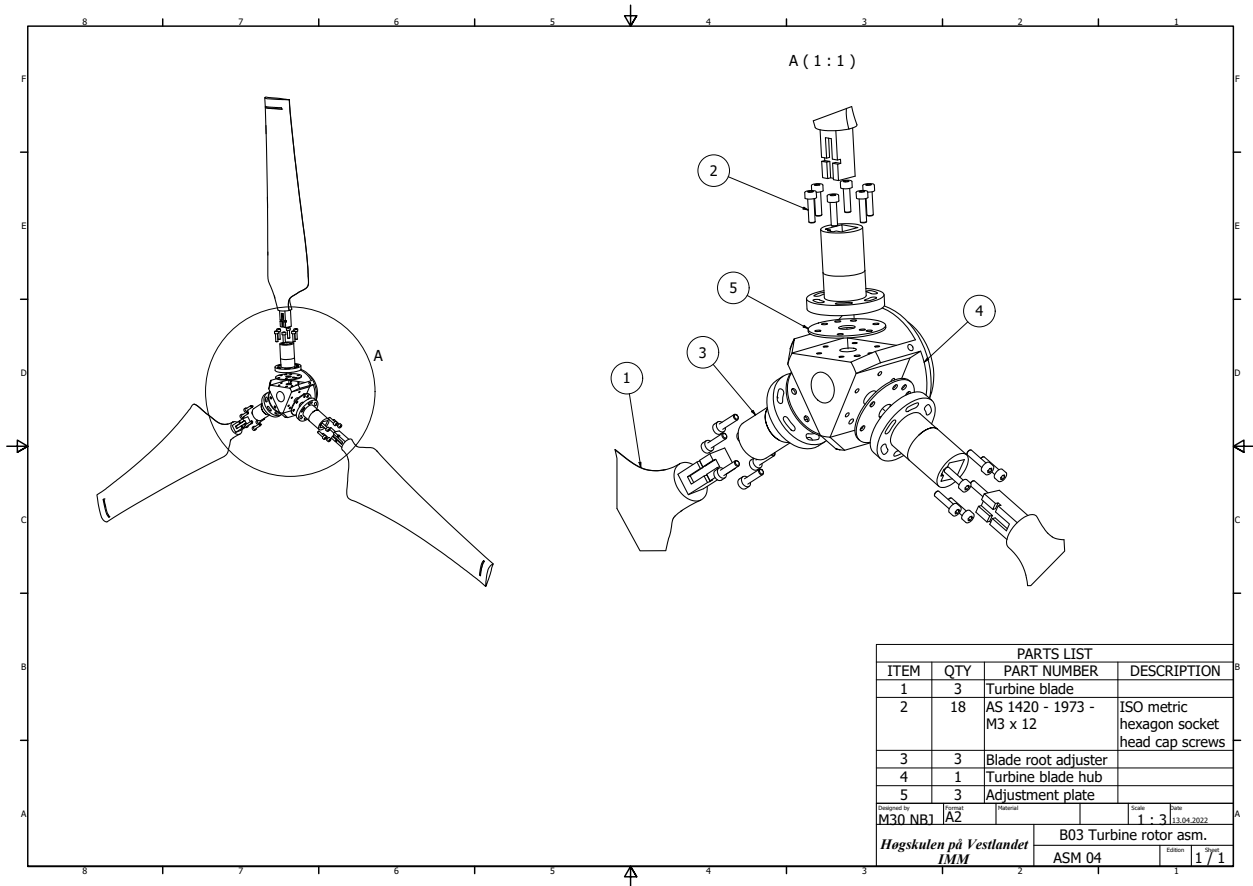
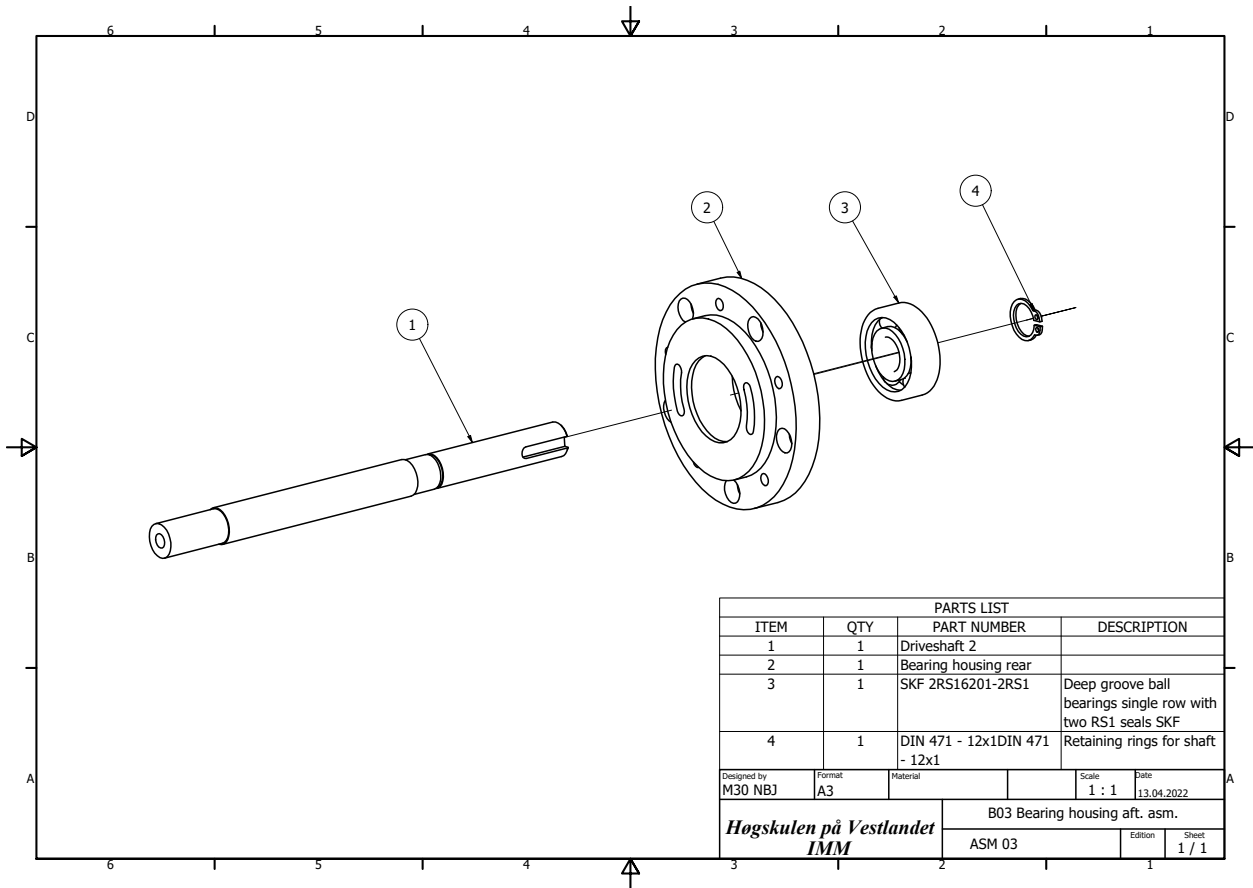


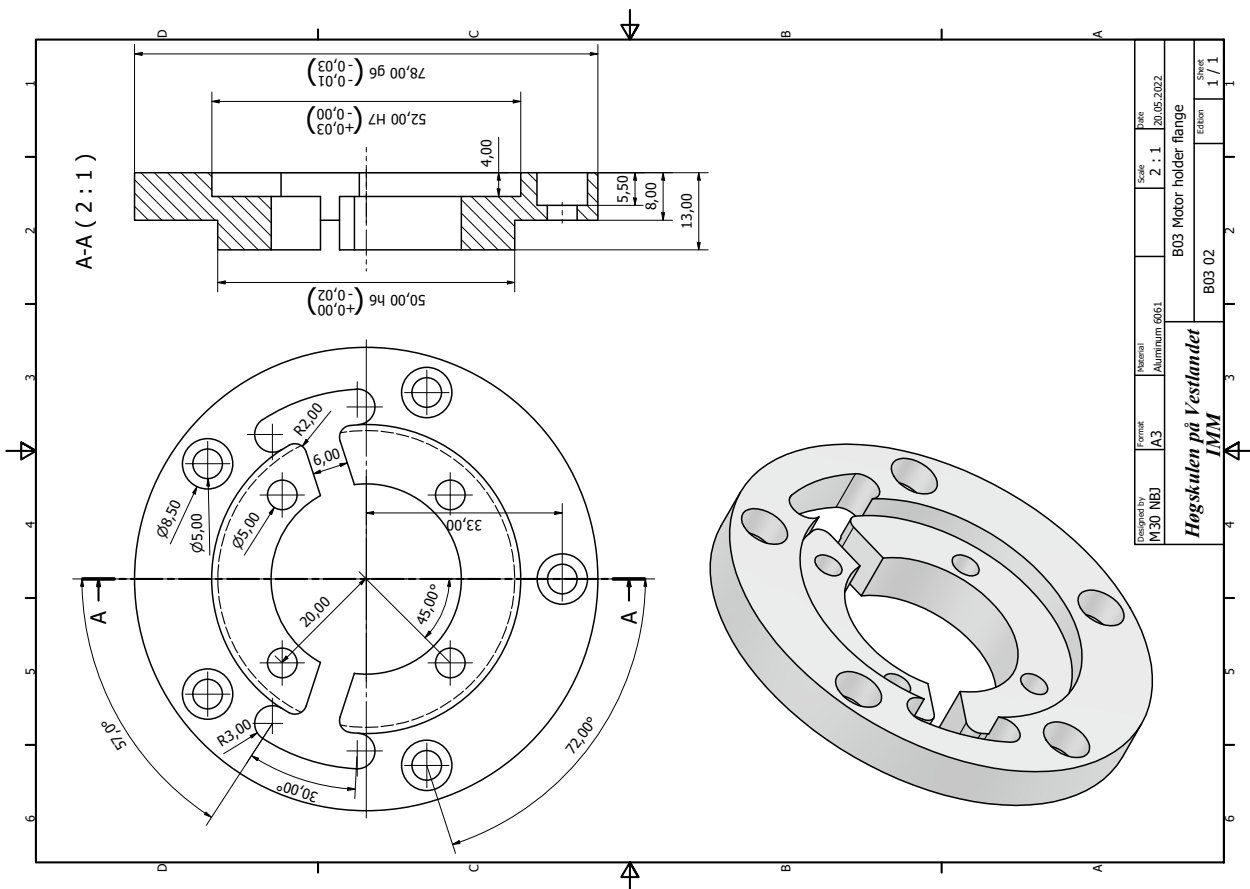
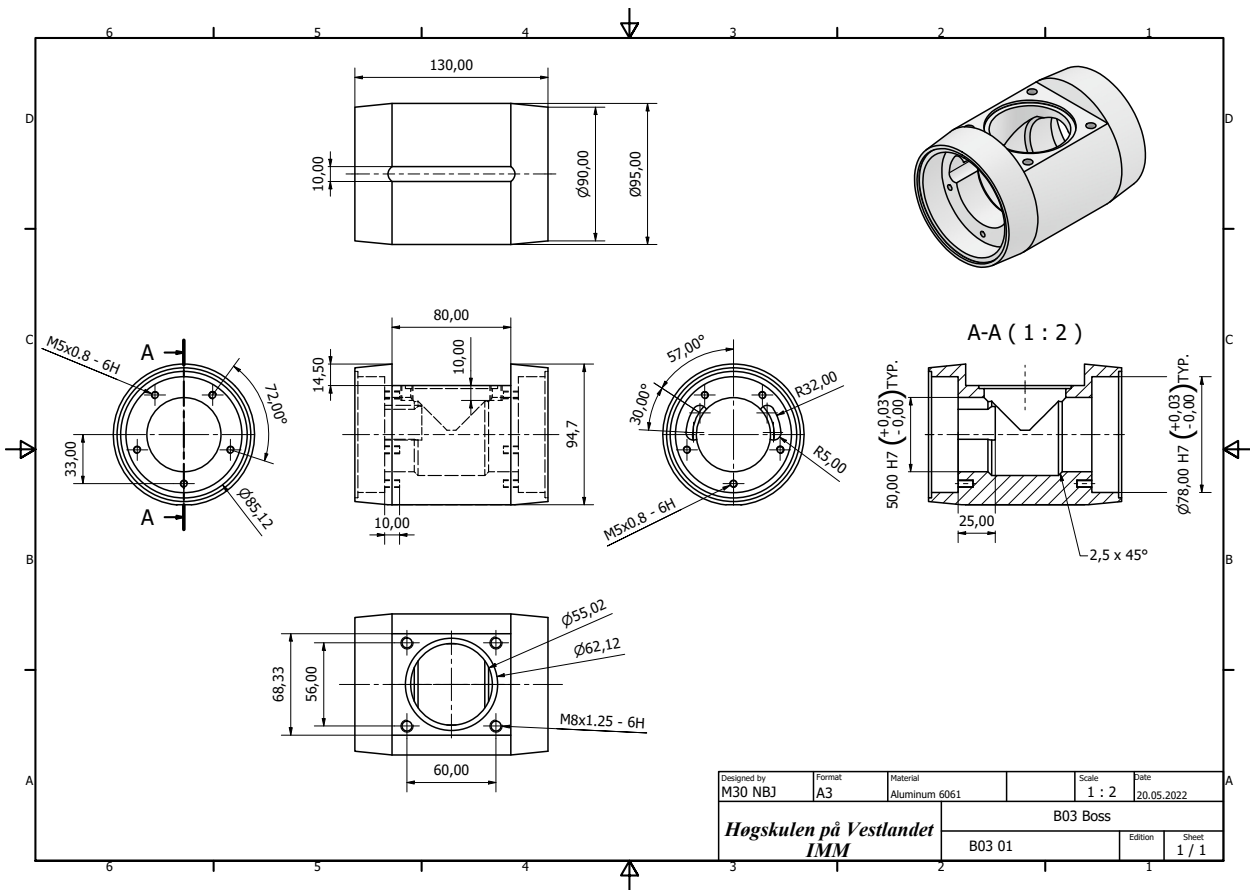
(j) NT TD $V = 1 \text{ m/s}$

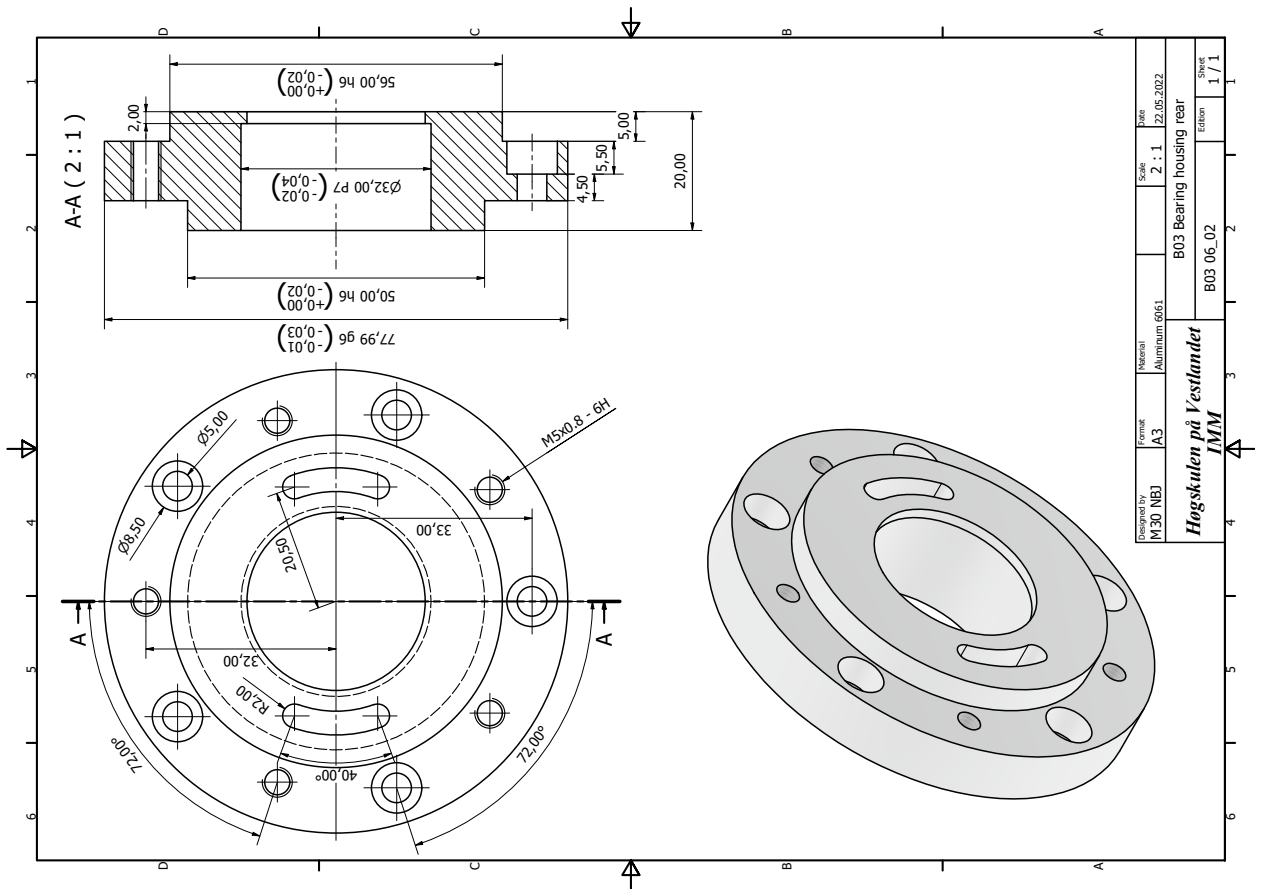
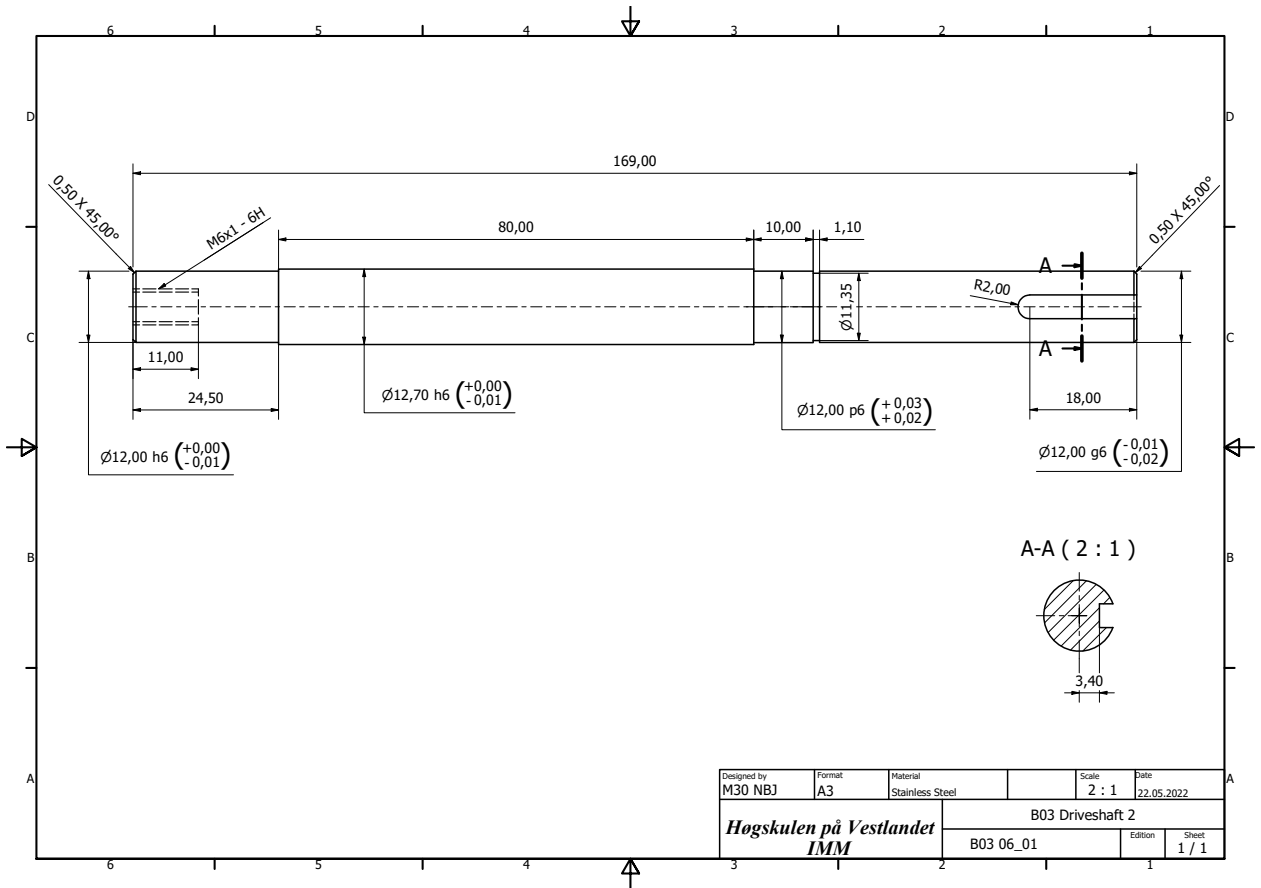
Figure .3: Data Recordings Turbines 2

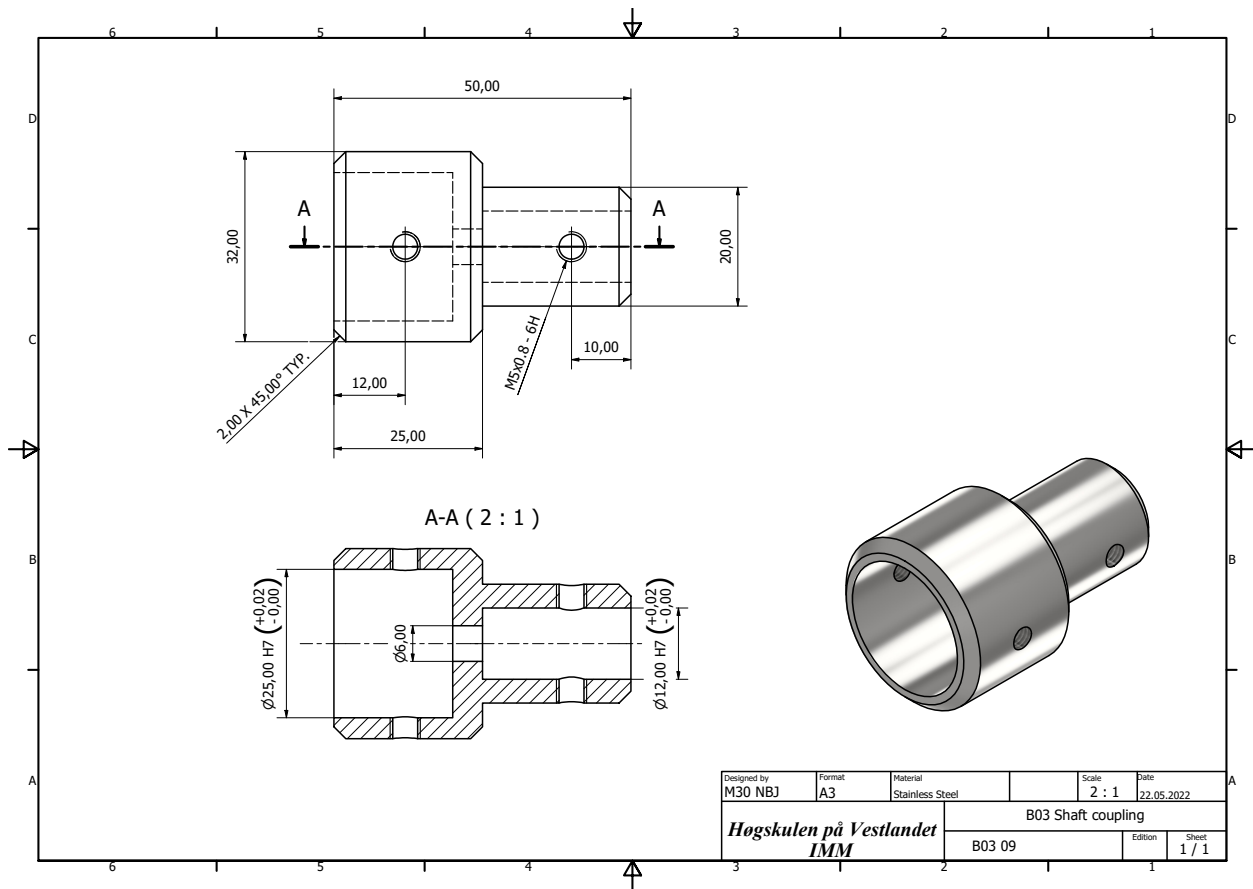
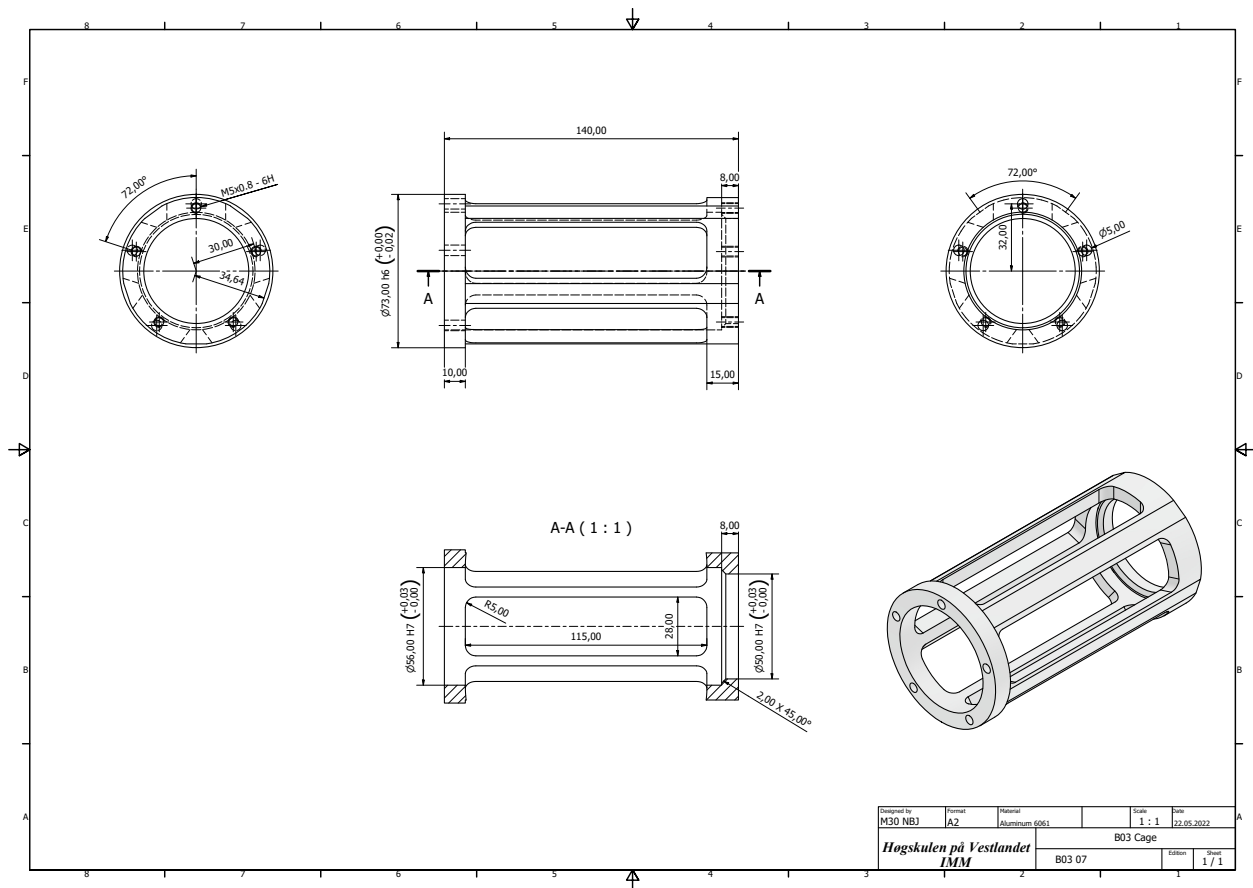
Appendix B: CAD drawings

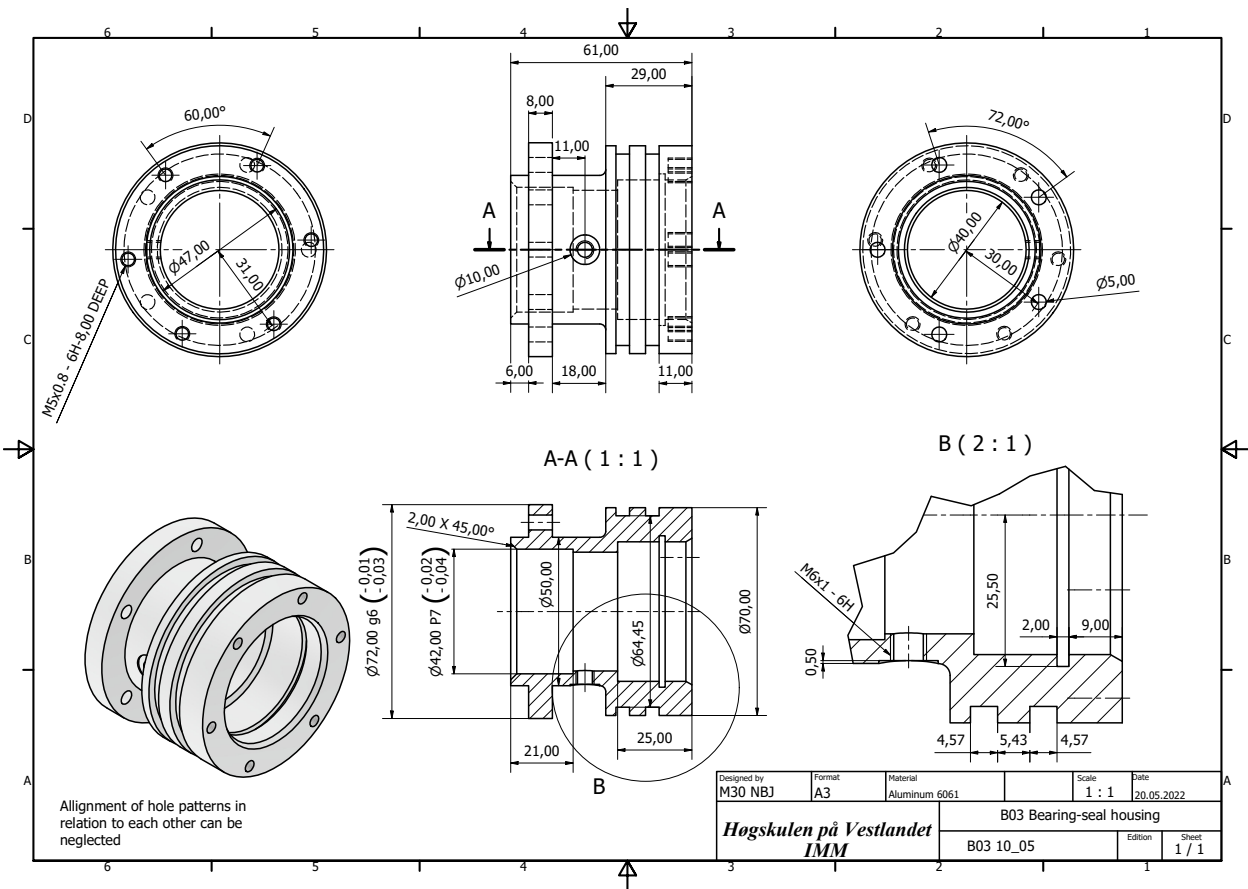
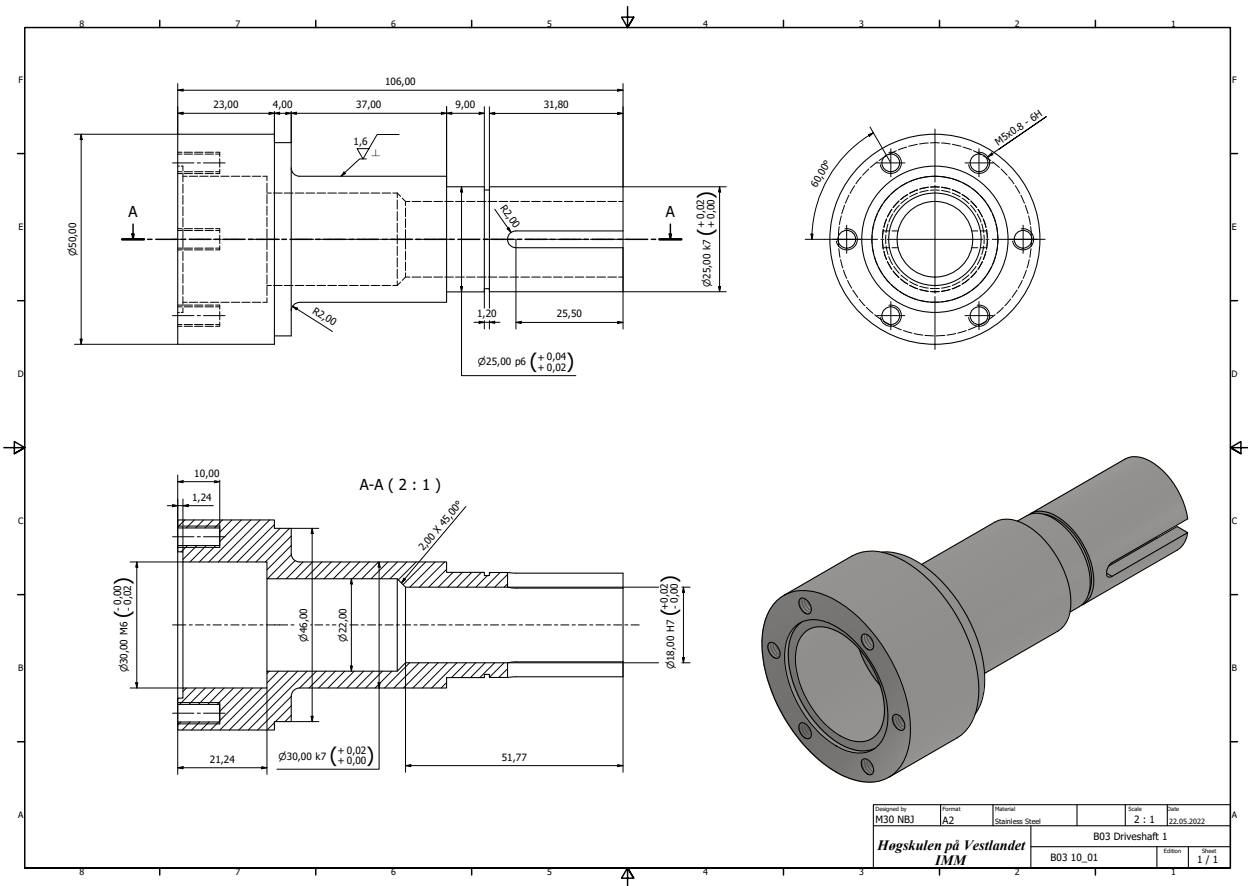


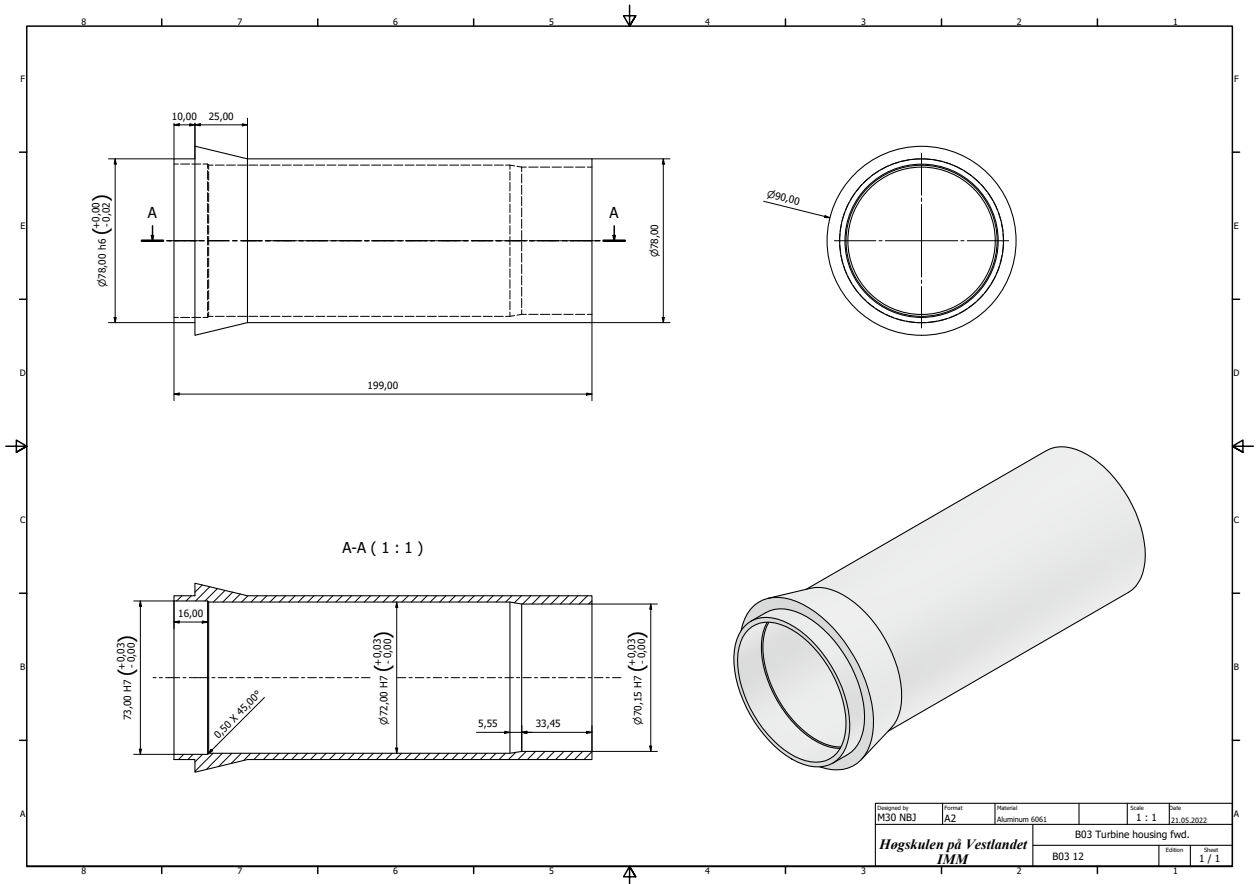
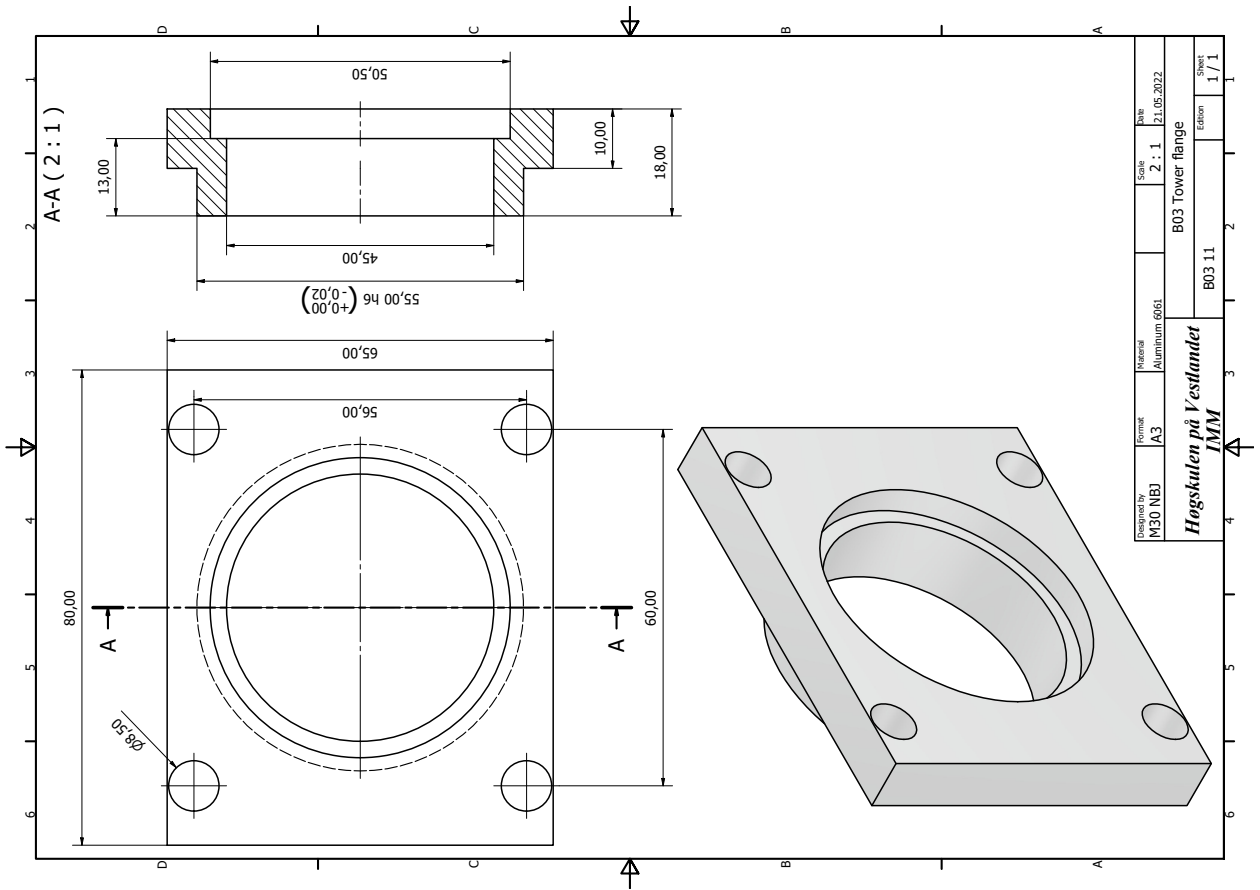


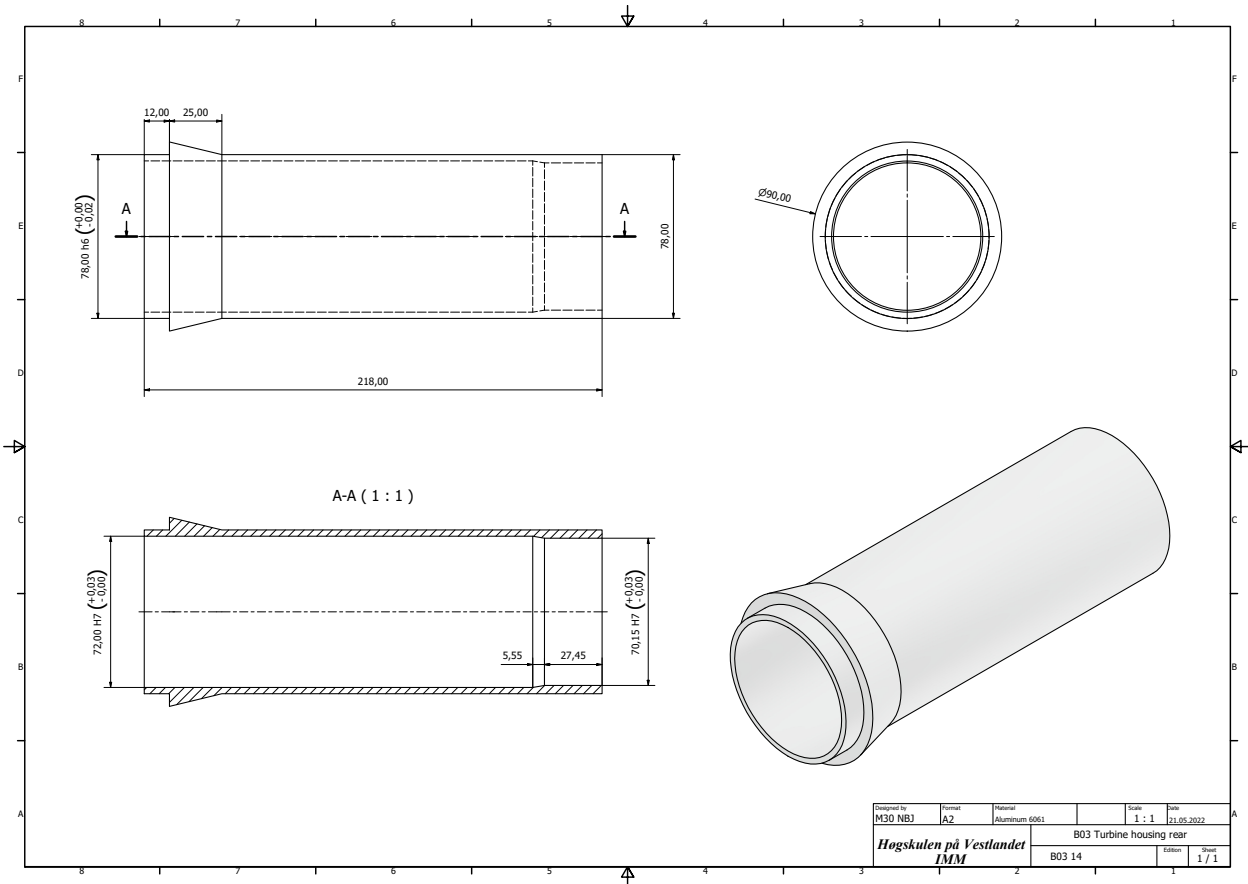
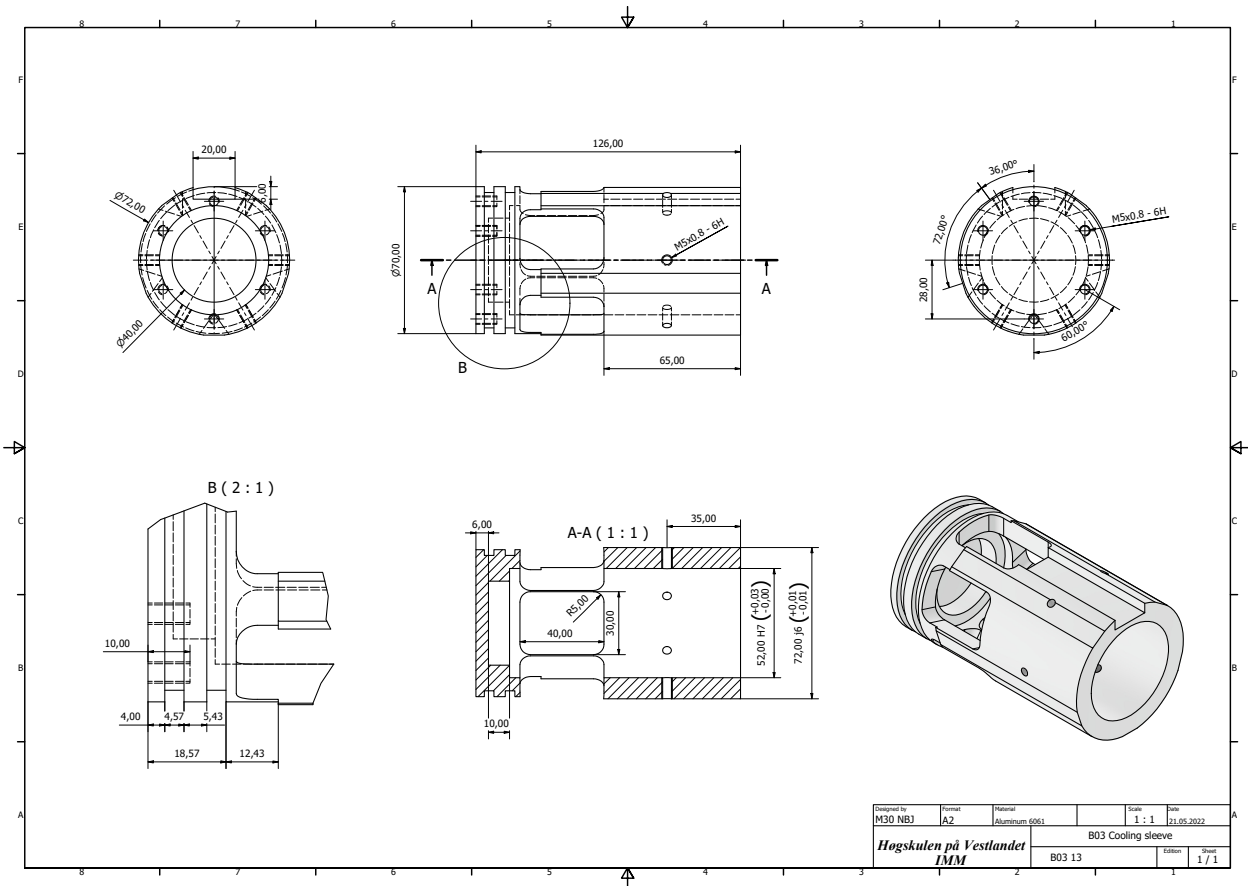


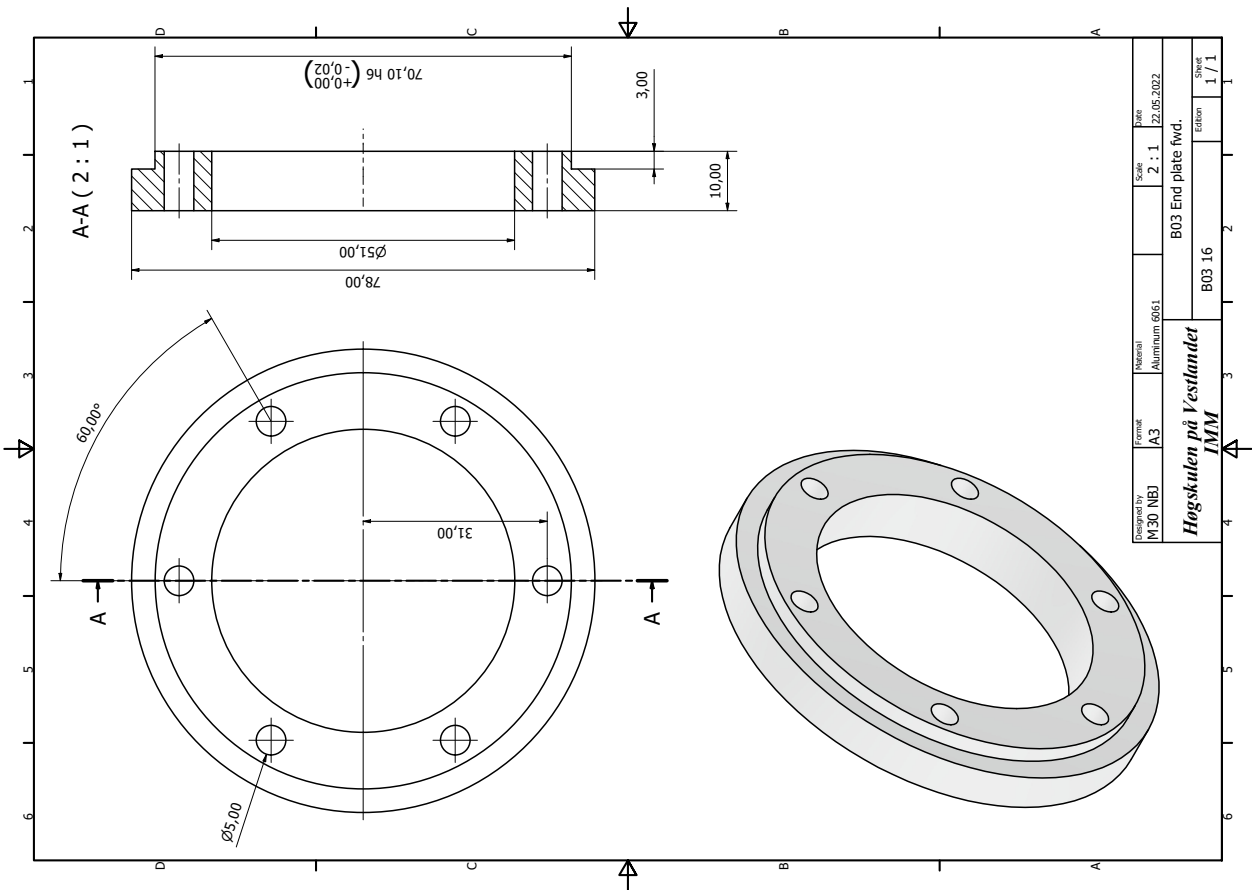
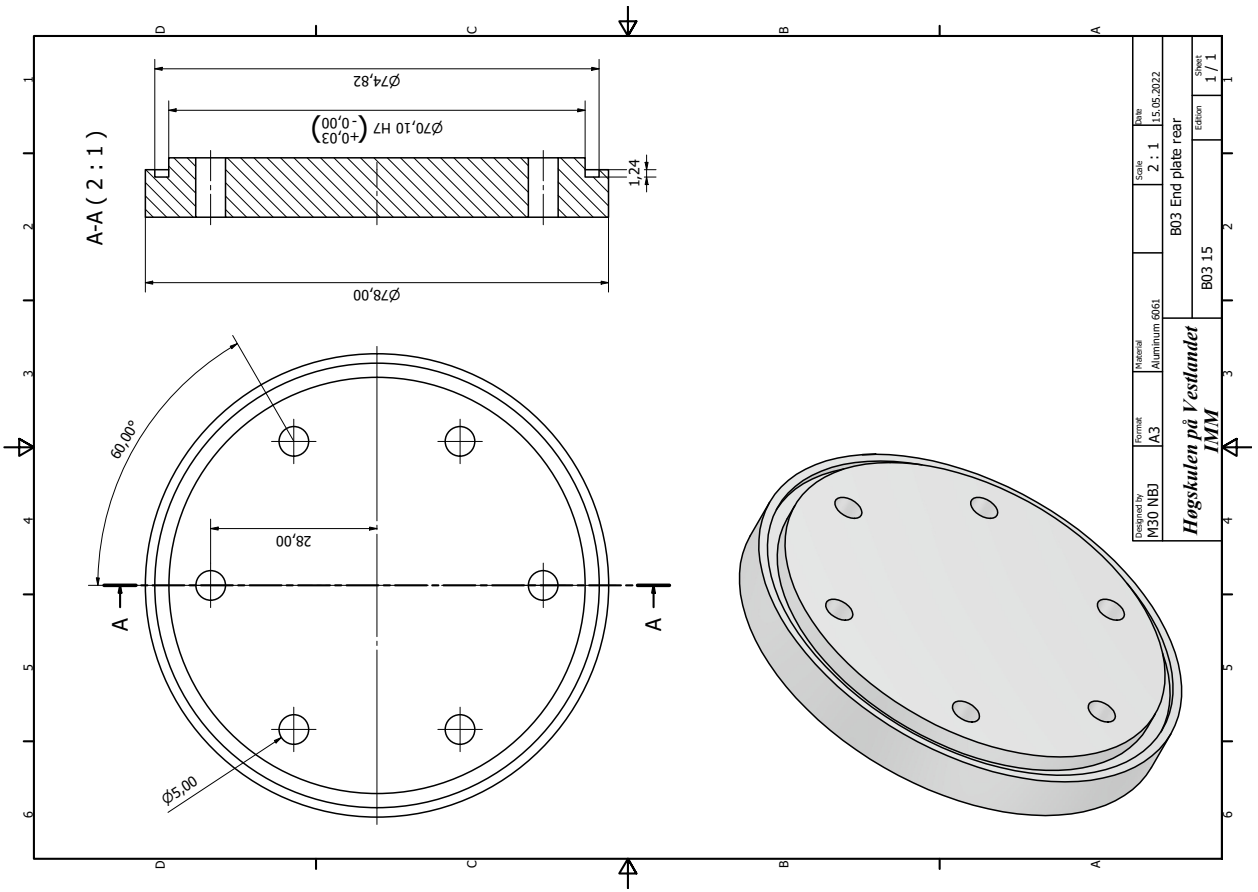


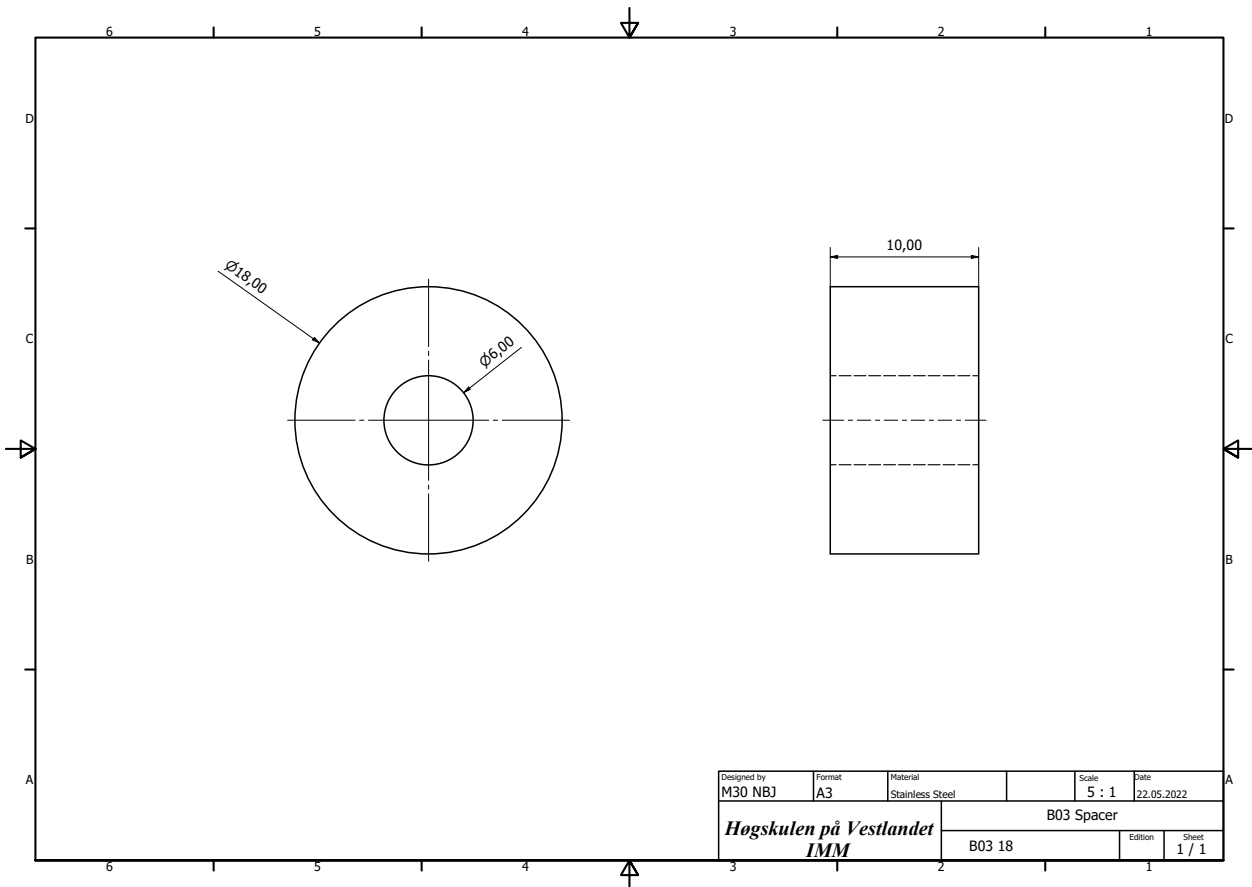
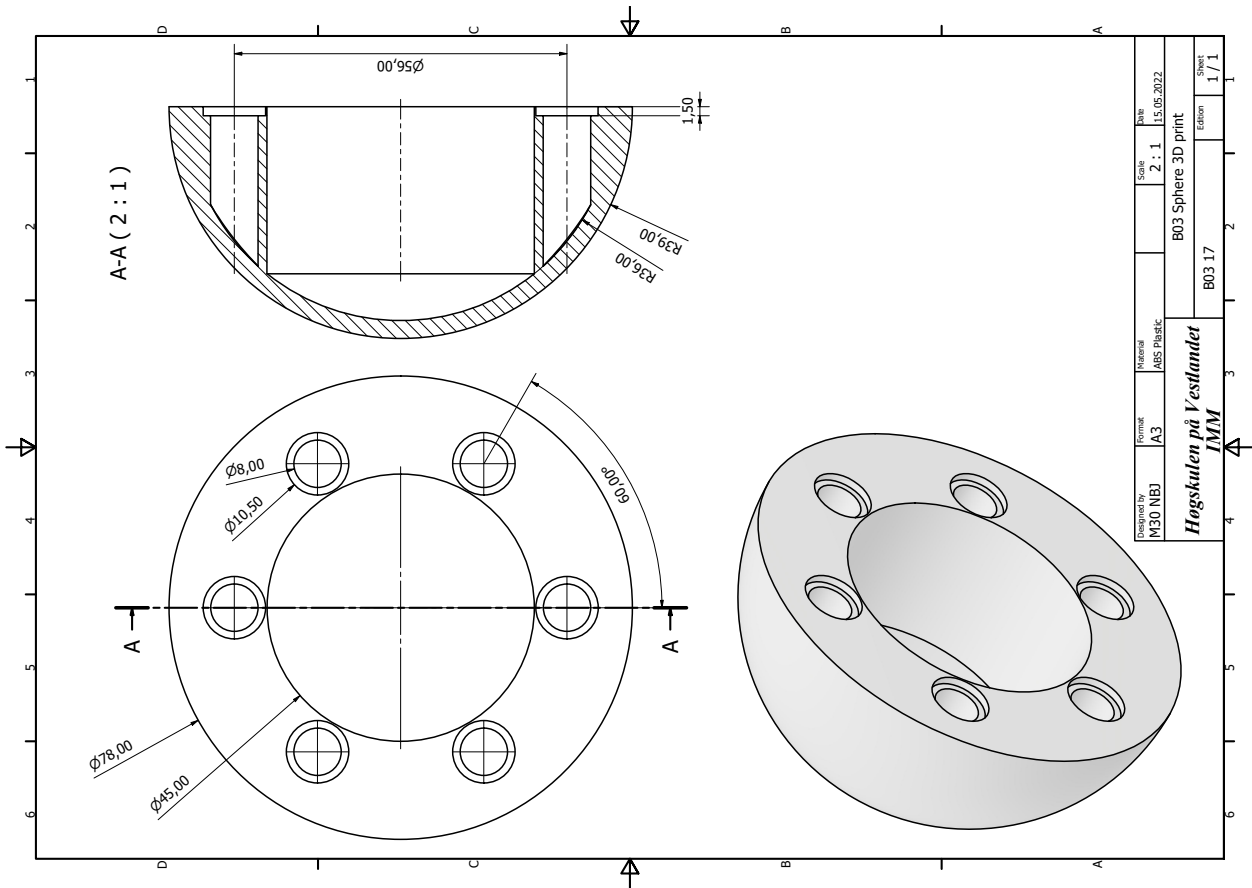


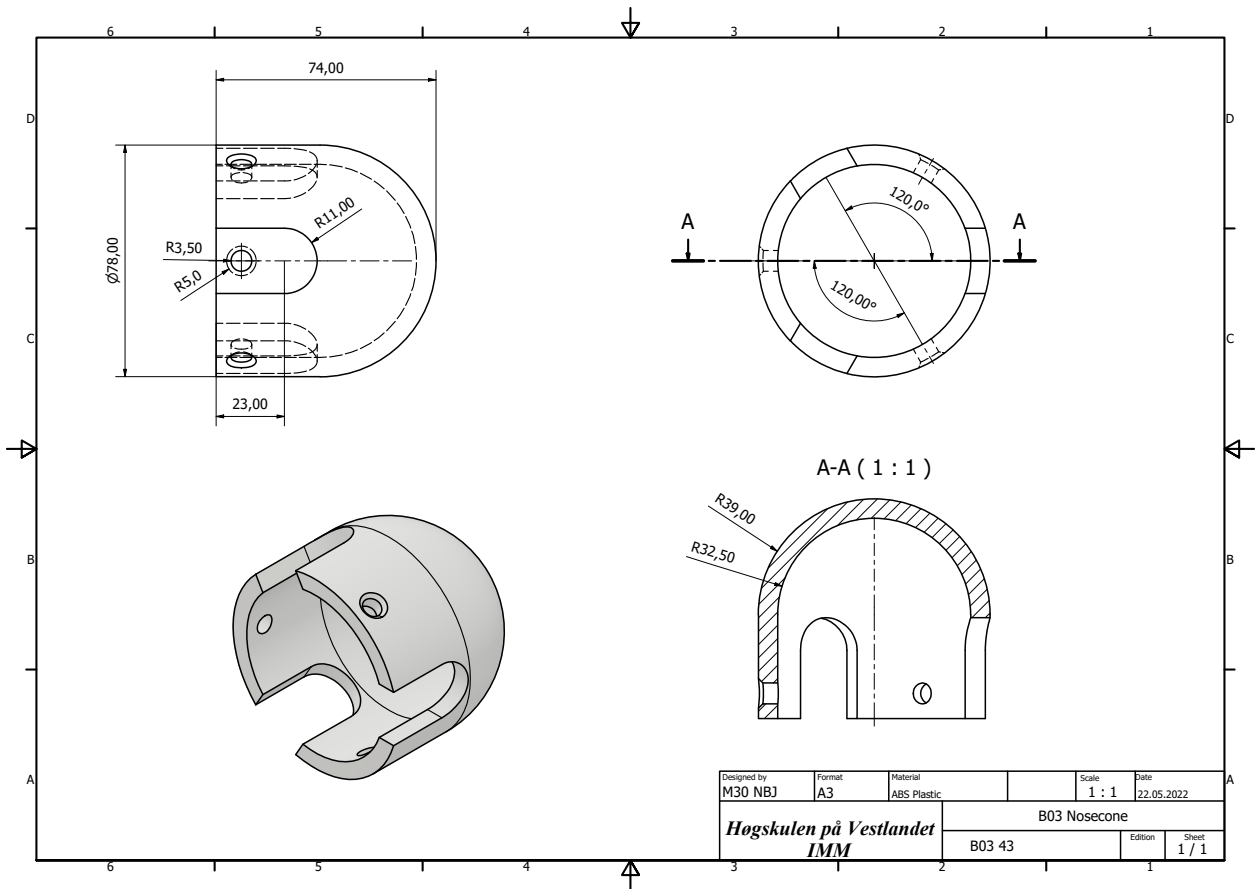
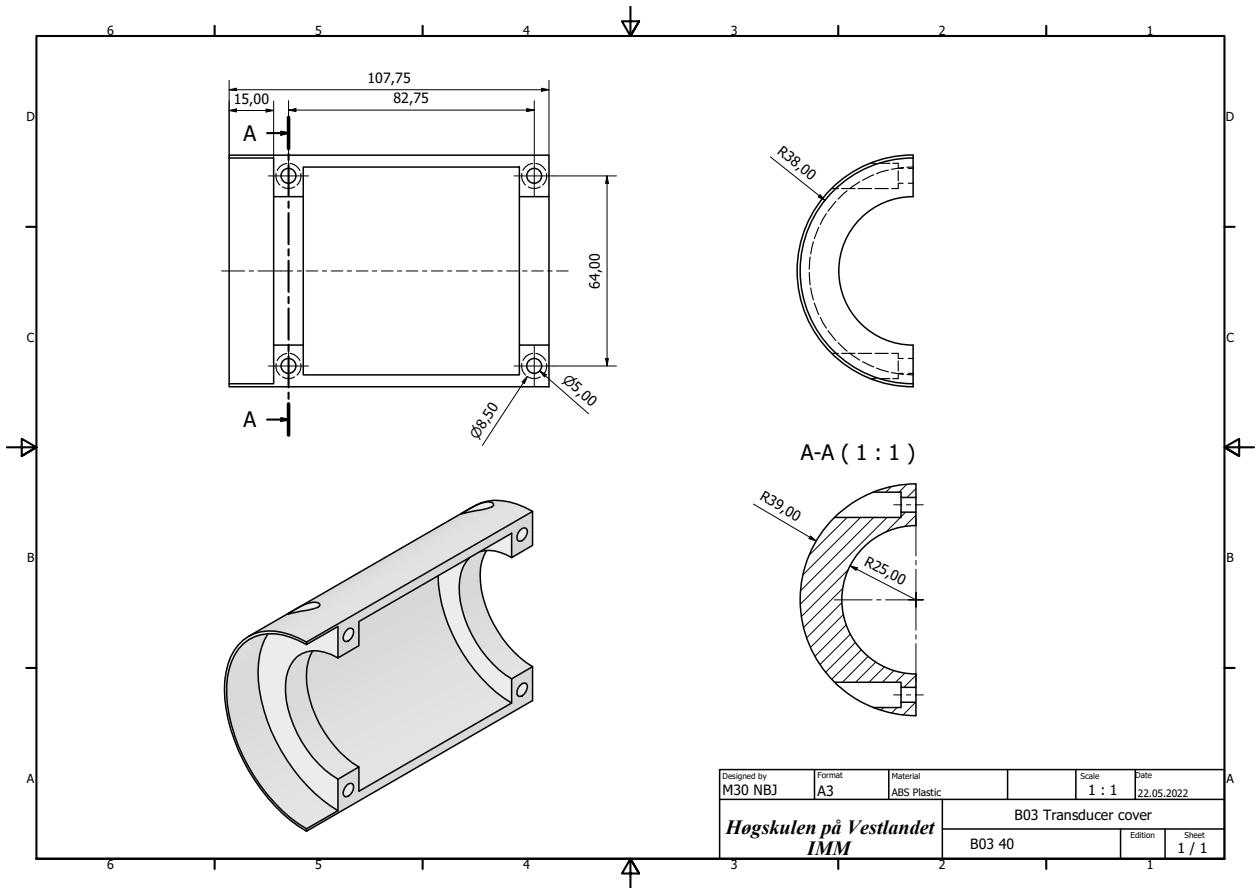












Appendix C: MatLab script

Power spectral analysis

```
clear all
format long
format compact
close all
clc

filename1 = 'U06_Twr_05m.txt';
filename2 = 'U06_Twr_Tung_05m.txt';
data1=importlabdata(filename1);
data2=importlabdata(filename2);
k=2;
data_onecolumn1 = data1(:,2);
data_onecolumn2 = data2(:,2);

%%
fs=2000; % sampling freq ADV, max
nr_cols=2; % number of columns in data file
frames_check1=length(data_onecolumn1)/(nr_cols); % insert number of cols in file
Data1 = reshape(data_onecolumn1',nr_cols,frames_check1)';
frames_check2=length(data_onecolumn2)/(nr_cols); % insert number of cols in file
Data2 = reshape(data_onecolumn2',nr_cols,frames_check2)';

samples1=Data1(:,2);
samples2=Data2(:,2);
time1=[1/fs:1/fs:length(samples1)/fs]';
time2=[1/fs:1/fs:length(samples2)/fs]';

Load1=Data1(:,2); % raw data is in Volt
Load2=Data2(:,2); % raw data is in Volt

%% cut off start and breakdown data
time_short1=time1(10201:50000);
Load_short1=Load1(10201:50000);

time_short2=time2(10201:50000);
Load_short2=Load2(10201:50000);
```

```

%% Plot time series
figure(1)
plot(time1,Load1,'b-'),hold on
plot(time_short1,Load_short1,'r-'),hold on
legend('full signal','cut signal','Location','northeast')

ylabel('$Load [N]$', 'interpreter','latex')
xlabel('$Time [s]$', 'interpreter','latex')
set(gca,'fontname','times','fontsize',15)
box on
grid on

%% Frequency analysis load cell

[pxx1,f1] = pwelch(Load_short1,[],[],[],200);
[pxx2,f2] = pwelch(Load_short2,[],[],[],200);

figure(3)

plot(f1,10.*(log10(pxx1)),f2,10.*(log10(pxx2)), 'LineWidth',1.3),hold on, grid on;

xlabel('Frequency [Hz]')
ylabel('PSD [dB]')
set(gca,'fontname','times','fontsize',15)

xlim([-1 2])
ylim([-90 0])
legend('Twr 0.5m','Twr 0.5m w','Location','northeast')

% publish('Frekvens.m','pdf');

```

Drag force data processing.

```
clc
clear all
close all

load("Drag_best_twr.mat")

%Choose column for y values (Force 0, 1,...)
col = 2;

%read in porous disc data

%filenames = 'U0p2mps_Tårn.txt';
filenames=dir('U*GT.txt');

for i=1:length(filenames);

TwrOnlydata = importlabdata(filenames(i).name);

Fs = 2000;
time = [0:1/Fs:(size(TwrOnlydata,1)-1)/Fs]';

%% get zero offset
startind_z1 = [0.1,0.1,0.1,0.1,0.1].*Fs;
endind_z1 = [1,1,1,1,1].*Fs;
Meanoffsetstart = mean(TwrOnlydata(startind_z1(i):endind_z1(i),col))
TwrOnlydata_tmp = TwrOnlydata(:,col)-Meanoffsetstart;
TwrOnlydata(:,col) = TwrOnlydata_tmp;

%% Crop data for start and end

startind = [15,15,15,15,15].*Fs;
endind = [130,60,40,30,25].*Fs;
TwrOnlydata_tmp = TwrOnlydata(startind(i):endind(i),:);

%%
figure('color','w')
plot(time,TwrOnlydata(:,col),'k-')
hold on
plot(time(startind(i):endind(i),:),TwrOnlydata_tmp(:,col),'r-')
xlabel('Time [s]')
ylabel('Force [N]')
set(gca,'fontname','times','fontsize',20)
legend('Recorded data','Cropped data',Location='northwest')

%% Find mean tare drag

GT_taredrag(i) = mean(TwrOnlydata_tmp(:,col))

rho = 1000;
A_turbine = 0.00651; %fra inventor m^2
Atwr = 0.05*0.5;
A_twr_turbine=A_turbine+Atwr
U0 = [0.2, 0.4, 0.6, 0.9,1];
L_c = 0.6; %characteristic length = length of turbine in meters
```

```

Re_turbine_Gt(i) = U0(i)*L_c/1.14e-6;
CD_GT_twr(i) = GT_taredrag(i)/(0.5*rho*A_twr_turbine*U0(i)^2)
%Re_twr(i) = U0(i)*L_c/1.14e-6

TwrOnly{i} = TwrOnlydata_tmp;
end

%% PLOT Drag coefficient of turbine

L_c = 0.6; %characteristic length = length of turbine in meters

Turbine_drag = GT_taredrag-Drag_best_twr
CD_GT = (Turbine_drag./(0.5*rho*A_turbine.*U0.^2))

figure('color','w');
plot(Re_turbine_Gt,CD_GT,'o');
ylabel('$C_D$', 'interpreter','latex')
xlabel('$R_{e_{Turbine}}$', 'interpreter','latex')
%sizefig('CDvsRe_twr-only.eps',1,'p',1/4,1/2)
set(gca,'fontname','times','fontsize',12)
box on
grid on
save('Drag_GT.mat','GT_taredrag','CD_GT','CD_GT_twr','Re_turbine_Gt','TwrOnly');

```

Drag force and coefficients plots.

```
clc
clear all
close all

%% Load previous data

load('Drag_GT.mat','GT_taredrag','CD_GT','CD_GT_twr','Re_turbine_Gt')
load('Drag_NT_SK.mat','NT_SK_taredrag','CD_NT_SK','CD_NTSK_twr','Re_turbine')
load('Drag_NT_SL.mat','NT_SL_taredrag','CD_NT_SL','CD_NTSL_twr')
load('Drag_NT_TD.mat','NT_TD_taredrag','CD_NT_TD','CD_NTTD_twr')
load('Drag_twr_05.mat','H05_twr_taredrag','CD_05','Re_twr')
load('Drag_twr_05_vekt.mat','H05_twr_vekt_taredrag','CD_05_w')
load('Drag_best_twr.mat','Drag_best_twr')
%% (Twr+trubin)-twr

GT_only = GT_taredrag-Drag_best_twr;
NT_SK_only = NT_SK_taredrag-Drag_best_twr;
NT_SL_only = NT_SL_taredrag-Drag_best_twr;
NT_TD_only = NT_TD_taredrag-Drag_best_twr;

%% Theoretical drag from tower
Ct = 1.2
rho = 1000
A_twr = 0.05*0.5
V=[0.2, 0.4, 0.6, 0.9, 1]

Fd_twr = 0.5*Ct*rho*A_twr.*V.^2

Cd_twr_theory = [1.2 1.2 1.2 1.2 1.2]

%% Drag force plots

% twr
figure('color','w');

hold on;
plot(V,H05_twr_taredrag,'-x',LineWidth=0.7);
hold on;
plot(V,H05_twr_vekt_taredrag,'-s',LineWidth=0.7);
hold on;
plot(V,Fd_twr,'-.v',LineWidth=0.7);
legend('Twr 0.5m','Twr 0.5m w','Theoretical value','location','northwest')
hold off;

ylabel('Drag [N]','interpreter','latex')
xlabel('$V$ [m/s]','interpreter','latex')
%sizefig('CDvsRe_twr-only.eps',1,'p',1/4,1/2)
set(gca,'fontname','times','fontsize',15)
box on
grid on

% twr + turbine
figure('color','w');
plot(V,GT_taredrag,'-o',LineWidth=0.8);
```

```

hold on;
plot(V,NT_TD_taredrag, '-d',LineWidth=0.8);
hold on;
plot(V,NT_SL_taredrag, '-v',LineWidth=0.8);
hold on;
plot(V,NT_SK_taredrag, '-*',LineWidth=0.8);
legend('PT twr','NT TD twr','NT SL twr','NT SC twr','location','northwest')

```

```

ylabel('Drag [N]','interpreter','latex')
xlabel('$V$ [m/s]','interpreter','latex')
%sizefig('CDvsRe_twr-only.eps',1,'p',1/4,1/2)
set(gca,'fontname','times','fontsize',20)
box on
grid on

```

```

% turbine experimental

```

```

figure('color','w');
plot(V,GT_only, '-o',LineWidth=0.7);
hold on;
plot(V,NT_TD_only, '-d',LineWidth=0.7);
hold on;
plot(V,NT_SL_only, '-v',LineWidth=0.7);
hold on;
plot(V,NT_SK_only, '-*',LineWidth=0.7);
legend('PT','NT TD','NT SL','NT SC','location','northwest')

```

```

ylabel('Drag [N]','interpreter','latex')
xlabel('$V$ [m/s]','interpreter','latex')
%sizefig('CDvsRe_twr-only.eps',1,'p',1/4,1/2)
set(gca,'fontname','times','fontsize',15)
box on
grid on

```

```

% Turbine theoretical (subtracting theoretical value)

```

```

figure('color','w');
plot(V,GT_taredrag-Fd_twr, '-o',LineWidth=0.9);
hold on;
plot(V,NT_TD_taredrag-Fd_twr, '-d',LineWidth=0.9);
hold on;
plot(V,NT_SL_taredrag-Fd_twr, '-v',LineWidth=0.9);
hold on;
plot(V,NT_SK_taredrag-Fd_twr, '-*',LineWidth=0.9);
legend('PT','NT TD','NT SL','NT SC','location','northwest')

```

```

ylabel('Drag [N]','interpreter','latex')
xlabel('$V$ [m/s]','interpreter','latex')
%sizefig('CDvsRe_twr-only.eps',1,'p',1/4,1/2)
set(gca,'fontname','times','fontsize',21)
box on
grid on

```

```

%% Drag coefficient plots

```

```

%% Twr_only

```

```

figure('color','w');

```

```

hold on;
plot(Re_twr,CD_05,'-x',LineWidth=0.7);
hold on;
plot(Re_twr,CD_05_w,'-s',LineWidth=0.7);
hold on;
plot(Re_twr,Cd_twr_theory,'-.v',LineWidth=0.7);
hold on;
% plot(U0,Fd_twr,'-.v',LineWidth=0.7);
legend('Twr 0.5m','Twr 0.5m w','Theoretical value','location','northwest')
hold off;
ylim([1 2.2]);

ylabel('$C_D$', 'interpreter', 'latex')
xlabel('$R_e$', 'interpreter', 'latex')
%sizefig('CDvsRe_twr-only.eps',1,'p',1/4,1/2)
set(gca,'fontname','times','fontsize',15)
box on
grid on

%% Nacelle-twr

figure('color','w');
plot(Re_turbine_Gt,CD_GT,'-o',LineWidth=0.7);
hold on;
plot(Re_turbine,CD_NT_TD,'-d',LineWidth=0.7);
hold on;
plot(Re_turbine,CD_NT_SL,'-v',LineWidth=0.7);
hold on;
plot(Re_turbine,CD_NT_SK,'-*',LineWidth=0.7);
legend('PT','NT TD','NT SL','NT SC','location','northwest')

ylabel('$C_D$', 'interpreter', 'latex')
xlabel('$R_e$', 'interpreter', 'latex')
%sizefig('CDvsRe_twr-only.eps',1,'p',1/4,1/2)
set(gca,'fontname','times','fontsize',15)
box on
grid on

%% Nacelle-twr (Theoretical)
figure('color','w');
plot(Re_turbine_Gt,CD_GT_twr,'-o',LineWidth=0.7);
hold on;
plot(Re_turbine,CD_NTTD_twr,'-d',LineWidth=0.7);
hold on;
plot(Re_turbine,CD_NTSL_twr,'-v',LineWidth=0.7);
hold on;
plot(Re_turbine,CD_NTSK_twr,'-*',LineWidth=0.7);
legend('PT twr','NT TD twr','NT SL twr','NT SC twr','location','north')

ylabel('$C_D$', 'interpreter', 'latex')
xlabel('$R_e$', 'interpreter', 'latex')
%sizefig('CDvsRe_twr-only.eps',1,'p',1/4,1/2)
set(gca,'fontname','times','fontsize',15)
box on
grid on

```

```
%% Nacelle&twr

figure('color','w');
plot(Re_turbine_Gt,CD_GT_twr,'-o',LineWidth=0.7);
hold on;
plot(Re_turbine,CD_NTTD_twr,'-d',LineWidth=0.7);
hold on;
plot(Re_turbine,CD_NTSL_twr,'-v',LineWidth=0.7);
hold on;
plot(Re_turbine,CD_NTSK_twr,'-*',LineWidth=0.7);
legend('PT twr','NT TD twr','NT SL twr','NT SC twr','location','north')

ylabel('$C_D$', 'interpreter', 'latex')
xlabel('$R_e$', 'interpreter', 'latex')
%sizefig('CDvsRe_twr-only.eps',1,'p',1/4,1/2)
set(gca,'fontname','times','fontsize',15)
box on
grid on
```


Extraction of best combined tower data.

```
clc
clear all
close all

load("Drag_twr_05.mat","H05_twr_taredrag")
load("Drag_twr_05_vekt.mat","H05_twr_vekt_taredrag")

%% Experimental
A = H05_twr_vekt_taredrag(1:2)
B = H05_twr_taredrag(3)
C = H05_twr_vekt_taredrag(4:5)

Drag_best_twr = [A, B, C]

%% Theoretical
Ct = 1.2
rho = 1000
A_twr = 0.05*0.5
V=[0.2, 0.4, 0.6, 0.9, 1]

Fd_twr = 0.5*Ct*rho*A_twr.*V.^2

Cd_twr_theory = [1.2 1.2 1.2 1.2 1.2]

%Drag_best_twr = Fd_twr

save('Drag_best_twr.mat','Drag_best_twr')
```

Resonance analysis.

```
clc
clear all
close all

%% VIV

St = 0.22;
U = [0.2 0.4 0.6 0.9 1];
D = 0.05; %m outer diameter twr
d = 0.043; %m inner diameter twr

f = St.*U/D;

%% Plot shedding frequency

figure('color','w');
hold on;
plot(U,f,'-x',LineWidth=0.7);
legend('Shedding frequency','location','northwest')

ylabel('Hz','interpreter','latex')
xlabel('Flow velocity [m/s]','interpreter','latex')
set(gca,'fontname','times','fontsize',15)
box on
grid on

%% Natural frequency tower

E = 69*10^9; %modulus elasticity
I = (pi*D^4/64)-(pi*d^4/64); %are moment cylinder
L = 0.65; % free length

m_twr = 2.65;
m_twr_stiffer = 0;
m_twr_holder = 2.45;
m_turbine = 2.3;
m_max = 10
m_added_twr = 1.6
% m_twr_holder+m_twr_stiffer+m_twr

m = [2, m_twr, m_twr+m_twr_stiffer, m_twr+m_twr_stiffer+m_turbine,
m_twr+m_twr_stiffer+m_turbine+m_added_twr, m_max]

%% Plot natural frequency vs shedding frequency theoretical (rigid body)

k = (3*E*I)/L^3;

fn = (1/(2*pi))*(sqrt(k./(m)))

figure('color','w');
hold on;
%subplot(2,1,1)
yyaxis left
plot(f,U,'-*',LineWidth=0.7) % Plot into left axes
ylabel('$V$ [m/s]','interpreter','latex')
```

```

yyaxis right
plot(fn,m,'-o',LineWidth=0.7)
ylabel('m [kg]','interpreter','latex')

legend('Shedding frequency','Natural frequency cylinder')
%title('Shedding vs natural frequency | Theoretical values')
xlabel('f [Hz]','interpreter','latex')
set(gca,'fontname','times','fontsize',15)
box on
grid on
%hold on

%% Plot natural frequency vs shedding frequency experimentally observed

k2 = 1500 % estimated k value from observations

fn = (1/(2*pi))*(sqrt(k2./(m)))

%
figure('color','w');
% hold on;
%subplot(2,1,2)
yyaxis left
plot(f,U,'-*',LineWidth=0.7) % Plot into left axes
ylabel('$V$ [m/s]','interpreter','latex')
yyaxis right
plot(fn,m,'-o',LineWidth=0.7)
ylabel('m [kg]','interpreter','latex')

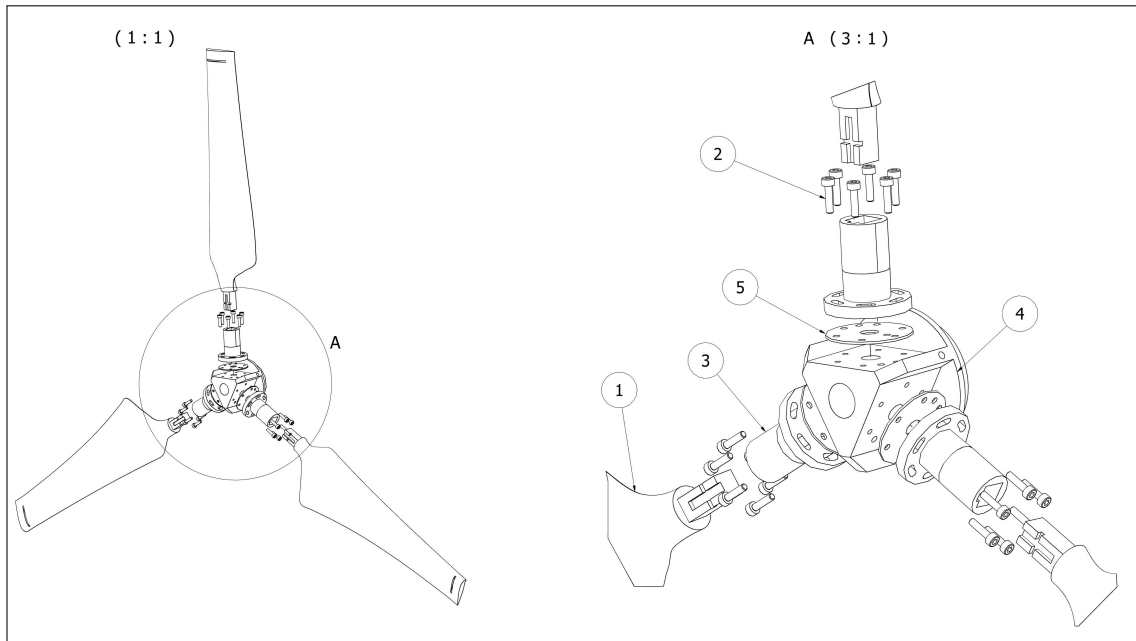
legend('Shedding frequency','Natural frequency cylinder')
%title('Shedding vs natural frequency | Observed values')
xlabel('f [Hz]','interpreter','latex')
set(gca,'fontname','times','fontsize',15)
box on
grid on

```

Appendix D: Assembly manual

Sub-assemblies are used to break down the structure into smaller compositions, installed as separate units in the complete turbine assembly. Components that requires special tools or procedures during assembly, such as bearings and seals, will preferably be included in its own sub-assembly. This allows the bearing housings to be easily separated from the main assembly, and service can be performed effectively without the risk of damaging larger components. In addition, the design allows relative ease of complete assembly, by only involving light tools to work with on a regular basis. The design consists of three sub-assemblies. The turbine rotor assembly, the forward bearing/seal housing and the rear bearing housing.

The turbine rotor is the component that allows energy to be converted from the passing fluid to usable, electrical power. A major feature of the turbine relies on its ability to accommodate different turbine blades to assess its characteristics. In regards to this, a flexible solution is developed that allows adjustments of the turbine blades to be made with ease.

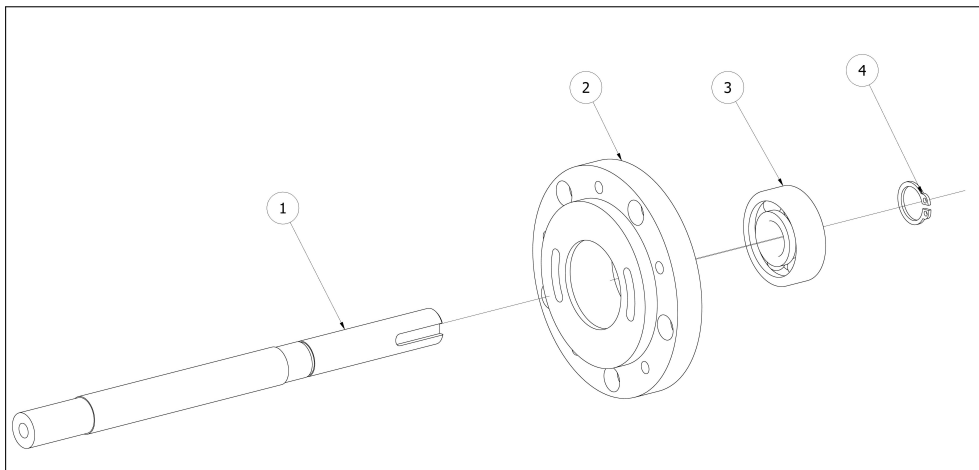


- | | | |
|----------------------|-----------------------------------|------------------------|
| 1. Turbine blade | 2. M3 x 12 hex. socket head screw | 3. Blade root adjuster |
| 4. Turbine blade hub | 5. Blade root adjustment plate | |

Figure .4: Turbine rotor exploded view

1. Place the turbine blade hub (4) in a vice with one of the three flange faces pointing upwards. Small force should be applied to avoid damaging the contact surfaces.
2. The angle of the turbine blades (1) should be determined before the blade root adjuster (3) is installed. The kidney slots allow 20° fully adjustable areas with a gap of 40° between each slot.
3. Take one of the three adjustment plates (5) and place it on the flange face while aligning the holes in the plate and hub.
4. The same procedure is performed on the blade root adjuster. In addition a locking pin align the plate and adjuster to each other.
5. Six M3 x 12 hex. socket head screws (2) are then used to attach the plate and adjuster to the hub. Washers or a small amount of sealant can be applied for thread locking. Torque is kept to a minimum to avoid damaging the threads.
6. The turbine blades are then placed inside the squared slots of the blade root adjuster and locked in place with the locking mechanism...
7. The procedure are repeated for each of the three turbine blades.

The second bearing housing has multiple functions. While it houses the second bearing it also works as a mounting flange for the forward cage as well as a wire passage. The assembly is relatively simple, but it is still preferable to do this separately in advance of the final turbine assembly.

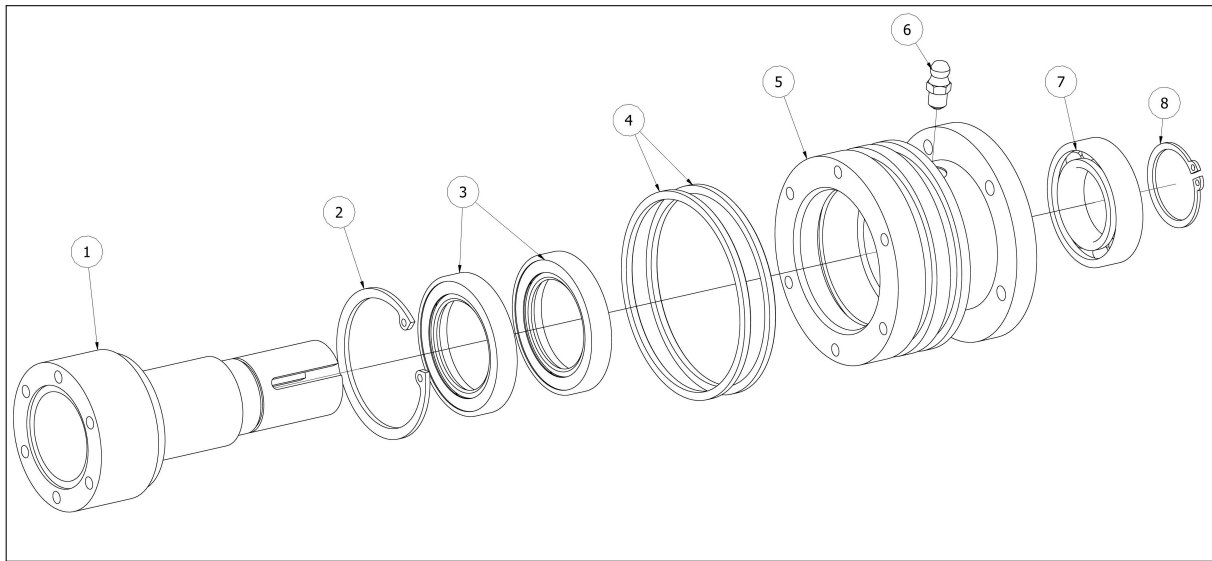


1. Driveshaft 2
 2. Bearing housing rear
 3. Ball bearing SKF 16201-2RS1
 4. Spring retaining ring 12 x 1

Figure .5: Bearing housing rear exploded view

1. The assembly can be done by involving cooling and heating of components or by press force. Either way are approved methods, but the first one will be preferred if possible.
2. Heat the housing (2) to approximately 100°C and cool down the bearing(3) to -20°C. This gives the bearing a temporarily loose fit during insertion. After inserting the bearing, allow the parts to reach room temperature before proceeding.
3. Cool down the driveshaft (1) as much as possible without without permanently interfering on a molecular level. Heat the housing with the bearing inserted to a moderate temperature of around 50°C. The driveshaft can then be inserted. Make sure the guiding edge is fully inserted and in contact with the inner ring of the bearing.
4. If press force must be used for the previous step, make sure that a counter force is applied on the opposite side of the bearing side to prevent it moving out of position.
5. Finally, install the retaining ring (4) on the driveshaft to keep the driveshaft in place.

The bearing/seal housing in the front has one of the most important functions in the turbine. This part separates the water-exposed side from the dry and isolated inside of the turbine with a series of seals. In addition, the bearing is one of two bearings that hold the driveshafts and its forces. For that reason, a reliable solution with high redundancy is developed to protect the electrical components from water intrusion.



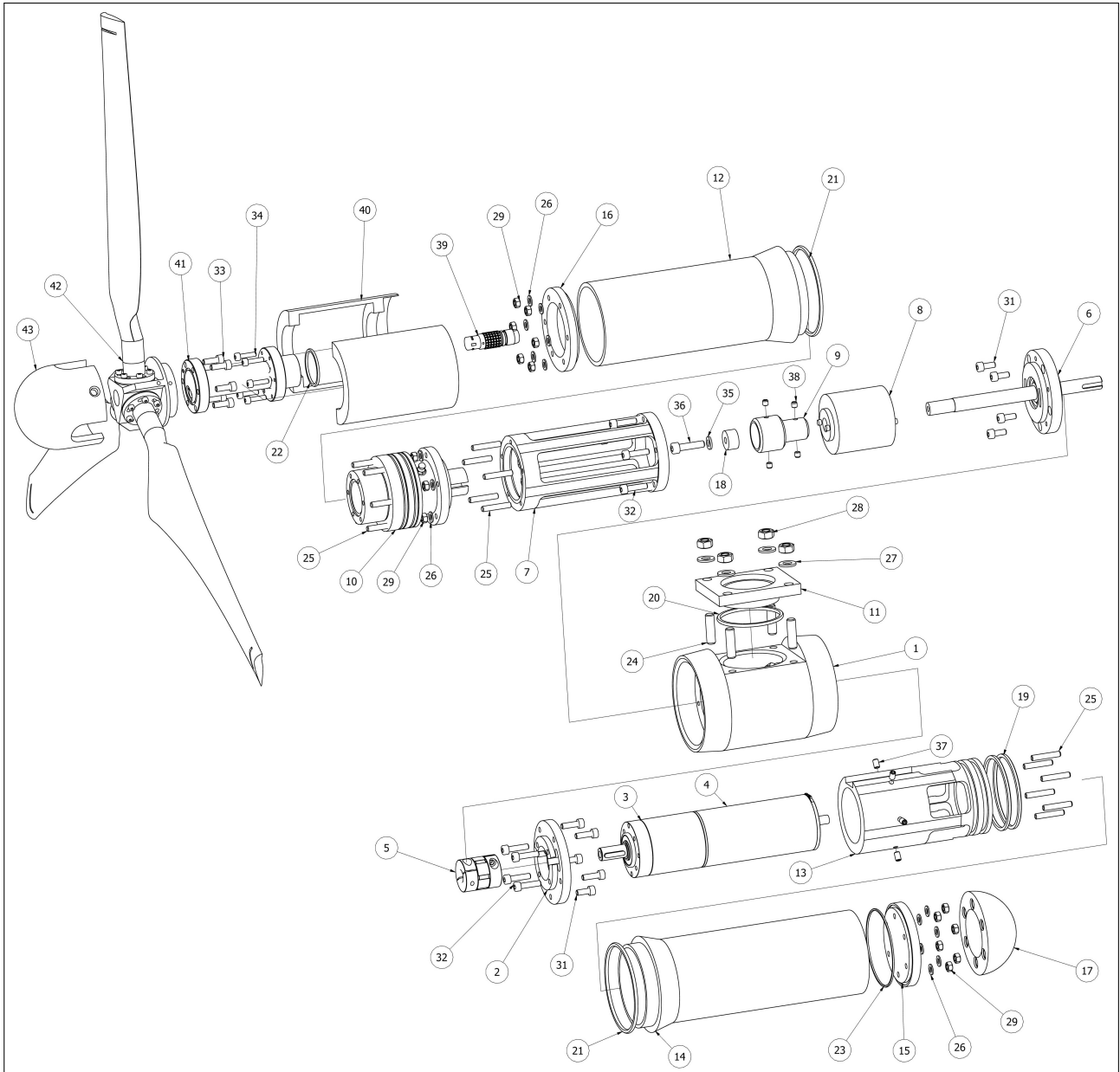
- | | | |
|--------------------------------|------------------------------------|--------------------------------------|
| 1. Driveshaft 1 | 2. Spring retaining ring 48 x 1,75 | 3. Rotary shaft lip seal 30 x 47 x 7 |
| 4. O-ring 66,34 x 2,62 | 5. Bearing/seal housing | 6. Grease nipple M6 |
| 7. Ball bearing SKF 61905-2RS1 | 8. Spring retaining ring 25 x 1,2 | |

Figure .6: Bearing/seal housing fwd. exploded view

1. The assembly can be done by involving cooling and heating of components or by press force. Either way are approved methods, but the first one will be preferred if possible.
2. Start by removing one of the two rubber lip seals of the bearing (7) to allow lubrication from inside of the housing (5). This side should naturally point towards the grease nipple (6) when installed.
3. The next step is to heat the housing to approximately 100°C and cool down the bearing to -20°C. This gives the bearing a temporarily loose fit during insertion. After inserting the bearing, allow the parts to reach room temperature before proceeding.
4. Insert the two axial lip seals (3) by applying press force on the outside rings. The inner most seal should be mounted with the exposed spring side facing inwards, and the outer seal should face the opposite way.
5. The largest retaining ring (2) are then installed in the housing on the sealing side to prevent them from moving.
6. Cool down the driveshaft (1) as much as possible without without permanently interfering on a molecular level. Heat the housing with the other components inserted to a moderate temperature of around 50°C. The driveshaft can then be inserted. Make sure the guiding edge is fully inserted and in contact with the inner ring of the bearing.
7. If press force must be used for the previous step, make sure that a counter force is applied on the opposite side of the bearing to prevent it moving out of position.
8. Install the other retaining ring (8) to secure the driveshaft from moving.
9. Lubricated the two o-rings (4) with suitable silicone grease and stretch them over the housing into their grooves.
10. Lastly, the grease nipple should be installed and grease should be inserted. This will lubricate both seal and bearing while acting as a water barrier.

The main assembly is relatively involving and requires a variety of tools and components. Figure .7 presents all components in an exploded view and trails are used as guides in an orderly manner to get a compact yet clear drawing view. The following instruction should be used as guidelines, but can vary if the user finds other improved methods.

1. Note that all seals and o-ring should be lubricated with a suitable silicone grease before installation. In addition the wires from the components are not showed in Figure .7, but routing can be examined in Figure 3.11.
2. Start by placing the boss (1) in a vice and use it as a base for the complete assembly.



- | | | |
|-------------------------------|------------------------------|------------------------------|
| 1. Boss | 2. Motor holder flange | 3. Gearbox |
| 4. Motor | 5. Jaw coupling | 6. Bearing housing asm. |
| 7. Cage | 8. Slipring | 9. Shaft coupling |
| 10. Bearing/seal housing asm. | 11. Tower flange | 12. Turbine housing fwd. |
| 13. Cooling sleeve | 14. Turbine housing rear | 15. End plate rear |
| 16. End plate fwd. | 17. Sphere 3D print | 18. Spacer |
| 19. O-ring 66,34 x 2,62 | 20. O-ring 55,25 x 2,62 | 21. O-ring 78,97 x 3,53 |
| 22. O-ring 30 x 1,8 | 23. O-ring 69,57 x 2,41 | 24. Stud M8 x 20 |
| 25. Stud M5 x 20 | 26. Plain washer M5 | 27. Plain washer M8 |
| 28. Hex. nut M8 | 29. Hex. nut M5 | 30. Hex. socket head M5 x 16 |
| 31. Hex. socket head M5 x 12 | 32. Hex. socket head M5 x 20 | 33. Hex. socket head M5 x 14 |
| 34. Hex. socket head M4 x 16 | 35. Plain washer M6 | 36. Hex. socket head M6 x 25 |
| 37. Hex. set screw M5 x 8 | 38. Hex. set screw M5 x 5 | 39. Transducer connector |
| 40. Transducer cover | 41. Transducer | 42. Turbine rotor asm. |
| 43. Nosecone | | |

Figure .7: Model turbine exploded view

3. Fasten six M5 x 20 studs (25) at the end of the cooling sleeve (13) with the use of Loctite sealant 222 or 243.
4. Apply some Loctite 620 inside the cooling sleeve. Slide the cooling sleeve on to the motor. Use light force to overcome the tight fit and insert six hex. set screws (37) in each hole. The wire routing slot should point upwards and the sleeves lengthwise position will be limited by a guiding edge.
5. Route the wires from the motor (4) into the wire slot on the sleeve and through the motor holder flange (2). Mount the flange to to the gearbox (3) using four M5 x 20 hex. socket head screws (32).
6. Place a key in the key slot for the gearbox output shaft and mount the jaw coupling (5) on the shaft.
7. Use five M5 x 12 hex. socket head screws (31) to mount the motor holder and its components to the boss. Make sure that the two wire routing passages are oriented upwards. Take the wires out from the boss through the tower flange hole.
8. Stretch the two o-rings (19) over the sleeve and into their grooves. Fit the o-ring (21) over the rear turbine housing (14) and slide the housing over the motor and gearbox into its position.
9. Place the o-ring (23) in the grove of the rear end plate (15) and use six M5 washers (26) and hex. nuts (29) to tighten up the end plate to the housing. Attach the sphere (17). The back side of the turbine is now complete.

10. Proceed to the front section. Attach the bearing housing assembly (6) to the boss and jaw coupling using five M5 x 12 hex. socket head screws (31). Fasten the jaw coupling to the driveshaft 2 through the tower flange hole.
11. Slide the slipring (8) onto driveshaft 2 and attach the locking ring to the shaft with the suited screws. Note that the rotating part should face forward and the stationary wires can be routed through the bearing housing. Lock the outside of the slipring to the cage with the sliprings locking pin (not showed).
12. Mount the shaft coupling (9) to driveshaft 2 with the spacer (18), M6 washer (35) and a M6 x 25 hex. socket head screw.
13. Mount the cage (7) to the bearing housing using five M5 x 20 hex socket head screws and insert five M5 x 20 studs at the front of the cage by using Loctite 222 or 243 as thread locking.
14. As the transducer connector (39) is attached to the slipring directly by wire, it is necessary to route this in the correct order. Align the bearing/seal housing (10) and lead the transducer connector through the hollow driveshaft 1 .
15. The wires from the connector should exit on two sides of driveshaft 1 in the milled slots. Follow up by pushing the housing into position while driveshaft 1 enters the shaft connector. Fasten the housing with five M5 washers and M5 hex. nuts to the cage.
16. Step 9. can now be replicated at the front of the turbine involving the forward trubine housing (12), the forward end plate (16) and the same nuts, bolts and seal.
17. The transducer connector can now be connected to the transducer (41) and the o-ring (22) can be stretched onto the transducer rear flange.
18. Insert the transducer in the driveshaft 1 and use six M4 x 16 hex. socket head screws (34) to attach the transducer. Attach the turbine rotor assembly (42) to the transducer with six M5 x 14 hex. socket head screws (33).
19. Finish the front section by attaching the nosecone (43) and the transducer cover (40) with appropriate screws (not showed).

20. Note that the tower itself is not included in .7 due to space limitation, but it should be welded to the tower flange (11) in advance.
21. Insert four M8 x 20 studs into the boss with loctite 222 or 243 for thread locking and pull all cables through the tower to exit at the top.
22. Attach the o-ring (20) to the flange and fasten the tower flange using four M8 washers (27) and M8 hex. nuts (28). The assembly is now complete.

